Quantifying Tissue Characteristics Using Photoacoustic Methods

by

Linyu Ni

A dissertation submitted in partial fulfillment
of the requirement for the degree of
Doctor of Philosophy
(Biomedical Engineering)
in the University of Michigan
2023

Doctoral Committee:

Professor Xueding Wang, Co-Chair
Professor Guan Xu, Co-Chair
Professor Alan Argento
Professor Brian Fowlkes

Linyu Ni

nilinyu@umich.edu

ORCID iD: 0000-0003-3345-7341

© Linyu Ni 2023

Dedication

To my family, advisors, and friends, I dedicate this dissertation with sincere gratitude for your unwavering support and invaluable contributions to my academic journey.

Acknowledgements

I would like to express my deepest gratitude to my advisors, Dr. Xueding Wang and Dr. Guan Xu, for their unwavering support, expert guidance, and mentorship throughout my doctoral studies. Their passion for research, patience, and willingness to share their knowledge have been invaluable to me, and I am grateful for the opportunity to learn from them. Dr. Wang and Dr. Xu have generously given their time to work with me on every paper, conference, and project I have undertaken, providing insightful feedback, and helping me develop my research skills. Their encouragement and support have given me the confidence to pursue challenging research questions and to present my work to the scientific community.

I would like to express my sincere gratitude to the members of my committee, Dr. Alan Argento, Dr. Brian Fowlkes, and Dr. Cheri Deng, for their invaluable feedback and insightful comments throughout the course of this project. Their contributions have significantly improved the quality of my work. In particular, I am especially grateful for Dr. Argento's ongoing guidance and direction in one of my projects, as well as for his willingness to attend my defense and provide constructive feedback. I am honored to have had the opportunity to work with such distinguished scholars.

I am grateful to my family for their unwavering love and support throughout my academic journey. Despite not being able to see me often due to the distance, they have provided me with constant psychological support and motivation, which has been crucial in keeping me going during challenging times. Their encouragement and understanding have been an inspiration to me, and I cannot thank them enough for their selflessness and unwavering support throughout the four years of my graduate studies.

I am grateful to all my friends for their friendship and support during my studies. Their encouragement and understanding have helped me navigate the challenges of graduate school.

Table of Contents

Dedication ii

Acknowledgements iii

List of Figures ix

List of Tables xx

List of Abbreviations xxi

Abstract xxiii

Chapter 1 Introduction 1

1.1 Background 1

1.3 Research Objectives and Thesis Outlines 4

Chapter 2 Review of Quantification in Photoacoustic Methods 6

2.1 Theory of Photoacoustic Imaging 6

2.1.1 Photoacoustic Modalities 6

2.1.2 Photoacoustic Imaging Contrast 8

2.1.2.1 Photoacoustic Signal Generation 8

2.1.2.2 Photoacoustic Speckles 10

2.2 Quantifications in Photoacoustic Signals 11

2.2.1 Morphological Analysis 11

2.2.2 Multi-spectral Analysis 13
2.2.3 Elastography Analysis 14
2.2.4 Multivariate Parameter Classification 15
Chapter 3 Characterizing the Aggressiveness of Prostate Cancer Using an All-optical Needle Photoacoustic Sensing Probe: Feasibility Study 17
3.1 Introduction 17
3.2 Experiment Setup 20
3.2.1 System Setup 21
3.2.2 Spatial Sensitivity Distribution of the All-Optical Needle PA Sensing Probe 21
3.2.3 Phantom Preparation 22
3.2.4 Preparation of *Ex Vivo* Human Prostate Tissues 23
3.3 Analysis Methods 23
3.3.1 Nonlinear Spectrum Analysis 24
3.3.2 Envelope Statistics 25
3.3.3 Statistics and Multivariate Parameter Analysis 25
3.4 Results 27
3.4.1 Spatial Distribution of Measurement Sensitivity 27
3.4.2 Phantom Study Results 27
3.4.3 Human Tissue Results 30
3.5 Discussion and Conclusion 35
Chapter 4 Assessment of Prostate Cancer Using a Translational Needle Photoacoustic Sensing Probe: Preliminary Study on Intact Human Prostates 38
4.1 Introduction 38
4.2 Experiment Setup 40

4.2.1 Probe Design 40
4.2.2 The Controlling System 41
4.2.3 Simulated TRUS Guided Transperineal Needle PA Sensing Probe Insertion Procedure 42
4.3 Analysis Method 44
4.3.1 Histopathology 44
4.3.2 Quantification Methods 46
4.3.2.1 PASA 46
4.3.2.2 Statistics and Multivariate Analysis 47
4.4 Results 48
4.4.1 PASA at Individual Wavelength 48
4.4.2 Multivariate Parameter Analysis Using SVM 50
4.5 Discussion 51
4.6 Conclusion 52
Chapter 5 Assessing Biomechanics of Aqueous Veins and Perilimbal Sclera Using Dual-Wavelength Photoacoustic Macroscopy System 54
5.1 Introduction 54
5.2 Combined Sclera and Vessel Imaging Using Dual-Wavelength Photoacoustic Microscopy System 59
5.2.1 Imaging System Setup 59
5.2.2 Imaging of Phantoms 60
5.2.2.1 Phantom Preparation 60
5.2.2.2 Results 61
5.2.3 Imaging of *Ex Vivo* Porcine Eyes and Human Eye 61
5.2.3.1 Eye Preparation 61

5.2.3.2 Results 62

5.3 The Biomechanical Analysis of Aqueous Veins and Perilimbal Sclera by Three-dimensional Photoacoustic Imaging and Strain Field Calculation 65

5.3.1 System Setup 66

5.3.1.1 Perfusion System 66

5.3.1.2 Imaging System 67

5.3.2 Strain Calculation Method 68

5.3.2.1 Feature Tracking and Finite Element Mesh Generation 68

5.3.2.2 Strain Calculation 69

5.3.2.3 Validation of the Strain Measurements Using Tensile Preparation 70

5.3.2.3.1 Tensile Preparation 70

5.3.2.3.2 Results 71

5.3.2.4 Validation of The Strain Measurements on Posterior Porcine Eye 72

5.3.2.4.1 Eye Preparation 72

5.3.2.4.2 Results 72

5.3.2.5 Statistical Analysis 74

5.3.3 Results 75

5.3.3.1 Example Results of Anterior Porcine Eye 75

4.3.3.2 Example Results of Anterior Human Eye 77

4.3.3.3 Results of Statistical Analysis 77

5.4 Discussion and Conclusion 80

Chapter 6 Characterizing Intestinal Fibrosis Using Endoscopic Photoacoustic Strain Imaging 84

6.1 Introduction 84

6.2 Experiment Setup 86

6.2.1 System Setup 86
6.2.2 Data Acquisition and Analysis Method 87
6.2.2.1 Multispectral Analysis 87
6.2.2.2 PA-strain Analysis 88
6.2.2.2.1 Mathematical Demonstration of PA-strain 88
6.2.2.2.2 Procedures of PA-strain Measurement 89
6.2.2.3 Ex Vivo Microelastometer Measurements 91
6.2.2.4 Multivariate Parameter Analysis 92
6.2.2.5 Histopathology 92
6.2.3 Animal Model 93
6.3 Results 94
6.4 Discussion and Conclusion 100
Chapter 7 Conclusions and Future Plans 102
7.1 Conclusions 102
7.2 Future Plans 105
7.2.1 System Improvements 105
7.2.2 Quantification Improvements 106
Bibliography 108

List of Figures

Figure 2-1: The absorption spectra of dominant chromophores in biological tissue in the ultraviolet to infrared range. The spectrum is from the reference [20]..... 13

Figure 3-1: All-optical needle PA sensing probe setup. (a) System schematics. FOD: Fiber optic diffuser, FOH: Fiber optic hydrophone. FOHS: Fiber optic hydrophone system. (b) The needle PA sensing probe. (c) A photo showing the emission pattern of the fiber optic diffuser. (d) Intensity distribution along fiber diffusor needle in Figure 3-1(c). 0 mm and 10mm represent the positions a and b labeled in Figure 3-1(c), respectively. (e) Frequency response of the fiber optic hydrophone. This figure is taken from our published paper [120]. 20

Figure 3-2: Measurement geometries. (a) Measuring spatial sensitivity distribution of the all-optical needle probe using 1 mm diameter microsphere as a point object. Driven by 2D translation stages, the point object fixed at the tip of a positioning fiber was placed at different locations in the dashed rectangle area. (b) A photo taken during a phantom study. (c) A photo taken during the study of human prostate tissue. The dashed lines in (b) and (c) are the emission segments of the fiber optic diffusers. This figure is taken from our published paper [120]..... 21

Figure 3-3: Representative histology photographs of the measured human prostate tissue samples, including a benign sample, a nonaggressive cancer tissue with GS=6, and an aggressive cancer tissue with GS=7. 100× objective magnification. This figure is taken from our published paper [120]. 22

Figure 3-4: Process for quantitative PA analysis of tissue microstructure. (a) Representative PA signal measured by the all-optical needle PA sensing probe from a phantom containing 100 μm diameter microspheres at the concentration of 20 per mm^3. (b) Power density spectra of the signal in (a) and the illustration of the expanding window for calculating spectral slopes for different spectral segments. (c) Calculated spectral slope values as a function of the upper limit

of the expanding window. A linear fitting of this curve leads to the nonlinear spectral slope (i.e., tan θ, where θ is the angle between the fitting liner and x-axis). (d) The histogram of the signal in (a). Red line is the fitted generalized gamma distribution. This figure is taken from our published paper [120]. 24

Figure 3-5: Spatial distributions of the detection SNR achieved by the all-optical needle PA sensing probe. (a), (b), and (c) are the results measured at 1220 nm, 1370 nm, and 266 nm, respectively. White line is the 5 dB boundary at each wavelength. This figure is taken from our published paper [120]. 26

Figure 3-6: Representative RF PA signals obtained for microsphere phantoms and the quantitative processing procedures including deriving the nonlinear spectral slopes and envelope statistics. The blue and orange curves in (a-d) are from microspheres at the same concentration of 2 per mm^3, but with different dimensions of 40 μm and 200 μm, respectively. The gray and green curves in (e-h) are from microspheres with the same dimension of 10 -μm, but with different concentrations of 2 per mm^3 and 20 per mm^3, respectively. (a) and (e) RF PA signals. (b) and (f) The corresponding power spectra. (c) and (g) The derived spectral slopes using the expanding window and the quantification of the nonlinear spectral slopes. (d) and (h) The GG distributions and the corresponding parameter *a* calculated in envelope statistics. GG-*a* stands for GG parameter *a*. This figure is taken from our published paper [120]..... 28

Figure 3-7: Statistical analysis of the quantitative PA measurements. (a) Nonlinear spectral slopes and (c) GG parameter a quantified from PA measurements of microspheres with the same concentrations of 2 counts per mm^3 but varied dimesons (40, 50, 100, and 200 μm diameter). (b) Nonlinear spectral slopes and (d) GG parameter *a* quantified from PA measurements of microspheres with the same dimension (100 μm diameter) but varied concentrations (2, 6, 10, 12, and 20 microspheres per mm^3). This figure is taken from our published paper [120]. 29

Figure 3-8: SVM based categorization of the phantom study combining the nonlinear spectral slope and GG parameter *a*, (a) The classification between microsphere phantoms with the same concentrations of 2 counts per mm^3 but varied dimesons (40, 50, 100, and 200 μm diameter). (b) The classification between microsphere phantoms with the same dimension (100 μm diameter) but varied concentrations (2, 6, 10, 12, and 20 microspheres per mm^3). This figure is taken from our published paper [120]. 30

Figure 3-9: Representative RF PA signals acquired from a benign prostate tissue, a nonaggressive cancer tissue (GS=6), and an aggressive cancer tissue (GS=7), acquired at 1220 nm laser wavelength. This figure is taken from our published paper [120]. 30

Figure 3-10: Nonlinear spectral analysis and envelope statistics of representative PA signals acquired from human prostate tissues, including benign (green curves), GS=6 (blue curves), and GS=7 (orange curves), at the three optical wavelengths (1220 nm, 1370 nm, and 266 nm). (a) Power spectra of the PA signals acquired from the three prostate tissues at the three optical wavelengths. (b) Nonlinear spectral slopes calculated from the power spectra in (a). (c) GG distributions derived from the envelope statistics of PA signals acquired from the three prostate tissues at the three optical wavelengths. GG-*a* stands for GG parameter *a*. This figure is taken from our published paper [120]. 32

Figure 3-11: Statistical analyses of the nonlinear spectral slopes and the GG parameter *a* acquired from the three categories of human prostate tissues (benign, GS=6, and GS=7). (a-c) The box plots showing the quantified nonlinear spectral slopes of the three categories of tissues measured at the wavelength of 1220 nm, 1370 nm, and 266 nm, respectively. (d-f) The box plots showing the GG parameter *a* of the three categories of tissues measured at the wavelength of 1220 nm, 1370 nm and 266 nm, respectively. p values are quantified for the t-tests comparing the results between any two of the three categories. This figure is taken from our published paper [120]. 33

Figure 3-12: SVM based categorization of the human prostate tissues, including benign, GS=6, and GS=7, by combining the nonlinear spectral slope and GG parameter *a* quantified at each of the optical wavelengths (1220 nm, 1370 nm, and 266 nm). This figure is taken from our published paper [120]. 34

Figure 4-1: The needle PA sensing probe. (a) Optical components. FOD: Fiber optic diffuser. FOH: Fiber optic hydrophone. (b) Side view and (c) Top view of the needle probe in the red-dashed box in (a). The green dashed line marks the introducing angles. 700 nm laser was coupling into the illumination fiber in (c). The figure is taken from our published paper [67]. .. 40

Figure 4-2: The overview of the setup includes US guide system, laser system, hydrophone system and biopsy system. The figure is taken from our published paper [67]..... 41

Figure 4-3: The diagram of the laser and hydrophone system. (a) Hydrophone system. The hydrophone system involves a compacted detection system (labeled as 1.) and a connected FOH (labeled as 2.). The labeled objective 3. shows the disposable FOHs in a box. (b) The Laser controlling diagram of the transperineal needle PA sensing probe system. L: Convex Len. M: Mirror. FOH: Fiber optic hydrophone. FOD: Fiber optic diffuser. NIR: Near-infrared. The figure (b) is taken from our published paper [67]. 42

Figure 4-4: Detailed illustration of the experiment components in the red dashed box in Figure 3(a). The figure is taken from our published paper [67]. 43

Figure 4-5: TRUS guided insertion of the needle PA sensing probe. (a) The schematic of the US guide system for needle inserting procedures. The US images (b) and (c) were taken before and after the needle insertion, respectively. The needle was marked in the red circle in (c). The red dotted line in (a-c) represents the inserting direction. The figure is taken from our published paper [67]. 44

Figure 4-6: Histopathology of the intact prostates. (a) Gross pathology of the prostate by slicing the prostate into 4-5 mm thick samples. The blue spots are the spatial markers of the PA measurements by dye injection. The 2D contours of the cancerous regions were delineated in black. (b-c) represent the histology photos of the benign and the cancerous regions. 10× objective magnification. The figure is taken from our published paper [67]. 45

Figure 4-7: Method of PASA. (a) The frequency response of the fiber optic hydrophone system. (b) Representative calibrated PA signal power spectrum and PASA analysis. θ represents the linear slope of the PDS in the frequency range from 8 to 28 MHz. The figure is taken from our published paper [67]. 46

Figure 4-8: Example PA signals acquired at 1220 nm, 1370 nm, 800 nm and 266 nm wavelengths for insertions in the benign and cancer regions in an intact human prostate. The orange curves are the measurements in the cancerous region and the blue curves are the measurements in the benign region. The figure is taken from our published paper [67]. 47

Figure 4-9: Averaged PA signal power spectra acquired within the benign and cancerous regions at (a) 1220 nm, (b) 1370 nm, (c) 800 nm and (d) 266 nm and the corresponding linear fits. The blue curves and the orange curves are the average of all measurements within the benign and

cancerous regions, respectively. The dashed lines in all images were located at 18MHz. The figure is taken from our published paper [67]. 48

Figure 4-10: Statistics of the PASA quantifications, including (a) The linear slope and (b) The midbandfit for the spectral range of 8-28 MHz, for the benign and the cancerous regions at 1220 nm, 1370 nm, 800 nm, and 266 nm. The green line and the red line in each box represent the median and the average, respectively. The upper and lower limits of the boxes are 75 and 25 percentiles of the data distribution. The figure is taken from our published paper [67]..... 49

Figure 4-11: SVM based categorization between the benign and the cancerous groups at the wavelengths of 1220 nm, 1370 nm, and 800 nm using 49 measurements for the parameter of (a) linear slope and (b) midbandfit. The figure is taken from our published paper [67]..... 50

Figure 5-1: The integrated dual-wavelength photoacoustic microscopy system. LPDM: long pass dichroic mirror (cut-off wavelength 1150 nm), SPDM: short pass dichroic mirror (cut-off wavelength 900 nm), BS: beam splitter, SL: scan lens. The green light pass is at the wavelength of 532 nm while the red laser path is centered at the wavelength of 1200 nm. This figure is adapted from a manuscript currently in preparation. 59

Figure 5-2: Two-dimensional image at 532nm and 1200nm of the three-line phantom made of hair, fishing line and red dye line. The left image is the picture under the camera. The middle and right images were acquired at the wavelengths of 1200nm and 532nm separately. This figure is adapted from a manuscript currently in preparation. 61

Figure 5-3: Circumferential aqueous vasculatures and surrounding sclera tissues of the whole porcine eye imaged using the integrated dual-wavelength photoacoustic microscopy system in Figure 5-1. (a) The combined whole image of aqueous veins and surrounding sclera tissues. The magnified features of veins and sclera tissues of the area A and B in the white boxes in (a) are shown in (b-c) and (d-e), respectively. The cornea is represented by a white circle and a white arrow in (b) and (d). The yellow arrows represent aqueous veins. This figure is adapted from a manuscript currently in preparation. 62

Figure 5-4: Circumferential aqueous vasculatures and surrounding sclera tissues of the 2nd whole porcine eye imaged using the integrated dual-wavelength photoacoustic microscopy system in Figure 5-1. (a) The combined whole image of aqueous veins and surrounding sclera

tissues. The magnified features of veins and sclera tissues of the area A and B in the white boxes in (a) are shown in (b-c) and (d-e), respectively. The cornea is represented by a white circle and a white arrow in (b) and (d). The yellow arrows represent aqueous veins, while the blue arrows represent thin and small scleral plexus branches. This figure is adapted from a manuscript currently in preparation. 63

Figure 5-5: Circumferential aqueous vasculatures and surrounding sclera tissues of the 3rd whole porcine eye imaged using the integrated dual-wavelength photoacoustic microscopy system in Figure 5-1. (a) The combined whole image of aqueous veins and surrounding sclera tissues. The magnified features of veins and sclera tissues of the area in the white box in (a) are shown in (b) and (c), respectively. The yellow arrows represent aqueous veins. This figure is adapted from a manuscript currently in preparation. 64

Figure 5-6: Circumferential aqueous vasculature and surrounding sclera tissues of a whole human eye imaged using the integrated dual-wavelength photoacoustic microscopy system in Figure 5-1. The magnified features of veins and sclera tissues of the area A and B in the white boxes in (a) are shown in (b-c) and (d-e), respectively. The cornea is represented by a white circle and a white arrow in (b) and (d). The yellow arrows indicate aqueous veins. This figure is adapted from a manuscript currently in preparation. 64

Figure 5-7: Photoacoustic image example of a subsection of the human eye. (a) The vasculature image acquired at 532 nm. The color scale shows the depth of individual vessels. (b) A cross-section image was obtained across the yellow dotted line in (a) at the wavelength of 1220 nm. (c) A cross-section image scanned at the yellow dotted line in (a) at the wavelength of 532 nm. The color scales in (b) and (c) represent the signal intensity. The yellow arrows indicate the signals generated by melanin. This figure is adapted from a manuscript currently in preparation. 65

Figure 5-8: Experiment setup. The entire system is composed of imaging system which is the same as the system in Figure 5-1 and a perfusion system to control eye pressure. This figure is adapted from our unpublished data and restructured based on the figure presented in our published paper [147]. 65

Figure 5-9: The eye perfusion procedures. SS IOP: steady state intraocular pressure. This figure is adapted from unpublished data. 66

Figure 5-10: The examples using PAM-FEA analysis method. (a) The reference image of vein image acquired at 800 nm. (f) The reference image of the sclera tissue with black tattoo acquired at 800nm. (b), (g) The feature points extracted from reference images in image (a) and (f). (c), (h) The examples of tracked results in the reference image and the last image at the highest pressure. (d), (i) The calculated localized strain distributions in x direction. (e), (j) The averaged strains in x and y and z direction. The direction of x and y is labeled in figure (b) and (g), while z direction is perpendicular to the x and y directions. This figure is adapted from a manuscript currently in preparation. This figure is reorganized using both our published paper [147] and unpublished data. 69

Figure 5-11: Tensile validation using PAM-FEA approach. (a)(b)(c) are photo of an undeformed elastomer specimen, photoacoustic image, and mesh image composed of feature points at each corner of triangle, respectively. (d) is a photoacoustic image with overlaid points identified and tracked from the reference image (blue dots) and two deformed images stretched 0.55 mm (red dots) and 1.4 mm (green dots). (e) is the deformed mesh with the color map of the strain εXX at the end of the stretch test. (f) is the average strain εXX determined by PAM-FEA versus strain determined from the distance between the test machine grips. (g) is the average strain $|\varepsilon YY|$ (absolute value of compressive strain in the Y-direction) versus εXX determined by PAM-FEA. This figure is adapted from our published paper [147]..... 71

Figure 5-12: The calculated mechanical results. (a) The εXX and (b) The εYY in the ONH region of a porcine globe at 21 mmHg measured by a commercial imaging system. (c) The picture of the porcine globe with sprayed speckles. Photoacoustic image in grayscale is overlaid on the photo. (d) The deformed mesh of 78 elements showing the spatial variation of εYY at 21 mmHg in the XY-plane view, and (e) The εYY at 21 mmHg in the XZ-plane view. The figure (a) and (b) are from our unpublished data obtained from Dr. Alan Argento's Group, while (c)(d)(e) are from our published paper [147]. 73

Figure 5-13: The direction diagram of veins and sclera tissues in 3D image. This figure is rebuilt based on our unpublished data. 74

Figure 5-14: Perfused porcine eye (Example 1). (a) Photo of an aqueous vein and branched vein segments, (b) Corresponding photoacoustic image, (c) Tracked points in 3D of the circled vein, where blue and red points are at IOPs of 6.2 and 18 mmHg, respectively, and the green

displacements of select identical points showing clear outward movement as the IOP increases, (d) Mesh with tetrahedral elements, and the spatial strain fields of (e) Normal strain εXX at 18 mmHg and (f) εZZ at 18 mmHg. (The sclera under the red dashed line indicates a region of deeper veins.) The figure is reorganized from the figures in our previously published paper [147]. 75

Figure 5-15: Spatial averages of the aqueous vein strain components in Figure 5-14, weighted by element volume, as functions of IOP. The dashed lines are logarithmic fits to the data. The figure also includes the coefficient of determination, R^2. The figure is from our previously published paper [147]. 76

Figure 5-16: PAM-FEA analysis on human eye. (a) PAM image of a small tissue region with tracked spatial features of aqueous veins (red) and surrounding sclera (blue). Scalebar: 500 μm. (b) 3D finite element model of the aqueous vein. (c) Cross-section of the aqueous vein at 2.5 (IOP 1) and 14 (IOP 2) mmHg. (d-e) Strains of the aqueous veins and the surrounding sclera (normalized to the scleral thickness and the eye's diameter) in the directions across the vein (x) and normal to the eye surface (z). This figure is created based on the preliminary data gathered for the manuscript we are currently preparing. 78

Figure 5-17: PAM-FEA of the aqueous veins and PLS during IOP elevation in porcine eyes. (a) and (b) The strains of the aqueous veins and the adjacent perilimbal sclera measured by PAM-FEA. A: Aqueous veins. S: Perilimbal sclera. F: Fittings to a pair of representative strain curves from the same eye. The fitted curves were evaluated at 18 mmHg, i.e., the black dashed line. (c) The in-plane strains of the veins vs. those of the perilimbal sclera at 18 mmHg, with confidence intervals. (d, e) The relative cross-sectional area of the aqueous veins vs. the in-plane and out-of-plane strains in the adjacent perilimbal sclera, respectively. PLS: Perilimbal sclera. This figure is created based on the preliminary data gathered for the manuscript we are currently preparing. . 79

Figure 5-18: Deformations of the aqueous veins and PLS as functions of steady-state IOP in an eye. (a) and (b) The in-plane and out-of-plane strains in the aqueous veins (A) and perilimbal sclera (S), respectively. F: Fittings to a pair of representative strain curves from the same eye. The fitted functions were evaluated at 18 mmHg. (c-e) Relative cross-sectional areas of the aqueous veins, in-plane strains, and out-of-plane strains vs. steady-state IOPs of the eyes, respectively. (f) Scatter plot (red circles) of the measurement data points evaluated at 18 mmHg

in (c) and (d). The blue circles are the steady-state IOPs predicted from the relative aqueous vein strains and in-plane perilimbal sclera strains using the linear regression model derived using the red circles. RMS: Root of mean square. PLS: Perilimbal sclera. This figure is created based on the preliminary data gathered for the manuscript we are currently preparing. 81

Figure 6-1: The diagram of experiment design. (a) The system setup of prototype endoscopic PA-US catheter probe from our previous published paper [244]. The structures marked with green boxes on top are magnified in the bottom. 1) Side-firing fiber optics with 800 μm core. 2) Illumination delivered by the side-firing fiber optic. 3) US array. 4) Semi-rigid tube to hold the relative positions of the side-firing fiber and the US transducer. 5) Hydrostatic balloon. 6) Three-way stopcock. 7) T adapter. 8) Hydrostatic pump. (b) Images of the probe head in its fully inflated and expanded states as its diameter increased from 8 mm to 12 mm. Figure (b) is from our unpublished data. 86

Figure 6-2: Data processing processes in PA-strain analysis. In the data processing pipeline for PA-strain analysis, the first step involves tracking feature points on the upper and lower boundary of the intestinal tissue in US images over time (as indicated by red dots in the left image), while the longitudinal borders of the tissue are marked by yellow dashed lines. In the second step, co-registered regions in PA images are extracted based on the tracking results from step one. Finally, the normalized changes in the average PA amplitudes of the extracted sections are computed as the strain increases. The average PA amplitude was normalized based on the initial average PA amplitude (Strain=0). The strain is determined by measuring the thickness changes between the upper and lower boundaries in US images. The scattered points are then fitted linearly, and the averaged PA amplitude at a strain equal to 0.15 is extracted and input into Equation 6-3 to calculate the Young's modulus. The figure is from our unpublished data. 91

Figure 6-3: The procedures of microelastometer measurements. (a) The setup of the microelastometer system. (b) The contact area of the indenter. (c) The measured stress and strain distributions of two tissues. The blue line and green line are the measured results of chronic and acute tissue, respectively. The linear fitting (orange lines are the fitted region, and the yellow dashed lines are the fitted results) was applied between 0 and 15% strain. The figure is from our unpublished data. 92

Figure 6-4: Histopathology examples of tissues at scanned positions. (a) The histology example at normal position with score equal to 0. (b) The histology example at low fibrosis position with score equal to 2. The arrow indicates the focal areas of fibrosis. (c) The histology example at high fibrosis position with score equal to 7. The arrow denotes high fibrosis areas with collagen scars. The Histopathology examples are taken from our unpublished data. 93

Figure 6-5: Examples of *in vivo* compression using PA-strain imaging in rabbits with normal, low, and high fibrosis. The images include US and PA images taken at the beginning, middle, and end of compression at low and high fibrosis locations. The US images are displayed in a gray colormap, while the PA images are displayed in a hot colormap. The examples are taken from our preliminary results. 95

Figure 6-6: The measured PA-strain with strain increases of examples in Figure 6-5. The blue dotted line and the orange dotted line represent the results of high fibrosis and low fibrosis, respectively. The examples are taken from our preliminary results. 96

Figure 6-7: The PA-US dual images of rabbit colon acquired at the wavelength of 720 nm and 1310 nm for spectral unmixing. The images in the three columns are B-mode US images (in gray colormap), PA images at 800 nm (in red colormap), and PA images at 1310 nm (in green colormap). The PA-US pictures in the three rows were scanned in the normal, low, and high fibrosis positions. The average PA amplitudes used for spectral unmixing were calculated in the green dashed regions. The examples are taken from our preliminary results. 97

Figure 6-8: The present study investigates the distribution of three key parameters related to fibrosis states. (a) The concentration ratio between collagen and hemoglobin, (b) The Young's modulus obtained from microelastometer measurements, and (c) The Young's modulus obtained from PA-strain, as a function of increasing score ranging from 0 to 7. The examples are taken from our preliminary results. 97

Figure 6-9: Linear Regression of Young's Modulus measured by microelastometer measurements and PA-strain analysis. The data are taken from our preliminary results. 98

Figure 6-10: Boxplots to differentiate the normal, the low fibrosis, and high fibrosis using three parameters. (a-c) Boxplots of the normal, low and high fibrosis using microelastometer

measurements, PA-strain measurements, and concentration ratio between collagen and hemoglobin, respectively. The statistical analysis was based on our preliminary results. 98

Figure 6-11: ROC curves of 5-fold SVM using single parameter or multi-variable parameters to differentiate low fibrosis and high fibrosis. It includes the ROC curves using microelastometer measurements, concentration ratio of collagen and hemoglobin, PA-strain, and the combination of the last two. The classification was based on our preliminary results..... 99

List of Tables

Table 3-1: Correlation Between Quantitative Measurements and SVM Results. The data is taken from our published paper [120]. 34

Table 4-1: Disease conditions of the sampled locations. The table is taken from our published paper [67]. 45

Table 4-2: The SVM statistical results using single wavelength or combined wavelengths. (5-fold cross validation, 80% learning, 20% testing) The table is taken from our published paper [67]. 51

Table 6-1: The scoring system of fibrosis. Normal: score=0; Low Fibrosis: score=1-3; High Fibrosis: score=4-7. 93

Table 6-2: The sample size for each score using the scoring method shown in Table 6-1..... 94

Table 6-3: The correlations between each pair of the parameters. 99

Table 6-4: The area under the curve (AUC) for each ROC curve in Figure 6-11. Solid line displays the AUCs under the ROC curves in Figure 9. 95% CI represents the AUCs of the positive and negative bound of 95% confidence interval for each ROC curve in Figure 6-11. CI: confidence interval. 100

List of Abbreviations

Acoustic resolution photothermal microscopy – AR-PAM

American national standard institute – ANSI

Area under curve – AUC

Artificial intelligence – AI

Balanced salt solution – BSS

Computed tomography – CT

Deoxygenated hemoglobin – HB

Fineite element analysis – FEA

Generalized gamma – GG

Gleason Score – GS

Indocyanine green – ICG

Intraocular pressure – IOP

Light emitting diodes – LEDs

Magnetic resonance imaging – MRI

OCT-Angiograpgy – OCT-A

One dimensional – 1D

Optical coherence tomography – OCT

Optical parametric oscillator – OPO

Optical-resolution PA microscopy – OR-PAM

Outer diameter – OD

Oxygen saturation – sO2

Oxygenated hemoglobin – HBO2

PA endoscopy – PAE

PA imaging – PAI

PA spectral analysis – PASA

PA tomography – PAT

Perilimbal sclera – PLS

Photoacoustic - PA

Positron emission tomography – PET

Prostate cancer – PCa

Radio frequency – RF

Receiver operating characteristic curve – ROC

Region of interest – ROI

Signal-to-noise ratio – SNR

Support vector machine – SVM

Three dimensional – 3D

Trinitrobenzenesulfonic – TNBS

Two dimensional – 2D

Ultrasound – US

Abstract

Photoacoustic (PA) sensing and imaging combines the optical resolution of laser light with the deep acoustic penetration of ultrasound waves to enable high-resolution imaging of deep tissues. PA signals are able to provide rich information about tissue composition and other physiological parameters, making PA imaging a powerful tool for biomedical research and clinical applications. This study aims to explore the quantification of tissue characteristics in PA signals or images for biomedical and pre-clinical applications.

In Chapters 3 and 4, we developed a prototype interstitial all-optical needle PA sensing probe to facilitate the clinical translation of prostate cancer. We validated the performance of the PA needle probe on microsphere phantoms and *ex vivo* human prostate tissue slices, effectively distinguishing between aggressive and non-aggressive tissues. We applied the needle probe to intact human prostates *ex vivo* to simulate transrectal ultrasound guided transperineal prostate biopsy procedures and achieved an accuracy close to 90% in differentiating between benign and cancerous regions.

In Chapter 5, we developed a photoacoustic microscopy (PAM) and finite element analysis (FEA) approach to characterize the biomechanical behaviors of the aqueous veins and perilimbal sclera, and their roles in the regulation of intraocular pressure (IOP). The optical resolution PAM system captured the separative 3D architectures of the sclera and the aqueous veins perfused with indocyanine green. FEA computed the strains of aqueous veins and surrounding perilimbal sclera tissues. The performance of the PAM-FEA has been validated by tensile test and *ex vivo* eyes. The findings indicated that the stiffness of perilimbal sclera tissue influences and constrains the deformations of aqueous veins during IOP regulation.

In Chapter 6, we employed two measurements to quantify intestinal fibrosis *in vivo* in a large cohort of rabbits: the collagen-to-Hb ratio, quantified by spectroscopic analysis, and tissue stiffness, quantified by PA-strain using our PA-US endoscopic catheter probe. The results

demonstrated that both measurements could significantly differentiate between low and high histological fibrosis. PA-strain was found to be positively correlated to the Young's Modulus measured *ex vivo* using a microelastometer, exhibiting a correlation coefficient of 0.84.

Overall, this study demonstrates the sensitivity and potential of quantifications using PA imaging or sensing, which can provide important information for disease diagnosis and treatment management. The results of Chapters 3-6 provide specific examples of the applications of PA imaging and sensing in prostate cancer diagnosis, intestinal fibrosis quantification, and characterization of the biomechanical behaviors of structures in the eye that regulate intraocular pressure.

Chapter 1 Introduction

1.1 Background

Biomedical imaging has played a critical role in the diagnosis of disease over the past few decades, substantially improving diagnostic accuracy and efficiency. In clinics, histopathologic analysis after tissue dissection by biopsy is the gold standard for diagnosis. This involves examining the suspected tissue to detect abnormal tissue cells or component alterations on a micro- or sub-micro scale. However, the process is time-consuming and carries the risk of bleeding and infection at the tissue extraction sites. Furthermore, the characterization and quantification of tissue structures or components are increasingly valuable in disease diagnosis using artificial intelligence (AI). Therefore, biomedical imaging technologies that can measure tissue structures provide a non-invasive and non-destructive option for disease diagnosis while maintaining high accuracy. The applications of these imaging methods can connect the diagnostic information and histopathology results.

Photoacoustic (PA) imaging (PAI), also known as optoacoustic imaging, is a biological imaging modality that combines optical contrast and acoustic penetration. To generate a PA signal, laser pulses are employed to illuminate the tissues, and the absorption of the complex tissue components converts the optical energy into acoustic energy due to the PA effect [1]. Compared with other imaging techniques, PA imaging has several advantages:

(a) PAI offers several advantages over traditional clinical tomography imaging techniques such as magnetic resonance imaging (MRI), computed tomography (CT), and positron emission tomography (PET). These advantages include faster imaging, lower cost, and a more compact system. Furthermore, PAI is non-ionizing, making it a safer alternative to CT and PET, which require the use of radioactive materials [2]. PAI only requires two major components, the light, and the US system, making it a simpler and more accessible option. Numerous early studies have successfully combined PAI with current clinical ultrasound equipment or platforms, resulting in

dual-modality US-PA imaging that has been applied to humans *in vivo*, thus making it a viable option for clinical use [3, 4, 5, 6]. Additionally, the use of light emitting diodes (LEDs) as a source of illumination has been investigated [7, 8, 9, 10], which further enhances the safety, portability, cost-effectiveness, and clinical translation of PAI systems.

(b) In contrast to ultrasound (US) imaging, PAI provides the unique ability to independently image endogenous chromophores in tissues, including oxy-hemoglobin (HBO2), deoxy-hemoglobin (HB), lipid, and melanin [11, 12, 13]. This capability is attributed to the significant difference in optical absorptions relative to acoustic impedance in tissues [14]. Furthermore, chromophores can also be dyes or nanoparticles that enhance the image contrast of specific tissue components [15]. To differentiate the chemical compositions of tissues, multi-spectral analysis methods are typically utilized in PAI. A thorough discussion of multi-wavelengths PA imaging and analysis will be presented in chapter 2.2.2.

(c) PAI offers a distinct advantage over other imaging modalities by providing the ability to image deep tissues with moderate resolution and shallow tissues with high resolution. The development of PA tomography (PAT), which utilizes US signal transmission, has allowed for imaging up to 70mm in depth using high-energy laser pulses [16, 17]. In order to overcome this limitation and facilitate the clinical applicability of PA imaging for internal organs, the endoscopic PAT imaging approach is commonly employed [18, 19]. Nevertheless, the resolution of endoscopic PAT is primarily dependent on the frequency of the US transducer. Thus, endoscopic optical-resolution PA microscopy (OR-PAM) was proposed to enable the collection of high-resolution and relatively high frequency information, such as micro-vascular architecture and micro-endogenous tissue chromophores [65, 234].

Since the microstructure is a crucial indicator to characterize tissues [21], the qualitative and quantitative analysis of high contrast PA signals plays a pivotal role in the pathological diagnosis of diseases [22]. PA signals in tissue, according to the PA effect theory, are the product of local absorption distributions and optical fluence [23]. Therefore, conventional PA images have been qualitatively examined to gather structural information, and some studies have proposed to recover quantitative physiological and molecular information. For instance, Jang. Group demonstrated the extraction of the optical absorptance coefficients from PA images of heterogenous media [24, 25]. L.V. Wang, Wang. Groups and many other groups successfully

unmixed physiologically relevant tissue parameters such as Hb, HbO2 and water (H2O) using multi-wavelength PA imaging [26, 27]. Our previously proposed PA spectral analysis (PASA) has shown its ability in quantifying absorber dimensions and concentrations for characterizing random tissues [28, 29, 30, 31, 32, 33, 34, 35, 36]. Dr. Michael C. Kolios's group has also proposed to introduce envelope statistics to PA quantitative analysis [37, 38]. In addition, mechanical parameters are as well an important biomarker for soft tissues characterization. Deformation of tissues can be tracked in series of PA images to reveal changes in the texture of biological tissues over the progression of the disease [39, 40, 41].

Background signals called speckles provide valuable information about tissue microstructures in addition to high contrast real-existing PA signals. Pioneering studies have investigated these speckles, which appear as granular patterns in reconstructed PA images. These granular patterns are a result of both physical absorbers with small dimensions outside the frequency range of US transducers and the interference of PA signals as they propagate through biological tissue [33, 42, 43]. While these patterns are often treated as noise that may lead to reduced image contrast, details blurring, and enhanced local pseudo features [47, 48], they have also been widely used for disease diagnosing as they reflect tissue microstructures. Even though PA wave propagation is similar to that of US wave propagation, PA signals cover a broader US bandwidth. As a result, granular patterns encode rich target information that represents tissue micro-information in both the RF PA signal and 2D/3D PA microscopy image [33]. Examples of the use of these patterns include the speckle-based cardiac function analysis [49], the assessment of the burn depth [50], and early diagnosis of coronary artery disease using speckle tracking echocardiography [51].

In summary, the advantages of the PA signal enable tissue characterization by quantifying random microstructure information such as characteristic size, number density, and mechanical parameters. This study aims to extract these meaningful parameters from PA signals in three different applications. The first application involves the classification of prostate cancer (PCa) at various stages using multi-wavelength PA quantitative analysis on PA radio frequency (RF) signals in deep tissues. The second application involves tracking the three-dimensional deformation of aqueous veins and sclera tissues separately in the regulation of intraocular pressure (IOP) in human eyes using dual-wavelength PAM. The third application involves tracking the strain changes in US images and calculating PA signal decrease in the co-registered PA images to quantify tissue stiffness.

1.3 Research Objectives and Thesis Outlines

The field of biomedical imaging presents diverse modalities, each with its unique advantages. PAI, in particular, has demonstrated exceptional capabilities in providing high-resolution, functional and molecular information. Moreover, quantitative analysis based on tissue characteristics is widely recognized as a crucial tool in assisting disease diagnosis and treatment management. There are numerous proposed parameters in the quantification of PA signal that are highly associated with tissue micro-information. One such example is the characteristic size and density, which are two basic properties of aggregation cells in biological tissue and are effective indicators for tissue classification. Quantitative analysis is a valuable tool to observe the less significant contrast fluctuations caused by changes in dimension and concentration of the microstructures within the region of interest (ROI) [52]. In light of this, the primary objective of this dissertation is to advance the quantitative analysis of tissue characteristics using PAI.

Chapter 2 provides a comprehensive overview of various PA techniques, including 1D sensing, PAT and PAM, and PA endoscopy. This chapter delves into the underlying physical and mathematical principles of PA contrasts and speckles, providing a thorough understanding of the technology. In addition, it provides a literature review of PA quantitative analysis, covering morphological analysis, multi-spectral analysis, elastography analysis, and multi-variate parameter classification. Moving forward, the thesis explores three key applications of tissue characterization using PA methods in the subsequent three chapters:

The first application discussed in Chapters 3 and 4 aims to evaluate PCa progression using an interstitial needle PA sensing probe that enables high-resolution and deep tissue penetration by acquiring 1D signals. Although the probe sacrifices the acquisition of 2D images, its unique capability to detect signals reflecting micro-structures or histological related information demonstrates its potential as an effective tool for detecting and assessing prostate cancer progression. In this chapter, we first describe the probe's design, which is compatible with standard prostate biopsy procedures, followed by an explanation of the quantification methods used. To verify the probe's efficiency, we conducted tests on microsphere phantoms, *ex vivo* human prostate tissues, and intact prostates. In Chapters 3 and 4, we compared the quantitative tissue measurements to histology results and confirmed the probe's ability to detect and assess

the progression of prostate cancer, distinguishing between normal and cancerous tissues, as well as non-aggressive and aggressive tissues.

Chapter 5 presents the second application, which involves the evaluation of the biomechanics of aqueous veins and perilimbal sclera in porcine eyes using multiwavelength PAM. The objective of the study is to investigate the biomechanical functions of aqueous veins and surrounding perilimbal sclera tissues separately to facilitate the regulation of IOP. The chapter begins by introducing the background and significance of studying the biomechanics of these two anatomical structures. Subsequently, the system setup and analytical methods used are elaborated upon. The results demonstrate the capability of the proposed dual-wavelength PAM imaging approach to separately investigate the biomechanics of these two components. In addition, statistical analyses of calculated strains using the proposed FEA strain analysis method were conducted in the results section to investigate the relationship between the behavior of aqueous veins and surrounding perilimbal sclera tissues.

In Chapter 6, endoscopic photoacoustic-strain imaging is implemented as the third method to characterize intestinal fibrosis, with the objective of investigating the correlation between multiple imaging findings and progressive fibrosis conditions in Crohn's disease using endoscopic imaging on a large cohort of rabbits *in vivo*. The chapter begins by providing the background for the differentiation of intestinal fibrosis states, followed by a detailed description of the PA endoscopy design and the rabbit disease model. The outcomes of the study are presented using both multi-spectral analysis and elastography analysis. The chapter demonstrates the potential of endoscopic PA-strain imaging as a promising diagnostic tool for intestinal fibrosis, providing insights into the assessment of disease progression.

At the end of the thesis, Chapter 6 presents the conclusion of the study along with a discussion of potential areas for future research.

Chapter 2 Review of Quantification in Photoacoustic Methods

2.1 Theory of Photoacoustic Imaging

2.1.1 Photoacoustic Modalities

PA sensor is the most basic way of receiving PA signals in one dimension (1D), in which a diffused laser at a certain wavelength illuminates the investigated location of a sample [53]. Detected by a wide-angle based US transducer, A-mode PA signals contain volume resolved information of samples. Unlike other imaging techniques, PAS does not need complex design or image reconstruction. The use of fiber-optic sensing systems in biomedical applications has become increasingly popular due to their small size, compactness, ease of use, and portability [54, 55, 56].

PA imaging in two dimensions (2D) and three dimensions (3D) can be accomplished by altering the optical illumination and acoustic detection methods. According to existing reviews, PA systems are typically categorized into three types: tomography, microscopy, and endoscopy [57, 58, 59, 60]. The core components of PA tomography (PAT) include wide-field optical illumination and unfocused US detections. To achieve at least 2D imaging, a linear array US transducer or moveable single-element US transducer is employed [61, 62]. In addition, more complex structures of US transducers, such as ring, hemispheric, and 2D matrix arrays, have also been developed to capture 3D information [17, 62]. The resolution of the reconstructed sample architectures is limited by the frequency detection range of the US transducers [16]. In summary, PAT has relatively low resolution in hundreds of microns but high imaging depth, which is as deep as several centimeters [16, 19].

PA microscopy systems are divided into two categories based on their focus types: Optical Resolution Photothermal Microscopy (OR-PAM) and Acoustic Resolution Photothermal

Microscopy (AR-PAM) [63]. The axial resolution for both systems is determined by the frequency bandwidth of the US transducer, the axial resolutions for both systems, but the generation of lateral resolution generation differs [64]. AR-PAM, also known as Photothermal Mesoscopy, uses wide-field illumination and tightly focused ultrasonic transducers with a wide bandwidth. The design allows for improved resolution but decreased penetration depth [58]. The spatial resolution of the AR-PAM is in the tens of microns, while the imaging depth is several millimeters [57, 58]. In contrast, OR-PAM uses focused laser beams for illumination, achieving better lateral resolution on the micron scale at the expense of laser penetration depth. As such, AR-PAM is the bridge connecting the PAT and OR-PAM in terms of two critical geometry configurations: imaging depth and imaging resolution [57].

Despite the benefits offered by the aforementioned PA systems, visualizing deep biological tissues remains a challenge. This is due to two main reasons: the limited light penetration and acoustic signal attenuation, particularly for high-frequency signals. To overcome these obstacles, PA endoscopy (PAE) based on PAT or PAM was proposed [18, 65]. PAE boasts the advantages of portability and miniaturization, making it well-suited for targeting internal or deep organs and tissues [18]. PAE has shown promise in medical fields such as gastroenterology and female or male's reproductive systems [66]. In gastroenterology, PAE provides high contrast and resolution for visualizing the gastrointestinal track, including esophagus, stomach, and colon [18, 67]. In gynecology, PAE has been used to visualize the cervix, uterus, and ovaries, providing important information for the diagnosis and treatment of reproductive system disorders [68]. Additionally, PAE has been used to image the prostate gland and differentiate prostate cancer non-invasively in the male reproductive system using a transrectal array PA probe [69].

While photoacoustic elastography imaging has demonstrated potential for detecting structures in deep organs, these structures often have dimensions ranging from tens to hundreds of microns. This presents a challenge for resolving these structures when they are positioned tens of millimeters away from high-frequency ultrasound (US) transducer arrays. To address this issue, we developed an interstitial measurement approach in Chapters 3 and 4 of this thesis [67]. This approach delivers sufficient optical energy and captures high-frequency photoacoustic signal components that encode microscopic architectural information within tissues.

The following chapter will explain the principle of PA generation, which involved three key steps. Initially, the pulsed laser is absorbed by the illuminated tissue. The absorbed optical energy is then converted to heat, which leads to the formation of a localized pressure wave. Finally, the acoustic or pressure waves that propagating from the site of initiation are detected by the US transducer [70].

2.1.2 Photoacoustic Imaging Contrast

2.1.2.1 Photoacoustic Signal Generation

After the illumination, the localized heat deposition resulting from the conversion of the optical energy in the tissues can be described by Equation 2-1 [71, 72]:

$$H(\vec{r},t) = \eta_{th}\mu_a F(\vec{r},t) \quad \text{Equation 2-1}$$

where μ_a represents the optical absorption coefficient, and $F(\vec{r},t)$ denotes the optical fluence at the location $\vec{r}$ with respect to time. η_{th} represents the percentage of optical energy converted into heat. The resultant laser heating then causes the fractional volume expansion, which can be expressed using Equation 2-2 [70]:

$$\frac{dV}{V} = -kp + \beta T \quad \text{Equation 2-2}$$

where V is the volume of the localized position, k is the isothermal compression coefficient, β is the thermal coefficient of volume expansion, and T is the temperature. The volume changes at illuminated positions are determined by two factors during laser illuminating: heat confinement and stress confinement [16, 73]. Thermal confinement is also referred to as thermal relaxation time τ_{th} as shown in Equation 2-3 [16, 74]:

$$\tau_{th} = \frac{d_c^2}{4D_T} \quad \text{Equation 2-3}$$

where D_T is the thermal diffusivity, and d_c is the characterized spatial resolution. According to reference [75] , the value of D_T for soft tissue is approximately 0.14 mm^2 per second. Stress confinement is defined by the stress relaxation time τ_{st} indicating the pressure propagating [16, 74]:

$$\tau_{st} = \frac{d_c}{v_s} \quad \text{Equation 2-4}$$

where v_s denotes the speed of sound. According to reference [76], the average speed of sound in soft tissues is approximately 1540 m per second. In PAT, the characterized spatial resolution d_c is always lager than 50 μm. Using this threshold value in Equations 2-3 and 2-4, the calculated thermal and stress confinements are $\tau_{th} = 50\ \mu\text{m} \times 50\ \mu\text{m}/4/0.14\ \text{mm}^2/\text{s} = 4.46\ \text{ms}$ and $\tau_{st} = 50\ \mu\text{m}/1540\ \text{m/s} = 32.47\ \text{ns}$, respectively. Since the pulse duration of the typically used laser is smaller than 10 ns, both confinements are reached. In this case, the volume expansion of the illuminated region can be neglected. The initial pressure generated can be expressed using Equation 2-5:

$$p_0(\vec{r},t) = \frac{\beta T(\vec{r},t)}{k} = \Gamma \mu_a \eta_{th} F(\vec{r},t) \qquad \text{Equation 2-5}$$

where $\Gamma = \frac{\beta}{k\rho C_v}$ is defined as Grueneisen parameter, which is positively related to the temperature [74]. In PAM, where the resolution is in the scale of micrometers, the stress confinement at $d_c = 1\mu m$ equals to $\tau_{st} = 1\ \mu\text{m}/1540\ \text{m/s} = 0.65\ \text{ns}$. The result indicates that PAT only satisfies thermal confinement.

The general propagation of PA signals can be described by the equation given below [77]:

$$\left(\Delta^2 - \frac{1}{v_s^2}\frac{\partial^2}{\partial t^2}\right) p(\vec{r},t) = -\frac{\beta}{k v_s^2}\frac{\partial^2 T(\vec{r},t)}{\partial t^2} \qquad \text{Equation 2-6}$$

This equation relates the pressure changes and temperature changes at the location $\vec{r}$ and time t. As discussed earlier, thermal confinement is always maintained. The heat diffusion equation, $H(\vec{r},t)$, in this case is expressed as:

$$\rho C_v \frac{\partial T(\vec{r},t)}{\partial t} = H(\vec{r},t) \qquad \text{Equation 2-7}$$

Where ρ denotes the mass density, and C_v denotes the specific heat capacities at constant volume. Equation 2-7 describes the thermal energy converted per unit volume and per unit time. By combining Equation 2-6 and 2-7, the final solution, as expressed in multiple papers, is given by [57, 77]:

$$p(\vec{r},t) = \frac{\beta}{4\pi C_p}\int d\vec{r}' \frac{1}{|\vec{r}-\vec{r}'|}\frac{\partial H(\vec{r}',t')}{\partial t'}\Big|_{t'=t-|\vec{r}-\vec{r}'|/v_s} \qquad \text{Equation 2-8}$$

where C_p represents the specific heat capacities at constant pressure, and $\vec{r}'$ and t' represent the source location and time. Equation 2-8 represents the measured pressure wave at the location $\vec{r}$ and time t.

2.1.2.2 Photoacoustic Speckles

In a reconstructed PA image, the pattern is composed not only of the observed objectives such as blood vessels, tumors, or other tissue structures, but also includes random noise patterns known as speckles. These speckles are generated by the summation of randomly generated PA signals of sub-resolution absorbers. This is similar to the generation theory of US speckle signals but has two main differences [72]: (a) the initial pressure of US signals has both negative and positive values, but the initial PA signals are all positive; (b) US speckles are caused by sub-resolution scatters, while PA are caused by absorbers.

In a A-scan of the PA imaging, the amplitude $A(t)$ can be expressed as the convolution between the particle impulse response $p_i(t)$ and the system impulse response $h(\vec{r}, t)$ in time domain [72]:

$$A(t) = \sum_{i=1}^{n} p_i(t) *_t h(\vec{r_i}, t - |\vec{r_i}|/v_s) \quad \text{Equation 2-9}$$

where we assume a total of n particles $(r_1, r_2. r_3, \dots r_n)$ and $\vec{r_i}$ denoting the position of the i_{th} particle relative to the detector. If we assume the particles in the volume V has the particle density of ρ, the average power of the A-scan can be obtained by [72]:

$$< P(t) >= \rho \int_V \langle\langle \left(p_i(t) *_t h(\vec{r}, t - |\vec{r}|/v_s)\right)^2 \rangle\rangle_i \, d\vec{r}^3 + \rho^2 \langle b_i(t) b_j(t) \rangle_{i \neq j} \quad \text{Equation 2-10}$$

$$b_i(t) = \langle p_i(t) \rangle *_t \int_V h(\vec{r}, t - |\vec{r}|/v_s) d\vec{r}^3 \quad \text{Equation 2-11}$$

The first term in Equation 2-10 represents speckles because it is the sum of the power generated by the randomly distributed absorbers. The second term describes the correlation between absorbers, generating only from the boundary features. The value of $p_i(t)$ is contingent upon the absorption characteristics of the tissue absorbers. As a result, it is subject to stochastic processes of particle impulse response, which invariably lead to a positive initial pressure. $\langle\rangle$ denotes the average of the random processed, $\langle\rangle_i$ is averaging over all particles, while. $\langle\rangle_{i \neq j}$ is the average over all particle pairs.

To quantify the visibility of speckles, the term R is defined as the ratio between the average speckle power and the average boundary feature. In this regard, R is inversely proportional to square root of particle density $\sqrt{\rho}$, indicating the speckle is visible when particle density is low or moderate. According to Equation 2-10, Equation 2-12 is provided to describe this term:

$$R = \sqrt{\frac{\int_V \langle\langle \left(p_i(t) *_t h(\vec{r}, t-|\vec{r}|/v_s)\right)^2 \rangle\rangle_i d\vec{r}^3}{\rho \langle b_i(t) b_j(t) \rangle_{i \neq j}}} \qquad \text{Equation 2-12}$$

In this equation, Due to the heterogeneous nature of tissues, the PA signal contains a wide range of acoustic frequencies. However, due to practical limitations, receivers are usually designed with a limited bandwidth. Despite this limitation, simulations described in reference [78] suggest that even band-limited data can produce speckle-like patterns that contain information about unresolved absorbers. This finding encourages the utility of PA speckles for morphological analysis or further functional analysis in biological research, which will be discussed in the next Chapters.

2.2 Quantifications in Photoacoustic Signals

The quantification of PA signals or images aims to extract tissue-specific information and is of increasing importance in biomedical imaging for diagnostic purposes. The utilization of computer technology in conjunction with PA quantification has become critical for achieving diagnostic efficiency [79]. The analysis methodology typically comprises two steps: feature extraction and classification. This chapter will cover four categories of quantification: morphological analysis, multi-spectral analysis, elastography analysis, and multivariate parameter classification.

2.2.1 Morphological Analysis

In PA imaging, tissue morphology refers to the spatial distribution of optical absorption or optical scattering properties of tissues, as revealed by the PA signal or image. The extraction of shape features, such as boundary, location, and size, represents a fundamental application of PAI for directly collecting tissue structural information from reconstructed images. The high-contrast features in reconstructed PA images reflect the existence of physically present microarchitectures in tissues. These extracted image features are widely utilized for object recognition and growth

monitoring. For instance, PA imaging has a distinct advantage in mapping vasculatures, as hemoglobin exhibits high absorption relative to surrounding tissues [80, 81, 82], thereby serving as a vital indicator of tumor growth through vasculature development [83, 84]. Furthermore, malignant tumors with irregular shapes can be differentiated from benign tumors with regular shapes using PA images [85, 86].

In addition to the distribution of physically existing structures, tissue morphology in PA imaging may also include speckle patterns that arise from the interference of acoustic signals. Unlike US speckles, PA speckles result only from positive interference, leading to a suppression of most speckles in PA imaging compared to US imaging. Despite the complexities of tissues and the use of band-limited receivers, speckle patterns still contain valuable information that does not correspond to real structures. Therefore, the morphology analysis discussed in this section focuses on envelope statistics and spectrum analysis of both these speckle patterns and real structures to enable tissue characterization.

(1) Envelope Statistics

Envelope statistics is a method of analyzing the statistical properties of signals, which describes the distribution of the amplitudes of the signal envelopes and quantifies the randomness of the signal. The mean, standard deviation, spread or dispersion, and skewness or asymmetry of the envelope distribution can be used to characterize the signal's average behavior, reflecting the physical size, concentration, and density in tissues [88, 89]. Envelope statistics have several applications in tissue characterization. The erythrocyte aggregation level in human blood can be observed and quantified using the envelope fitting [90]; multiple groups using the envelope to measure the blood oxygenation levels and blood flow, and this may help differentiate between normal and hypoxic tissues [91, 92, 93]. Envelope statistics have also been applied to detect tumor or inflammation areas by analyzing local tissue structure changes, including vasculatures or other tissue components [33].

(2) PA Spectrum analysis

The objective of PA spectroscopic techniques is to determine the frequency components of PA signals. In a study by Dr. Xu and colleagues [11], a linear fitting approach was suggested for measuring tissue microstructure information based on the power density spectra of PA

signals. The authors showed, through theoretical and experimental means, that there is a strong correlation between the size of absorbers and the linear fitting parameters, such as slopes and mid-band fits [11]. The results demonstrated the feasibility of the proposed method in differentiating tissue microstructures. The spectrum analysis has as well been applied in tissue characterization, tumor detection, and even functional analysis [94, 95, 96].

2.2.2 Multi-spectral Analysis

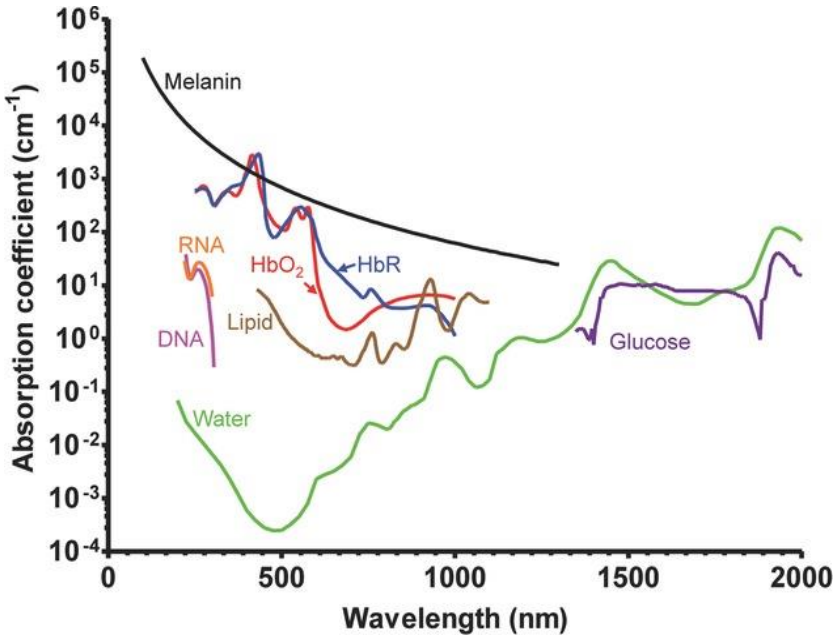


Figure 2-1: The absorption spectra of dominant chromophores in biological tissue in the ultraviolet to infrared range. The spectrum is from the reference [20].

The chromophores in tissues have unique spectral characteristics, exhibiting distinctive absorption features in different regions of spectrum. Figure 2-1 presents the absorption spectrum of the dominant absorbers in biological tissues from the reference [20] covering the wavelength region from ultra-violet to infrared. In this figure, chromophores have characteristic distributions and peaks in specific regions of the spectrum that can be used to distinguish them from other chromophores or tissue components. According to Equation 2-5, the PA signal is proportional to the absorption coefficient at a given wavelength. Thus, the averaged absorption coefficient in the imaged volume acquired at a single wavelength can be mathematically expressed using the linear superposition of various chromophores in Equation 2-13:

$$\mu_a(\lambda) = \sum_i \varepsilon_i(\lambda) \cdot c_i$$ Equation 2-13

Where $\boldsymbol{\varepsilon_i}$ represents the molar extinct coefficient of different chromophore in the unit of $cm^{-1}M^{-1}$ and c_i represents their respective concentrations. By employing multi-spectral photoacoustic imaging techniques, it is possible to capture the photoacoustic signal at various wavelengths, which can then be used to derive a system of linear equations through inversion methods [3, 95, 96, 97]. The solution to this system can be utilized to determine the spatial distribution or concentration of various chromophores, including but not limited to oxygenated (HBO2) and deoxygenated hemoglobin (HB), lipid and collagen, water, and melanin. Furthermore, this approach enables the extraction of valuable physiological and functional information pertaining to the tissue, such as the levels of Hb, HbO2, oxygen saturation (sO2), and total Hb [98]. These parameters are useful for a wide range of biomedical applications, including cancer detection and characterization, functional brain imaging, and drug delivery monitoring.

2.2.3 Elastography Analysis

Elastography analysis employs quantitative measures of tissue elasticity to visualize and assess the mechanical properties of biological tissues. Even though PA and elastography studies have started earlier in 1990s, the combination of PA and elastography is a more recent development and a relatively new area, with research starting to gain momentum in the early 2010s [98]. Since then, there has been significant progress in developing new techniques and applications for elastography PA, but it is still an emerging field with ongoing research and development. There are three vital steps in PA-based elastography:

1) Mechanical stimulation: the first step is to apply a mechanical stimulus to the imaging area of the tissue. The external mechanical stimulation, like deformation or vibration, can be achieved using various techniques, such as acoustic radiation force [99, 100], shear waves [98, 101, 102], physical static/dynamic compression [103].
2) Imaging: the second stage is to capture mechanical variations utilizing imaging modalities, such as the PA imaging technique in this study. When tissues are mechanically stimulated, they generate shear waves that propagate through the tissue. These shear waves cause small changes in the local density and compressibility of the

tissue, which in turn affects the speed of sound in the region. The optical absorption properties of the tissue also change due to the deformation caused by the shear waves. As a result, the tissue generates PA signals that can be detected and processed to reconstruct an image of the shear wave propagation within the tissue. By analyzing the characteristics of the shear waves, such as their speed and amplitude, the mechanical properties of the tissue, such as elasticity and stiffness, can be determined [104]. In addition to measuring shear waves, the structural deformation measured using PA imaging also enables the derivation of tissue elasticity, such as strains [103, 105] .

3) Imaging analysis: The last step is to quantify the tissues' mechanical properties from detected PA signals. This step involves applying mathematical algorithms to obtain tissue elasticity distributions which can be further visualized and interpreted by the clinicians [103].

Photoacoustic elastography has numerous applications in the field of biological imaging. For instance, existing studies have shown that tumor tissue is generally stiffer than normal tissue due to factors such as increased cell density, extracellular matrix deposition, and elevated interstitial fluid pressure [106, 107]. Elastography analysis on PA signals can be used to visualize the mechanical properties of tumors and surrounding tissues, which helps in the identification, characterization, and monitoring of cancers. Additionally, elastography analysis has been utilized to evaluate cardiovascular disease by detecting the stiffness of blood vessels and identifying regions of plaque accumulation [108]. The approach has also been applied to musculoskeletal imaging for identifying and monitoring diseases such as arthritis and fibrosis in our previous studies [109]. Moreover, elastography holds promise in regenerative medicine as it can be used to monitor the mechanical properties of tissue structures and assist with tissue engineering applications [103].

2.2.4 Multivariate Parameter Classification

The previous sections have discussed various features that can be extracted from PA signals or images. By considering multiple parameters simultaneously, the accuracy and robustness of the conclusions drawn can be improved. For example, Dr. Willmann's group proposed a multiparameter approach that combined oxygen saturation, total hemoglobin, and lipid content and successfully differentiated four different breast histologies *in vivo* using mice [237]. Dr.

Kim's group employed a support vector machine (SVM) to combine the spectral gradient of PA signals, relative sO2, and the skew angle in the sO2 distribution to differentiate thyroid cancers from normal tissue in a study involving 52 patients and 28 normal subjects [239]. The results showed that this multiparametric analysis had a higher accuracy compared to using a single parameter alone and classified Papillary thyroid carcinoma (PTC) nodules more accurately. Other studies have explored the use of multiparametric parameters form photoacoustic and ultrasound techniques to detect rheumatoid arthritis [240], both biomechanical features and morphology features to identify early esophageal [241] and early atherosclerotic plaque [242]. These studies demonstrate the potential of multiparametric analysis of PA signals or images for improving disease diagnosis and characterization.

Overall, PA signals combined with machine learning algorithms permit the joint analysis of diverse chromophores that may be present in the tissue, accounting for their spectral properties and spatial arrangement. The classification methods that are commonly used include support vector machine (SVM), k-nearest neighbor, neural networks, and random forests. In the study of prostate cancer, various parameters targeting hemoglobin content, such as sO2, total hemoglobin, have been studied for their potential to quantify prostate cancer [116, 117, 118, 119]. Other parameters, including collagen and lipid content, and cell morphology, such as nucleus cells, have also been used for classification of prostate cancer using PA spectrum analysis [67, 28, 29, 120, 121]. However, there are limited studies that combine all or part of these parameters to verify the robustness of classification. In the third part of this thesis, we introduced a new biomechanical parameter, PA-strain, for differentiating between different fibrosis states. Since we have already studied collagen and hemoglobin content in previous work [196, 193]. We plan to combine these parameters to evaluate the effectiveness of multivariate parameter classification. Specifically, we will use SVM to perform multivariate classification on all the parameters we have obtained in the following chapters. This approach will provide insight into the potential of using multiple parameters for accurate diagnosis and classification of tissue pathologies.

Chapter 3 Characterizing the Aggressiveness of Prostate Cancer Using an All-optical Needle Photoacoustic Sensing Probe: Feasibility Study

In this chapter, we present an innovative approach for improving the detection accuracy of aggressive prostate cancer through the implementation of an interstitial measurement method. We utilized the Photoacoustic (PA) technique, leveraging the advantages of wavelength tunability and distinct absorption properties of various tissue components. Our groundbreaking interstitial PA measurement method overcomes the limitations in traditional abdominal or transrectal guidance proposed by other groups, addressing the challenges of co-registration and penetration limitations that may hinder detection accuracy. Featuring an all-optical PA needle probe with PA spectrum analysis, our method has been successfully demonstrated on *ex vivo* tissue slices, highlighting its potential to transform prostate cancer diagnosis and treatment. For further details and a comprehensive discussion, please refer to our published paper [120].

3.1 Introduction

Tissue microarchitecture plays a critical role in the pathological diagnosis of diseases [22]. For example, the microarchitecture of prostate glands is evaluated by pathologists and assigned with Gleason scores that are the current clinical standard for evaluating the prognosis for patients with prostate cancer. The current standard procedure for assessing tissue microarchitecture is biopsy followed by histopathology which involves invasive tissue extraction [111, 112], places the patient at risk of biopsy-related complications [113], and contributes to expense and time for histological processing. Therefore, non-invasive, or minimally invasive methods for instantaneous *in vivo* assessment of tissue microarchitecture are highly desired.

Traditional diagnostic methods, such as transrectal ultrasound-guided biopsy and magnetic resonance imaging (MRI), have been the mainstay of prostate cancer diagnosis for decades [244]. However, these methods have several limitations, including poor accuracy to differentiate between benign and malignant lesions and cause low yield in tissue extraction [245]. In recent years, interstitial needle probes have emerged as a promising tool for diagnosing prostate cancer [67, 246], offering several advantages over traditional diagnostic methods. These probes can be inserted directly into the prostate gland, allowing for the collection of tissue samples for histological analysis. Furthermore, the use of interstitial needle probes enables the acquisition of real-time data, enabling clinicians to assess the tumor characteristics and obtain more accurate staging information. Compared to transrectal ultrasound-guided biopsy and transabdominal guidance, interstitial needle probes have the potential to have higher sensitivity and specificity for prostate cancer diagnosis.

Recently developed photoacoustic (PA) spectrum analysis (PASA) method, by analyzing the power spectrum of PA signal in the frequency domain, offers a new method for quantitative assessment of the microarchitecture in optically absorbing biological tissues [52, 118]. By further taking advantage of the unique optical absorption spectra of individual histochemical components in tissues, such as hemoglobin, lipid, and collagen, PASA of multi-wavelength PA measurements of a tissue can assess tissue microarchitectures formed by each histochemical component. This noninvasive method facilitates the characterization of tissue microarchitecture and histochemical properties simultaneously [29, 31, 128]. Multi-wavelength PASA has been validated in previous studies and adapted to several applications, including quantifying progressive architectural changes in prostate cancer [28, 29], identifying ovarian cancer [30], characterizing non-alcoholic fatty liver disease [31, 32], differentiating intraocular tumor types [13], determining red blood cell aggregation [35], and characterizing disease within lymph nodes [36].

As demonstrated in our previous studies, the capability of PASA in characterizing micron scale structures, e.g. morphological changes of red blood cells [129] and the clustering pattern of cancer cells [28], is highly relevant to the bandwidth of the detected PA signal. Highly sensitive detection of high frequency PA signal from deep tissue *in vivo*, however, can be challenging as the attenuation coefficient of PA signals is generally proportional to the square of the signal frequency [130].

In trade of high resolution and quantitative microarchitecture information comparable to histology, we sacrificed the 2D imaging capability using an ultrasound transducer array outside the tissue-volume-of-interest and developed a prototype interstitial needle PA sensing probe [29, 126]. This probe consists of a fiber optic diffuser with approximately 10 mm illumination length and a needle hydrophone with broad bandwidth up to 30 MHz. When inserted in a minimally invasive manner, the needle PA probe can capture the high frequency A-line PA signal within illuminated tissue volume. With sufficient temporal length and bandwidth, the microarchitecture information can be extracted with statistics-based spectral analysis.

The design of the needle PA sensing probe is aligned with the standard needle biopsy procedures but aimed at minimizing tissue extractions. The fiber optic diffuser has low manufacture cost and is disposable after single use, although the emission energy is not perfectly uniform along the fiber optic diffuser [29, 126]. The hydrophone has limited receiving aperture and its sensitivity is affected by nonuniform frequency domain attenuation. These factors, in combination, form a sensitivity distribution with low frequency spatial variation. Such low frequency spatial variation contributes to a constant low frequency component in any measurement that is not considered in PASA. The sampling volume of the needle PA sensing probe is defined by the threshold contour within which sufficient signal-to-noise ratio (SNR) can be achieved. The limitation of sampling volume can be compensated by the insertions of the needle PA probe at multiple locations within the prostate, which is not achievable with traditional 1D or 2D transducer arrays for imaging. Sampling at multiple locations is commonly performed in needle biopsy procedures. For example, prostate lesion is clinically significant only if its diameter is larger than 10 mm [127]. Therefore, with multiple insertions separated by 10 mm, a clinically significant cancerous lesion in the prostate can be identified. We validated the performance of the prototype interstitial needle PA probe in rodent prostates *in vivo* [128], and canine [126] and human prostates *ex vivo* [29].

Our previously developed needle PA sensing probe used a piezo-electric hydrophone for PA signal detection. Although this hydrophone possesses excellent detection sensitivity, it has a relatively large diameter of approximately 3 mm. In addition, the high manufacturing cost of the piezo-electric hydrophone makes the interstitial needle PA probe non-disposable and expensive to use. In this study, for the first time to the best of our knowledge, we produced an interstitial needle PA sensing probe with an all-optical design. The piezo-electric hydrophone for PA signal detection was replaced by a commercially available fiber optic hydrophone. Compared to the

piezo-electric hydrophone, the fiber optic hydrophone carries the advantage of a small footprint for miniaturization of the needle PA sensing probe. The broader signal detection bandwidth of the fiber optic hydrophone not only covers the previously observed clustered cancer cells, but also the epithelium of the glandular structure in the prostate with smaller dimensions [128]. After compensated by the frequency response of the hydrophone, the signal power spectra may demonstrate peaks contributed by each of the two components, leading to a nonmonotonic and nonlinear shape. Fitting such power spectra with linear model [52, 118] may not be sufficient for comprehensively characterizing the complicated tissue microarchitecture. Hence, we introduced a nonlinear spectral analysis method. In addition, we followed previous studies [33] and implemented an envelope statistics method for time domain analysis.

The performance of the all-optical needle PA sensing probe powered by the updated analysis methods for tissue characterization was validated first using phantoms containing optically absorbing microarchitectures with various dimensions and densities. Then, the diagnostic capability of the all-optical needle PA sensing probe was examined via the experiments on fresh human prostate tissues with different stages of progressive prostate cancer.

3.2 Experiment Setup

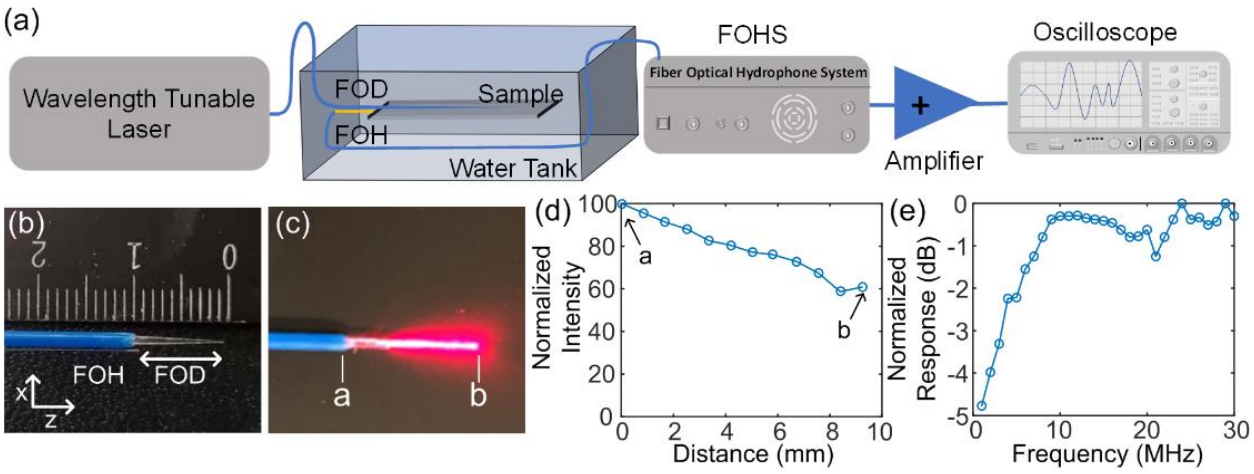


Figure 3-1: All-optical needle PA sensing probe setup. (a) System schematics. FOD: Fiber optic diffuser, FOH: Fiber optic hydrophone. FOHS: Fiber optic hydrophone system. (b) The needle PA sensing probe. (c) A photo showing the emission pattern of the fiber optic diffuser. (d) Intensity distribution along fiber diffusor needle in Figure 3-1(c). 0 mm and 10mm represent the positions a and b labeled in Figure 3-1(c), respectively. (e) Frequency response of the fiber optic hydrophone. This figure is taken from our published paper [120].

3.2.1 System Setup

As illustrated in Figure 3-1(a), the illumination sources of the experiment system inclum, 0020 fuser, the emission optical energy distribution along the fiber optic diffuser was quantified, as shown in Figure 3-1(d). The PA signals generated by the fiber optic diffuser were received by a fiber optic hydrophone (OD=150 μm, Precision Acoustics, UK) [130] positioned parallel to the fiber optic diffuser, as illustrated in Figure 3-1(b). The acquired signals were displayed on an oscilloscope and stored by a computer after amplification by 20 dB (5072 Pulse/Receiver, Olympus, Center Valley, PA). All signals were calibrated using the frequency response of the fiber optic hydrophone as shown in Figure 3-1(e).

3.2.2 Spatial Sensitivity Distribution of the All-Optical Needle PA Sensing Probe

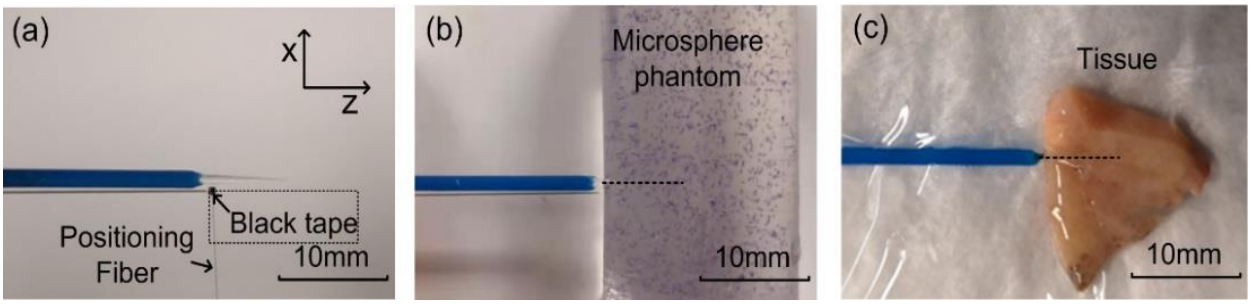


Figure 3-2: Measurement geometries. (a) Measuring spatial sensitivity distribution of the all-optical needle probe using 1 mm diameter microsphere as a point object. Driven by 2D translation stages, the point object fixed at the tip of a positioning fiber was placed at different locations in the dashed rectangle area. (b) A photo taken during a phantom study. (c) A photo taken during the study of human prostate tissue. The dashed lines in (b) and (c) are the emission segments of the fiber optic diffusers. This figure is taken from our published paper [120].

We quantified the spatially distributed sensitivity offered by the all-optical needle PA sensing probe. A black microsphere with a diameter of 1 mm (BKPMS-1.2, Cospheric LLC., Santa Barbara, California) was fixed at the tip of a positioning fiber. Driven by a 2D translational stage, the microsphere was positioned at different locations with respect to the needle probe. Both the needle probe and the point object were submerged in 1% intralipid solution, which has been frequently used for mimicking the optical properties of biological tissue [131, 132]. The microsphere was moved 13.71 mm along the longitudinal direction (z direction) and 3.05 mm along the azimuthal direction (x direction), both at a step size of 0.25 mm, as the scanning area shown by the dashed rectangle in Figure 3-2(a). At each position in the scanning area, PA signals from the microsphere were measured, and the SNR were quantified by the peak-to-peak

amplitude of the PA signal from the microsphere over the averaged amplitude of the background noise. Then the spatially distributed sensitivity was presented as the SNR as a function of the microsphere locations. The same procedure was repeated at three different laser wavelengths, including 1220 nm, 1370 nm, and 266 nm, which correlate to the strong absorption of lipid, collagen, and nucleus acid, respectively.

3.2.3 Phantom Preparation

We further investigated the capability of the all-optical needle PA sensing probe in distinguishing the dimensions and concentrations of optically absorbing microspheres by repeating our previous studies using the piezo-electric hydrophone [52]. As shown in Figure 3-2(b), cylindrical phantoms were fabricated with polyethylene microspheres (UVPMS-BV, Fisher scientific LLC., Santa Barbara, California) uniformly and randomly distributed in 10% porcine gel (G2500, Sigma-Aldrich Co. LLC., Burlington, MA). Illumination at 532 nm was used to target the dark purple color of the microspheres. We fabricated 9 phantoms, including 5 containing 100 μm diameter microspheres at different concentrations of 2, 6, 10, 12, and 20 microspheres per mm^3, and 4 containing 40, 50, 100, and 200 μm diameter microspheres at the concentration of 2 microspheres per mm^3. For each phantom, 6 measurements were taken at separate locations in the phantom, resulting in a total of 54 independent measurements.

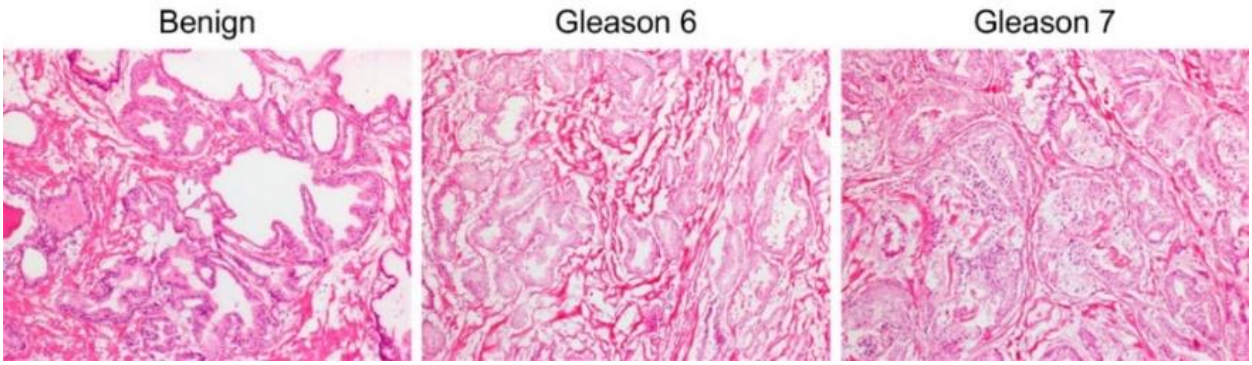


Figure 3-3: Representative histology photographs of the measured human prostate tissue samples, including a benign sample, a nonaggressive cancer tissue with GS=6, and an aggressive cancer tissue with GS=7. 100× objective magnification. This figure is taken from our published paper [120].

3.2.4 Preparation of *Ex Vivo* Human Prostate Tissues

Via the study on human prostate tissues, we examined the performance of the all-optical needle PA sensing probe in differentiating progressive cancer stages. Tissue samples with known pathological results were obtained from the Specialized Programs of Research (SPORE) tissue core at the University of Michigan. The tissue procurement protocol was approved by the institutional review board of human subject research at the University of Michigan. The sample pool included 7 benign human prostate tissue samples, 4 nonaggressive cancer human prostate tissue samples [Gleason score (GS)=6], and 3 aggressive cancer human prostate tissue samples (GS=7). The representative histology photographs of the samples are shown in Figure 3-3. As shown in Figure 3-2(c), each tissue block had the dimensions of approximately 15 mm×10 mm×3 mm. To prevent possible contamination of the tissue samples that were to be returned to the tissue bank, we inserted the fiber optic diffuser into the sample, covered the tissue sample with optimal cutting temperature compound, and sealed the sample with saran wrap. The PA measurements in each sample were acquired at 2 to 3 different locations with separations of 5 mm on average. Due to the limited spatial detection range shown later in the results section, we considered the measurements from these 2-3 different locations to be independent. The total number of measurement locations was 30, including 14 in benign tissues, 8 in nonaggressive tissues, and 8 in aggressive tissues. At each location, measurements at the three laser wavelengths, including 1220 nm, 1370 nm, and 266 nm, were taken.

3.3 Analysis Methods

The fiber optic hydrophone enables a broader detection bandwidth [130] compared to the piezoelectric needle hydrophone in our previous studies [52], which highly benefits the capability of the needle PA probe in characterizing tissue microarchitecture. As mentioned in Chapter 3.1 and shown later in Chapter 3.4, the broad bandwidth of the fiber optic hydrophone facilitates the resolution of both cancer cell clusters and the epithelium of prostate glands with smaller dimensions. The two components in combination form nonlinear spectral shapes. In this case, our previously used linear spectral analysis approach is no longer reliable. To address this issue, two nonlinear signal analysis methods were utilized in this study for quantifying the microarchitectural information encoded in PA signal. A PA signal from a phantom containing

100 μm diameter microspheres at the concentration of 20 per mm^3, as shown in Figure 3-4(a), was utilized as an example to explain the two analysis methods.

3.3.1 Nonlinear Spectrum Analysis

After a radiofrequency (RF) PA signal of a sample was acquired, as shown in Figure 3-4(a), the power density spectrum of the signal was generated, as shown in Figure 3-4(b). Instead of performing a linear fit over the entire detected power spectrum, we fitted each segment of the power spectrum covered by an expanding window to a linear model. We defined the initial segment of the power spectrum covered by the expanding window as [3, 11 MHz]. 3 MHz was selected because the frequency response of the fiber optic hydrophone falls by -3dB, i.e., 70% of the maximum frequency response, below 3 MHz as shown in Figure 3-1(e). 11 MHz was selected because most of the power spectrum in this study reached the highest magnitude at this frequency. The linear fitting of the power spectrum in this segment led to a spectral slope. Then we increased the upper limit of the expanding window with a constant step size of 2 MHz. For each segment, a linear fitting of the power spectrum was conducted, leading to a spectral slope. This process continued until the expanding window reached [3, 29 MHz], where 29 MHz was the upper limit of the calibrated spectral range of the fiber optic hydrophone. Figure 3-4(c) shows the spectral slope values calculated for each power spectrum segment as a function of the limits of the expanding window. Then, the curve in Figure 3-4(c) was fitted by a linear model, and the slope of this linear model was quantified as the nonlinear spectral slope.

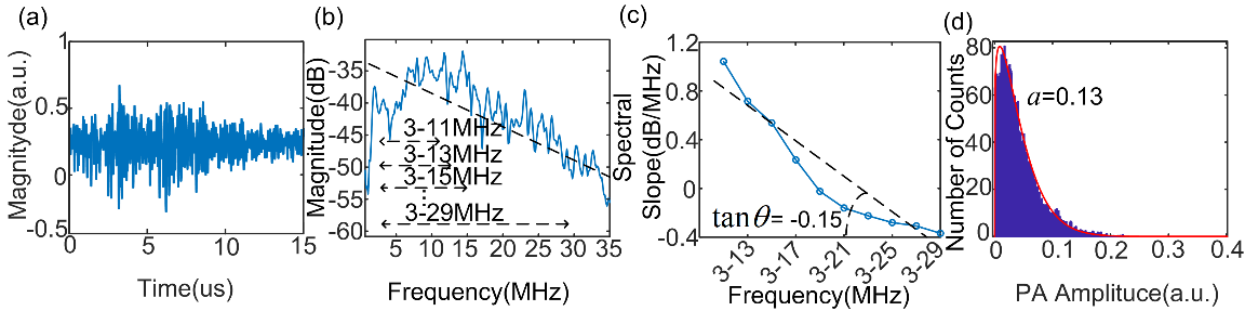


Figure 3-4: Process for quantitative PA analysis of tissue microstructure. (a) Representative PA signal measured by the all-optical needle PA sensing probe from a phantom containing 100 μm diameter microspheres at the concentration of 20 per mm^3. (b) Power density spectra of the signal in (a) and the illustration of the expanding window for calculating spectral slopes for different spectral segments. (c) Calculated spectral slope values as a function of the upper limit of the expanding window. A linear fitting of this curve leads to the nonlinear spectral slope (i.e., tan θ, where θ is the angle between the fitting liner and x-axis). (d) The histogram of the signal in (a). Red line is the fitted generalized gamma distribution. This figure is taken from our published paper [120].

Compared to linear spectral slope, nonlinear spectral slope magnifies the contribution of high frequency components in quantifying the shape of a signal power spectrum. During the quantification of linear spectral slope, the low frequency components dominate the linear fitting due to their large magnitudes. By calculating the linear slopes within segments of a signal power spectrum in Figure 3-4(b), the contribution of low frequency components is separately calculated. Any spectral peak in the high frequency range will lead to a local slow descending rate in the curve shown in Figure 3-4(c), leading to the increase of the slope, i.e., $tan\theta$, derived from the curve. Therefore, larger linear slopes derived from wide frequency windows in Figure 3-4(b) and 3-4(c) indicate more high frequency components in the signal power spectrum and lead to higher nonlinear spectral slope values.

3.3.2 Envelope Statistics

Besides the nonlinear spectral analysis in frequency domain, we also implemented envelope statistics to the PA signal in time domain, following a previous study [33]. Our study used the built-in "envelope" function in MATLAB (R2018b, Mathworks Inc., Natick, MA) to extract the positive envelopes of the signal by a Hilbert finite impulse response filter. The histogram of the signal envelopes was then generated using MATLAB, as shown in Figure 3-4(d). The signal histogram was afterwards fitted to the probability density function of the Generalized Gamma (GG) distribution:

$$f(s;a,d,p) = \frac{(p/a^d)x^{d-1}e^{-(x/a)^p}}{\Gamma(d/p)}, \quad \text{Equation 3-1}$$

where a, d and p are three positive parameters determining the shape of the distribution. The GG distribution has been used in PA signals analysis for envelope statistical studies [138, 139]. Among them, the GG parameter a dominantly determines the height and the width of the distribution that are correlated to the microarchitectural information encoded in the RF PA and US signals [33]. Thus, GG parameter a was investigated in this study.

3.3.3 Statistics and Multivariate Parameter Analysis

The correlations between the quantitative PA measurements and the microsphere dimensions and concentrations in the phantom study were calculated. To examine whether the quantitative PA measurements acquired by the all-optical needle PA sensing probe can characterize the

microarchitectures in prostate tissues, the nonlinear spectral slope, and the GG parameter *a* from different tissue categories (benign, GS=6, and GS=7) were compared in t-tests. T-tests were used because this study has limited sample size. The data sets were analyzed using the built-in function, "ttest", in MATLAB (R2018b, Mathworks Inc., Natick, MA). The null hypothesis is defined as that the nonlinear spectral slope (or the GG parameter a) cannot differentiate among the three categories of prostate tissues. The correlations between the nonlinear spectral slope and the GG parameter *a* were also calculated to understand the dependence between the two parameters.

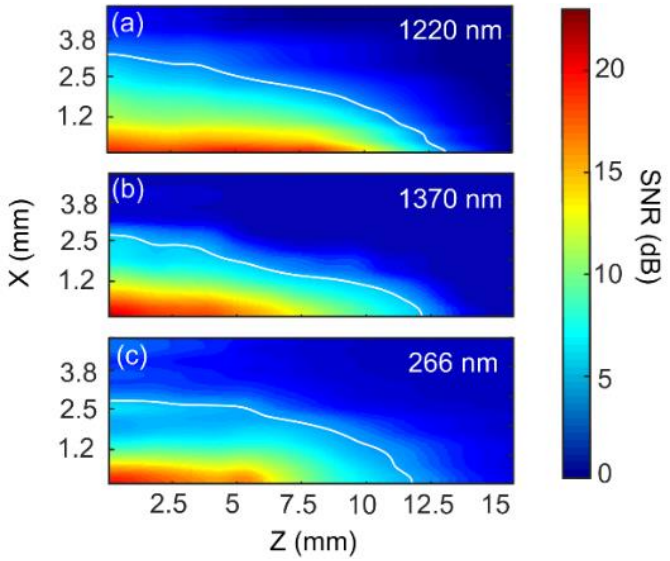


Figure 3-5: Spatial distributions of the detection SNR achieved by the all-optical needle PA sensing probe. (a), (b), and (c) are the results measured at 1220 nm, 1370 nm, and 266 nm, respectively. White line is the 5 dB boundary at each wavelength. This figure is taken from our published paper [120].

We further examined the feasibility of these quantitative PA measurements in distinguishing the prostate tissue categories via a multivariate SVM analysis. SVM was conducted using a built-in function in MATLAB ("fitcsvm" function with SVMtrain, default Gaussian kernel with 2 box-constraint for higher cost of misclassified points) between each pair of the three categories. Due to the limited sample size, we only attempted to define the boundaries among the tissue categories. The SVM boundaries were derived using the quantified PA measurements at each of the three laser wavelengths and all wavelengths. Then the accuracy of the boundaries in distinguishing the tissue categories was calculated.

3.4 Results

3.4.1 Spatial Distribution of Measurement Sensitivity

Figure 3-5 shows the spatial distribution of the SNR measured with the setup in Figure 3(a) as an indication of the spatially distributed sensitivity enabled by the all-optical needle PA probe. As shown in Figure 3-5, measurements at the three wavelengths have similar sensitivity distribution patterns. Using 5 dB SNR as the detection threshold of the needle probe, the detection range of the needle PA probe is 2.83±0.30 mm in x dimension (with the largest difference between the results at 1220 nm and 1370 nm), and 12.41±0.43 mm in z dimension (with the largest difference between the results at 1220 nm and 266 nm.

3.4.2 Phantom Study Results

Figure 3-6 shows the representative PA signals from phantoms containing optically absorbing microspheres with varied dimensions and concentrations, as well as the corresponding spectral analysis and envelope statistics. The RF PA signals in Figure 3-6(a) show that, at the same concentration, microspheres with larger dimensions generate higher PA signal amplitudes. In the power spectra in Figure 3-6(b), compared to the 100 μm microspheres, the power density spectrum of 40 μm microspheres shows less steep descent along the frequency axis, indicating relatively more high frequency components compared to low frequency components. As demonstrated in Figure 3-6(c), the quantified nonlinear spectral slope derived from the 40 μm microspheres is 0.01 which is higher than the -0.16 derived from the 100 μm microspheres. The RF PA signals in Figure 3-6(e) show that, with the same dimension, the microspheres with higher concentration also generate higher PA signal amplitudes. The corresponding power density spectra of the two phantoms are shown in Figure 3-6(f), where we can see that, despite the difference in magnitude, the overall shapes of the two spectra are similar. The difference between the quantified nonlinear spectral slopes derived from these phantoms containing microspheres with the same dimension but different concentrations (-0.08 vs. -0.19), as shown in Figure 3-6(g), is not as significant as those in Figure 3-6(e). Such a finding indicates that the nonlinear spectral slope is dominantly determined by the microsphere dimensions. The moderate difference (i.e., slightly smaller slope for the microspheres with higher concentration) can be due to the aggregation of the microsphere which leads to larger absorber dimensions and, therefore,

stronger low frequency components in PA signal. In Figure 3-6(d) and (h), microspheres with smaller dimensions and lower concentrations both had taller and narrower GG distributions, which agrees with the findings of a previous study [33]. Figure 3-7 presents the statistical analysis of the nonlinear spectral slopes and the GG parameter *a* acquired from the phantoms containing microspheres with varied dimensions and concentrations. Figure 3-7(a) and (c) are the quantified results from the phantoms containing microspheres with the same concentration (2 microspheres per mm3) but different dimensions (40, 50, 100, and 200 μm diameter); while Figure 3-7(b) and 3-7(d) are the quantified results from the phantoms containing microspheres with the same dimension (100 μm diameter) but different concentrations (2, 6, 10, 12, and 20 microspheres per mm^3). The nonlinear spectral slope shows a strong and negative correlation with the dimensions of the microspheres ($r=-0.80$, $n=20$, $p<0.0001$) but a relatively weak correlation with the concentrations of the microspheres ($r=-0.54$, $n=25$, $p<0.0001$); while the GG parameter *a* shows a strong correlation with the dimensions of microspheres ($r=0.72$, $n=20$, $p<0.0001$) and a moderate correlation with the microsphere concentrations ($r=0.63$, $n=25$, $p<0.0001$).

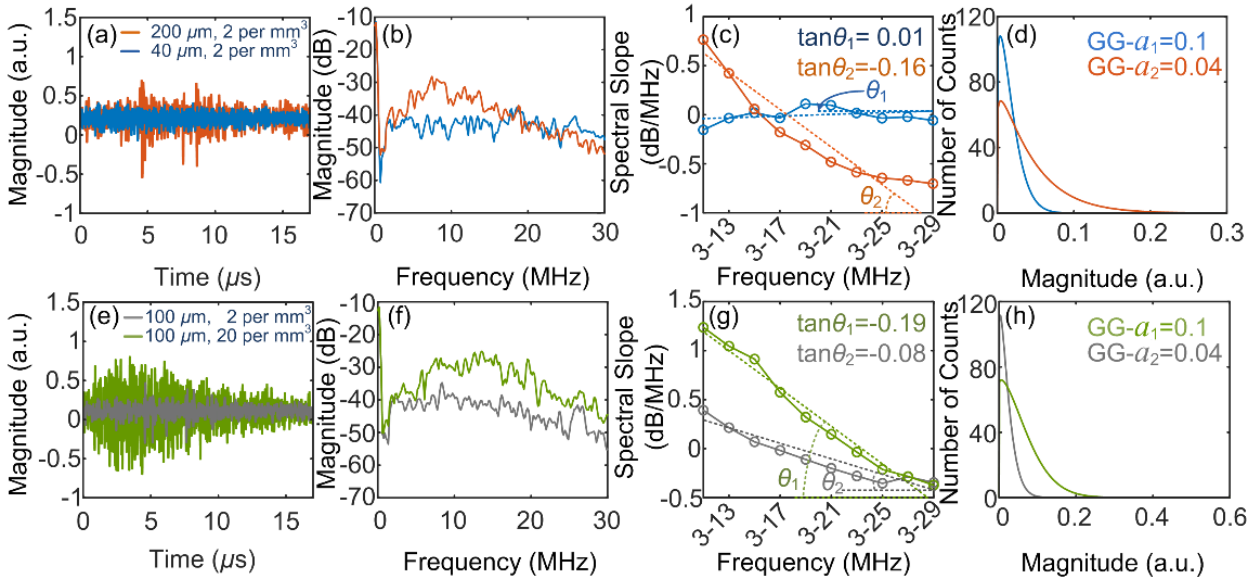


Figure 3-6: Representative RF PA signals obtained for microsphere phantoms and the quantitative processing procedures including deriving the nonlinear spectral slopes and envelope statistics. The blue and orange curves in (a-d) are from microspheres at the same concentration of 2 per mm^3, but with different dimensions of 40 μm and 200 μm, respectively. The gray and green curves in (e-h) are from microspheres with the same dimension of 10 -μm, but with different concentrations of 2 per mm^3 and 20 per mm^3, respectively. (a) and (e) RF PA signals. (b) and (f) The corresponding power spectra. (c) and (g) The derived spectral slopes using the expanding window and the quantification of the nonlinear spectral slopes. (d) and (h) The GG distributions and the corresponding parameter *a*

calculated in envelope statistics. GG-*a* stands for GG parameter *a*. This figure is taken from our published paper [120].

Combining the nonlinear slopes and GG parameter *a*, Fig. 3-7 defined the in case of different sizes phantoms with the change of microsphere size and concentrations. The accuracy as the ratio between the correctly categorized sample number over the total sample number is 92% in Figure 3-8(a) with 2 counts per mm^3 concentration but varied dimesons and 80% in Figure 3-8(b) with the same dimension (100 μm diameter) but varied concentrations.

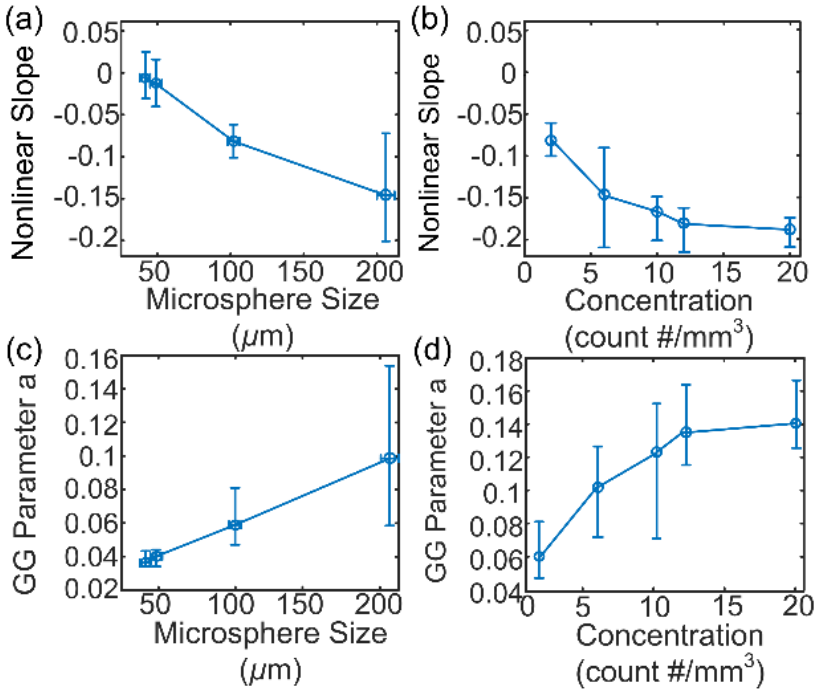


Figure 3-7: Statistical analysis of the quantitative PA measurements. (a) Nonlinear spectral slopes and (c) GG parameter a quantified from PA measurements of microspheres with the same concentrations of 2 counts per mm^3 but varied dimesons (40, 50, 100, and 200 μm diameter). (b) Nonlinear spectral slopes and (d) GG parameter *a* quantified from PA measurements of microspheres with the same dimension (100 μm diameter) but varied concentrations (2, 6, 10, 12, and 20 microspheres per mm^3). This figure is taken from our published paper [120].

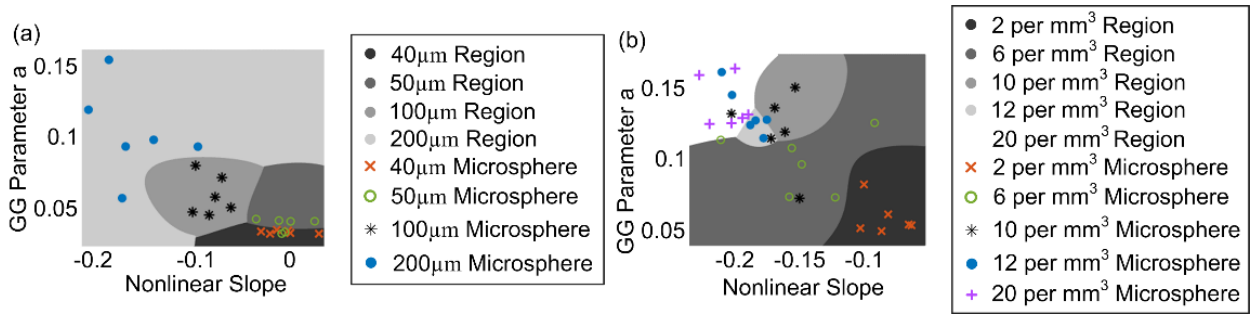


Figure 3-8: SVM based categorization of the phantom study combining the nonlinear spectral slope and GG parameter *a*, (a) The classification between microsphere phantoms with the same concentrations of 2 counts per mm^3 but varied dimesons (40, 50, 100, and 200 µm diameter). (b) The classification between microsphere phantoms with the same dimension (100 µm diameter) but varied concentrations (2, 6, 10, 12, and 20 microspheres per mm^3). This figure is taken from our published paper [120].

3.4.3 Human Tissue Results

Figure 3-9 shows the representative RF PA signals from the human prostate tissue samples at 1220 nm laser wavelength acquired by the all-optical needle PA sensing probe. The signals have an effective length of approximately 4 μs, corresponding to 60 wavelengths at the central frequency of the detection. There is no noticeable difference between the RF PA signals from the tissues in different categories (i.e. benign, GS=6, and GS=7).

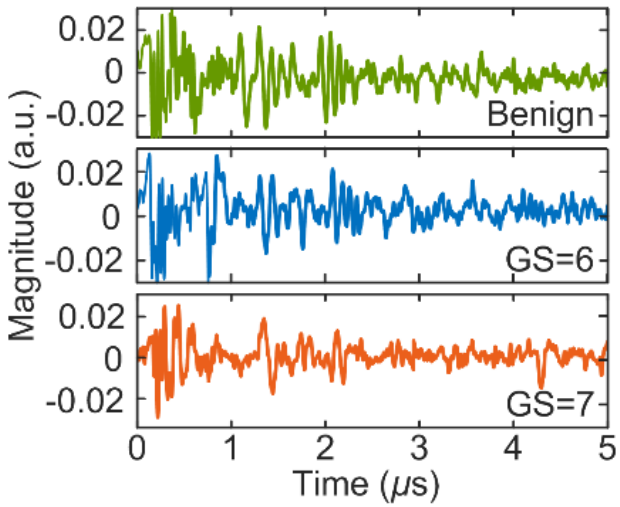


Figure 3-9: Representative RF PA signals acquired from a benign prostate tissue, a nonaggressive cancer tissue (GS=6), and an aggressive cancer tissue (GS=7), acquired at 1220 nm laser wavelength. This figure is taken from our published paper [120].

Figure 3-10 shows the procedures for analyzing the PA signals from the prostate tissues. Figure 3-10(a) demonstrates that, especially at 266 nm, the power spectra derived from the tissue

samples shows significant nonlinearity. In the 20-30 MHz range, benign tissue possesses larger high frequency components than nonaggressive cancer (GS=6) which demonstrates larger high frequency components than aggressive cancer (GS=7). In Figure 3-10(b), the curves derived from the expanding frequency window show more distinguishable trends among the tissue samples compared to the power spectra in Figure 3-10(a). The nonlinear spectral slopes are in the order of benign, GS=6 and GS=7, from the largest to smallest of all three wavelengths. This observation is supported by the histology in Figure 3-3. As prostate cancer progresses, the simple layer of epithelial cells in benign tissue or nonaggressive cancer that produces high frequency signal components may be replaced by large architecturally complex cell clusters in aggressive cancer. The large gaps between the cancer cell clusters, i.e., connective tissue rich in lipid and collagen, also tend to produce less high frequency spectral components at 1220 nm and 1370 nm compared to the benign tissue. These observations also match the findings in phantom studies, where the microspheres dimensions are negatively correlated with the nonlinear spectral slopes.

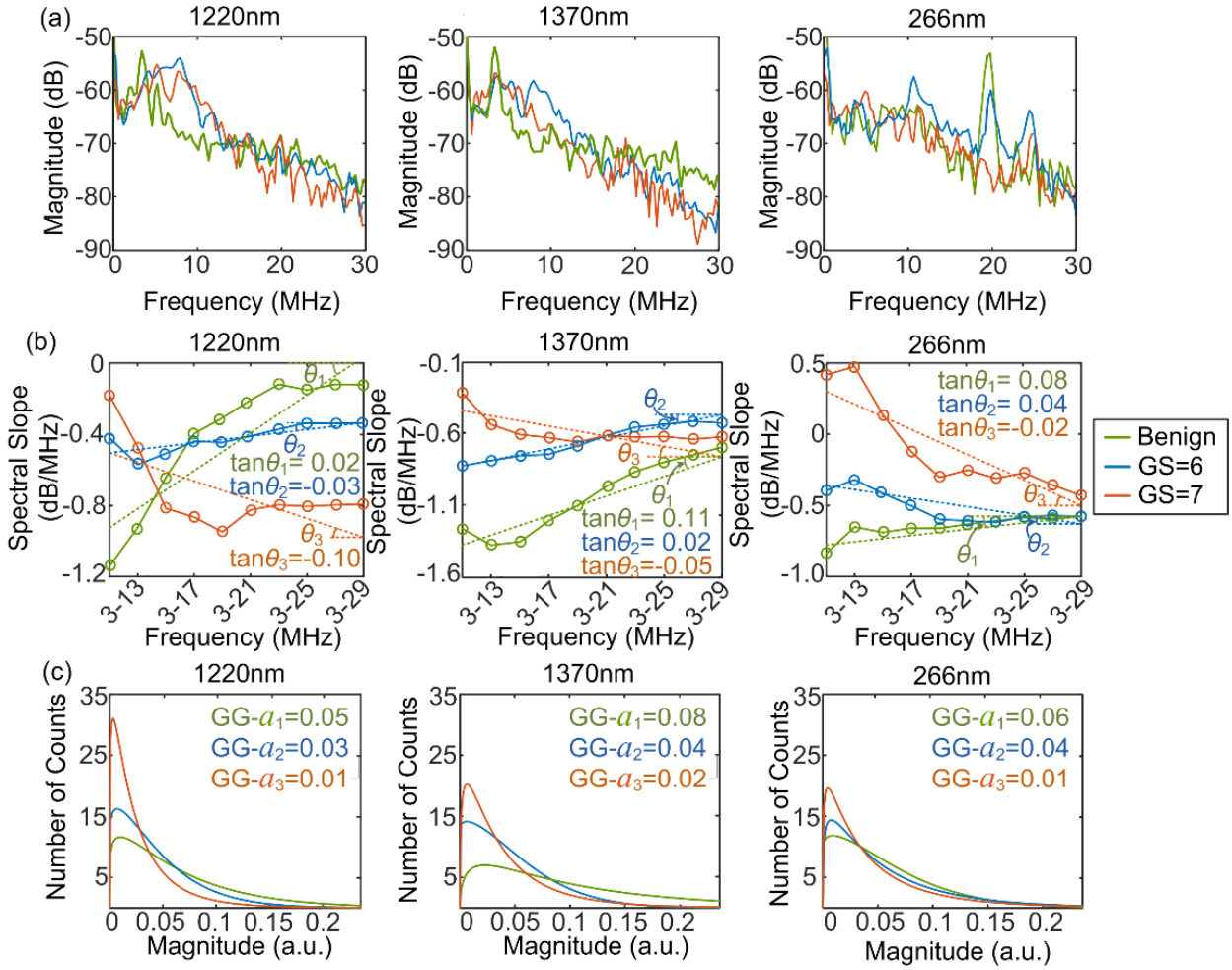


Figure 3-10: Nonlinear spectral analysis and envelope statistics of representative PA signals acquired from human prostate tissues, including benign (green curves), GS=6 (blue curves), and GS=7 (orange curves), at the three optical wavelengths (1220 nm, 1370 nm, and 266 nm). (a) Power spectra of the PA signals acquired from the three prostate tissues at the three optical wavelengths. (b) Nonlinear spectral slopes calculated from the power spectra in (a). (c) GG distributions derived from the envelope statistics of PA signals acquired from the three prostate tissues at the three optical wavelengths. GG-*a* stands for GG parameter *a*. This figure is taken from our published paper [120].

In Figure 3-10(c), GG distributions show increasingly narrow and tall profiles along with the progression of prostate cancer at all three wavelengths. The three tissue groups show more observable differences at 1220 nm and 1370 nm compared to those at 266 nm. Such results are supported by the fact that the connective tissue rich in lipid and collagen contents decreases as the cancer progresses [29, 133, 134]. The GG distribution at 266 nm in Figure 3-10(c) shows less differentiable features, which is supported by the fact that the diagnosis of aggressive prostate cancer frequently involves architecture changes instead of changes in the number of cancer cells within the tissues. The monotonically decreasing trend of quantified GG parameter a at 1220 nm and 1370 nm (targeting lipid and collagen, respectively) also matches the findings in phantom

study that the GG parameter a is positively correlated with the concentrations of the optical absorbers.

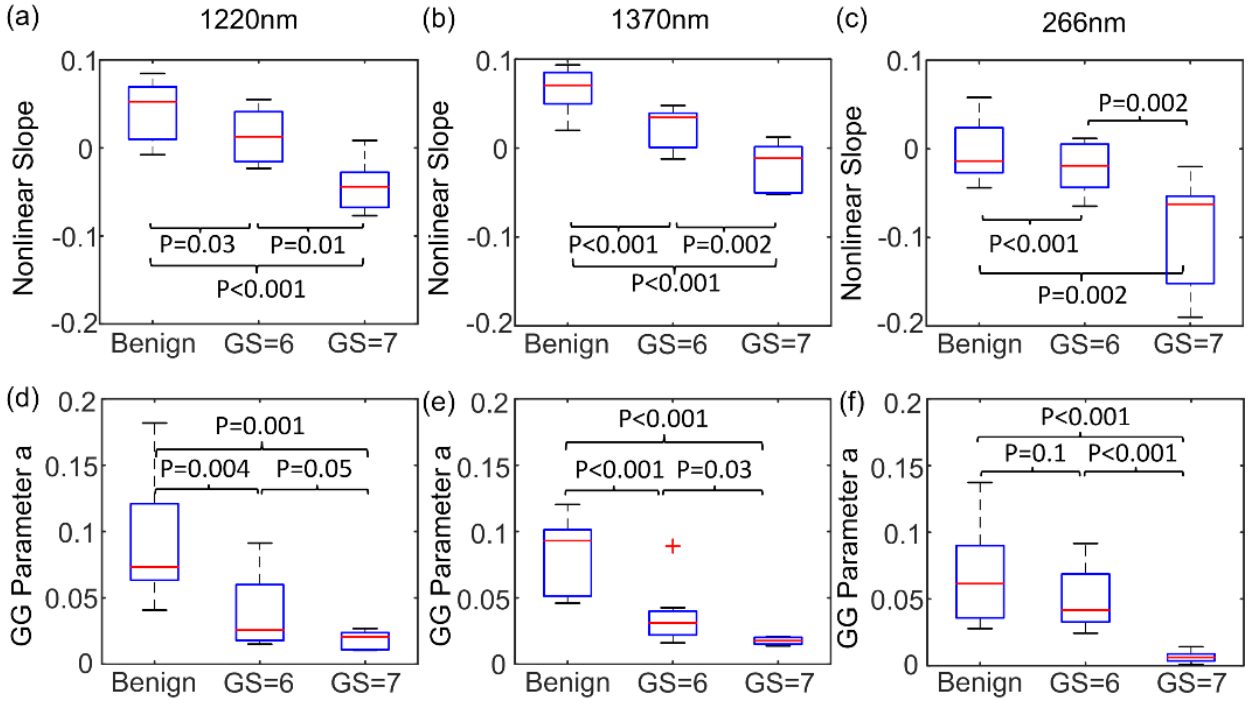


Figure 3-11: Statistical analyses of the nonlinear spectral slopes and the GG parameter *a* acquired from the three categories of human prostate tissues (benign, GS=6, and GS=7). (a-c) The box plots showing the quantified nonlinear spectral slopes of the three categories of tissues measured at the wavelength of 1220 nm, 1370 nm, and 266 nm, respectively. (d-f) The box plots showing the GG parameter *a* of the three categories of tissues measured at the wavelength of 1220 nm, 1370 nm and 266 nm, respectively. p values are quantified for the t-tests comparing the results between any two of the three categories. This figure is taken from our published paper [120].

With the nonlinear spectral analysis and envelope statistics results from all the prostate tissues, including 14 benign tissues, 8 nonaggressive cancers (GS=6), and 8 aggressive cancers (GS=7), statistical analyses were conducted, as shown in Figure 3-11. At each of the three wavelengths (i.e., 1220 nm, 1370 nm, and 266 nm), the quantified nonlinear spectral slope can differentiate between any two of the three categories (i.e., benign, GS=6, and GS=7) with statistical significance ($p<0.05$). The quantified GG parameter *a* at the 1220 nm and 1370 nm wavelengths can also differentiate between any two of the three categories with statistical significance ($p<0.05$). The quantified GG parameter *a* at the 266 nm wavelength, however, cannot differentiate between the benign and the GS=6 categories ($p>0.05$), although the GS=6 and the GS=7 categories can be differentiated ($p<0.05$). These results are clinically desirable, as over-diagnosis of GS 6 prostate cancer leads to overtreatment and morbidity [135, 136].

Table 3-1: Correlation Between Quantitative Measurements and SVM Results. The data is taken from our published paper [120].

Wavelength	1220 nm	1370 nm	266 nm
Correlation between nonlinear slope and GG parameter *a*	0.40	0.60	0.48
Accuracy of SVM classification	0.87	0.93	0.93

As shown in Table 3-1, the quantified isrelations between the nonlinear spectral slopes and the GG parameter *a* at all the wavelengths are no larger than 0.6, suggesting that the nonlinear spectral slopes and the GG parameter *a* contain independent diagnostic information. This justifies the use of multivariate analysis involving these two different quantitative PA parameters.

As shown in Figure 3-12, the SVM at any of the three optical wavelengths defined the boundaries between any two of the three tissue categories. We calculated the accuracy of the boundaries as the ratio between the correctly categorized sample number over the total sample number. Table 3-1 lists the accuracy of the boundaries defined using either of the two quantitative parameters (i.e., nonlinear slope and GG parameter *a*). When combining the quantitative parameters at all the three wavelengths, SVM demonstrated 100% accuracy in defining the boundaries among the three tissue categories.

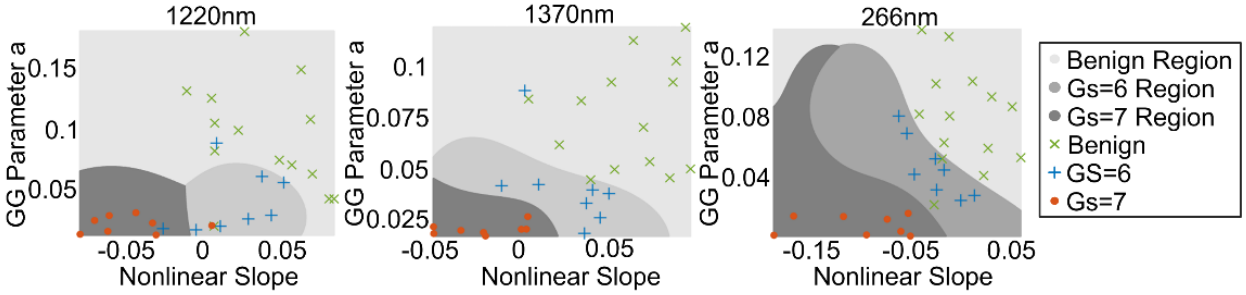


Figure 3-12: SVM based categorization of the human prostate tissues, including benign, GS=6, and GS=7, by combining the nonlinear spectral slope and GG parameter *a* quantified at each of the optical wavelengths (1220 nm, 1370 nm, and 266 nm). This figure is taken from our published paper [120].

3.5 Discussion and Conclusion

This study, for the first time, validated the feasibility of an all-optical needle PA sensing probe for interstitial measurements and characterization of biological tissues. With the updated signal analysis methods, quantitative PA measurements from this all-optical needle PA sensing probe demonstrated the capability in quantifying the dimensions and concentrations of the optical absorbers in phantoms, and in differentiating among *ex vivo* human prostate tissues with different stages of progressive cancer.

The main purpose of the phantom study is to examine the performance of the measurement setup with well controlled conditions. Therefore, the experiments were restricted to microspheres with uniform dimensions and distributions. The nonlinear slope and the GG parameters of 200-μm microspheres in Figure 3-7 shows larger error bar, probably due to the aggregation of the microspheres. Thus, we did not use larger microspheres. The overlapping between GG parameters of the microsphere at varied concentrations may indicate that the concentration difference investigated in this study is close to the sensitivity limit of magnitude-based envelope statistics.

The nonlinear spectral slope uses an expanding window to observe both 1) the low frequency components separately from the high frequency ones, and 2) the relative magnitude of low and high frequency components. Therefore, the expanding window bandwidth and step size have to fit to the specific microarchitectural dimensions in the targeted samples. Such approach assisted in comprehensively quantifying shape of a PA signal power spectrum that encodes tissue microarchitecture at multiple scales. The envelope statistics has shown the ability to quantify additional tissue component information (i.e., changes in lipid and collagen contents). Most parameters at the studied wavelengths can differentiate cancerous tissues from benign tissues and differentiate aggressive cancerous tissues (GS=7) from nonaggressive ones (GS=6). These parameters may be able to differentiate between clinically significant prostate cancer and benign tissue or clinically insignificant prostate cancer.

Considering that the nonlinear spectral slope and the GG parameter a contain independent diagnostic information, multivariate analysis combines the diagnostic information from these two parameters and takes full advantage of the all-optical PA measurement approach to improve diagnostic accuracy. As shown in this study, measurable SVM boundaries were identified

between the phantoms and the three types of tissues. Future study with more tissue samples will validate these boundaries [29] and investigate the mapping of these quantitative parameters to individual Gleason grades.

The all-optical needle PA sensing probe presented in this study has demonstrated the effectiveness in acquiring PA signals with sufficient temporal length for statistical analysis in both frequency domain and time domain. In this study, the optical density at the surface of the fiber optic diffuser at 1220 nm and 1370 nm is much lower than the safety limit established by American National Standard Institute (ANSI). At 266 nm, the optical density at the surface of the fiber optic diffuser was higher than the ANSI safety limit. This, however, is not a concern for the current study on *ex vivo* tissue samples.

The sensitivity profiles of the needle PA sensing probe in Figure 3-5 were determined by both the optical transmission and the acoustic reception. The profiles were measured in an ideal situation where a small interpolation occurred in a homogeneous background. The profiles may be slightly deformed by the heterogeneous optical properties in tissue. The sensitivity profiles were measured only in the plane containing both the transmission and reception components, and on the side where the fiber optic hydrophone is located. Owing to the uniform optical transmission in the azimuthal dimension of the fiber optic diffuser, the sensitivity profiles in other planes are similar except on the opposing side of the fiber optic diffuser to the hydrophone, where the aperture of the hydrophone is blocked. We assume the worst case that half of the reception angle of the fiber optic hydrophone is blocked. Therefore, we estimated sampling volume of the needle PA probe by approximating the SNR distributions in Figure 3-5 as triangles and rotating the triangle along the z axis by 180 degrees. The sampling volume covered by the needle PA probe is 45 mm^3 ($=\pi r^2 h/3/2=\pi\times 2.60^2\times 12.78/3/2$). On the other hand, considering that the sampling cavity of an 18 Gauge biopsy needle has the shape of a half cylinder with diameter of 0.838 mm and height of half an inch, the sampling volume of a biopsy core is only approximately 3.5 mm^3 ($=\pi r2h/2= \pi\times 0.4192\times 12.7/2$). Therefore, the needle PA probe has the potential to significantly increase the sampling volume for prostate cancer diagnosis. When the sampling volume covers both benign and cancerous tissue, the quantitative parameters may be averaged between the two categories. However, the detectable volume of the needle PA probe is much smaller than a clinically significant prostate tumor (10 mm in diameter). Therefore, with

multiple insertions of the needle probe the proposed 5 mm separation should be able to sample within the tumor volume where only cancerous tissue exists.

To prepare the all-optical needle PA sensing probe for clinical translation in the future, we will integrate the fiber optic diffuser and the fiber optic hydrophone into a steel needle with side window. The internal surface of the needle will be polished or coated for good light reflectance, which will increase the optical energy delivery, help reduce the optical energy at 266 nm below ANSI safety limit and extend the spatial sensitivity deeper into the tissue. The exposed optical components will be protected by a layer of medical grade polyurethane, which is acoustically matched with biological tissue and with negligible optical attenuation. We will also investigate on improving the sensitivity of the fiber optic hydrophone using established methods [144] to reduce the optical density at 266 nm while maintaining the SNR profiles achieved in Figure 3-5. Optical wavelengths between 750 to 850 nm targeting hemoglobin content will be included for measurements *in vivo*. In addition, we will search for an optimal design for light illumination by adjusting the diameter and the emission length of the fiber optic diffuser. A larger fiber diameter allows for more optical energy coupling, but the diameter is restricted by the inner diameter of the steel needle. Extended emission length facilitates more reliable statistics-based signal analysis; however, the corresponding increase in emission surface area will reduce the deliverable optical density as well as the SNR. All these optimization processes will be implemented in the next step of this research.

Chapter 4 Assessment of Prostate Cancer Using a Translational Needle Photoacoustic Sensing Probe: Preliminary Study on Intact Human Prostates

Building on the success of Chapter 3, where we effectively demonstrated an interstitial all-optical probe for quantifying aggressive and non-aggressive prostate cancer in tissue slices using PA methods, we continue to refine the technology in Chapter 4. Here, we further miniaturize the interstitial PA probe to fit within an 18G needle, making it compatible with clinical biopsy procedures. We have successfully illustrated the probe's utility and feasibility in differentiating cancer and normal regions based on biopsy simulations using intact human prostates *ex vivo*. Detailed information and results can be found in the corresponding published paper [67].

4.1 Introduction

The standard diagnosis approach of prostate cancer (PCa) is needle-based core biopsy guided by transrectal ultrasound (TRUS). Histopathologic processing of the extracted tissue visualizes the microscopic architecture of the tissue, which reflects the aggressiveness of the PCa [110]. TRUS guided prostate biopsy has a poor core yield and a high false negative rate owing to TRUS's limited sensitivity to PCa and the small volume of the biopsy core [114]. Magnetic resonance imaging (MRI) TRUS fusion biopsy has recently been introduced as a method to improve the identification of the clinically significant PCa in patients with initial negative biopsies [115, 116, 117]. Nonetheless, the procedure requires the fusion of MRI and Ultrasound (US) imaging that is subject to registration and targeting error.

Photoacoustic (PA) imaging and sensing, taking advantage of the unique optical absorption profiles of tissue components, is able to acquire microscopic tissue architecture at US resolution

[26]. Our previous studies validated that the frequency domain analysis of the photoacoustic signal power distribution, namely PA spectral analysis (PASA), can statistically quantify the content and microarchitectural distribution of tissue components inside the tissue-volume-of-interest [119]. Recent studies using human and animal prostates, including those by our [121, 120] and other groups [122, 123] have demonstrated that PASA can differentiate between benign and cancerous prostate tissues, and assess the aggressiveness of PCa. Therefore, PASA technology holds the promise to provide a diagnosis of PCa *in situ* without the need for tissue extraction, and may reduce the amount of biopsy core extractions and post-core-biopsy complications [154].

Encoding fine microarchitecture information comparable to histology, high frequency PA signal components attenuate fast through the biological tissue [125]. Aimed at capturing these high frequency signal components, we recently developed an interstitial PA measurement approach [120]. The interstitial measurement instrumentation includes a fiber optic diffuser for illumination and a needle hydrophone for signal detection. When joined together, the two components possess a slim profile for insertion into the prostate and allow for broadband PA signal acquisition from the surrounding tissue. The approach has been validated in detecting the progressive PCa in prostate tissue blocks in Chapter 3 and reference [120] and intact prostates from human subjects *ex vivo* [120] and animals *in vivo* [121]. Chapter 3 further miniaturized the interstitial needle PA sensing probe with an all-optical design that consists of a fiber optic diffuser and a fiber optic hydrophone [120].

In this study, we integrated the all-optical components into the inner lumen of a steel needle with the dimension close to a core-biopsy needle with the purpose of clinical translation. The mechanical reliability of the needles was examined by a certified medical device testing company (DDL, Inc., Eden Prairie, MN). The performance of the translatable needle PA sensing probe was examined in a simulated TRUS guided transperineal biopsy procedure using intact human prostates procured through radical prostatectomies. When inserted into the prostate, the needle PA sensing probe collected PA signals at multiple wavelengths targeting a series of tissue components. The measurement locations were stained by dye injection so that the histopathology results from the same locations can be compared to the PASA quantifications.

4.2 Experiment Setup

4.2.1 Probe Design

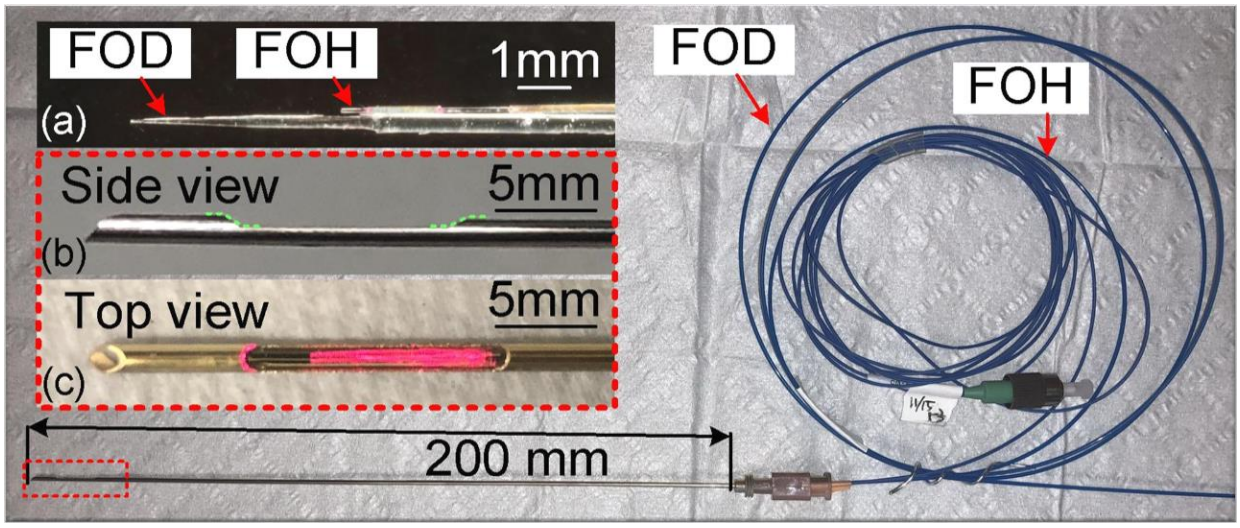


Figure 4-1: The needle PA sensing probe. (a) Optical components. FOD: Fiber optic diffuser. FOH: Fiber optic hydrophone. (b) Side view and (c) Top view of the needle probe in the red-dashed box in (a). The green dashed line marks the introducing angles. 700 nm laser was coupling into the illumination fiber in (c). The figure is taken from our published paper [67].

The needle PA sensing probe, as shown in Figure 4-1, included an 800 μm-diameter fiber diffuser for light illumination, a 150 μm-diameter fiber optic hydrophone for US detection, and a 200 mm-long 18G medical needle (TruGuide, Bard Peripheral Vascular Inc, Tempe, AZ). The emission segment of the fiber optic diffuser has a length of 6 mm and a conical shape, as shown in Figure 4-1(a). The fiber optic diffuser was fabricated following a fully automated protocol [129]. In brief, the plastic jacket of an 800 μm-diameter optic fiber was removed within 10 mm from its emission end. The emission end was positioned in a 50 mL centrifuge tube without touching the tube wall. Hydrofluoric acid ≤ 48% (HF, Sigma-Aldrich, Cleveland, OH) was infused into the tube at a flow rate of 8 μL/min. The HF acid surface gradually rose over the fiber emission end and etched a 10 mm-long conical surface. The fiber optic hydrophone with a plano-concave microresonator at the detection end [130] was driven by a commercial fiber optic hydrophone data acquisition system (Precision Acoustics, UK) in Figure 4-3(a). The functional segments of both the fiber optic diffuser and the fiber optic hydrophone were exposed through a 12 mm-long side-view window at the end of the 18G medical needle, as shown in Figure 4-1.

The 12 mm length was chosen because the prostate biopsy core is 12 mm in length. The window cutout possessed introducing angles, as shown in Figure 4-1(b), to prevent resistance during needle insertion and withdrawal. The inner surface of the side-view window was coated with gold for optimal illumination efficiency, as shown in Figure 4-1(c).

4.2.2 The Controlling System

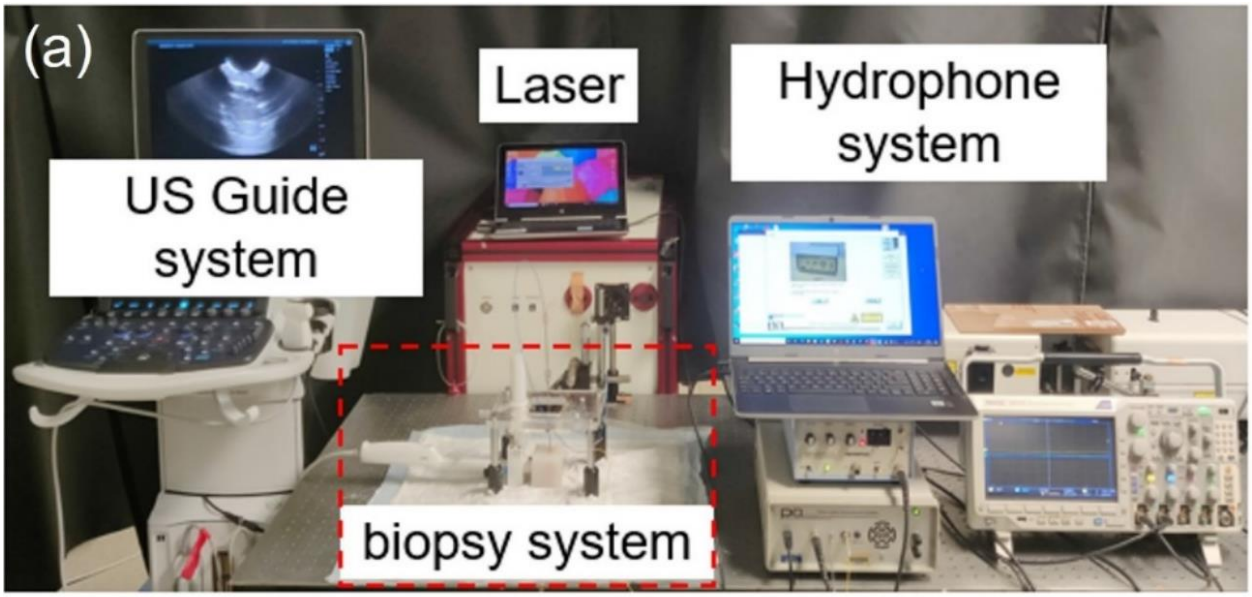


Figure 4-2: The overview of the setup includes US guide system, laser system, hydrophone system and biopsy system. The figure is taken from our published paper [67].

The needle PA sensing probe is driven by a system comprising four components: a laser system, a hydrophone system, a US guide system, and a biopsy system that simulates *in vivo* biopsy procedures. Figure 4-2 displays the diagram of the whole system. Figure 4-3 shows the main instruments in the hydrophone system and the diagram of the laser system.

In figure 4-3(b), the outputs of an optical parametric oscillator (OPO) pumped by the second harmonic of an Nd:YAG laser (Phocus Mobile, OPOTEK, Carlsbad, CA 690-950 nm and 1200-2400 nm, 5-7 ns pulse width, 10 Hz repetition rate) with pulse-to-pulse switching function and an Nd:YAG laser (using the fourth harmonic output, 266 nm, 5-8 ns pulse width, 10 Hz repetition rate, Surelite, Continuum, San Jose, CA) were integrated into the same light path and coupled into the fiber optic diffuser. In tissue studies, we employed illumination at 1220 nm, 1370 nm, 800 nm, and 266 nm to target lipids, collagen, total hemoglobin, and cell nuclei,

respectively. 266 nm illumination targets the contrast of cell nuclei [216, 217]. Since the tissue architecture described in the Gleason scoring system of PCa is formed by cancer cells, PASA at 266 nm is a direct measurement of the tissue architectures.

In this setup, the optical energy at the surface of the side-view window of the needle PA sensing probe was 3.3 mJ at 1220 nm, 1370 nm, 800 nm, and 0.9 mJ at 266 nm. According to Chapter 3, the sampling volumes for each wavelength were carefully compensated by the emission energy at each wavelength. We estimated the illumination surface as half of the cylindrical surface of the needle, which was $OD \times \pi \times h/2 = 1.27 \times \pi \times 12/2$ mm^2=23.9 mm^2. Hence, the optical energy density was approximately 13.8 mJ/cm^2 at 1220 nm, 1370 nm, and 800 nm, and 3.8 mJ/cm^2 at 266 nm. These energy levels are lower than the safety limits of 100 mJ/cm^2 at wavelengths larger than 1000 nm, 31.7 mJ/cm^2 for 800 nm, and 4.9 mJ/cm^2 for 266 nm, as established by American National Standard Institute (ANSI). The PA signals captured by the fiber optic hydrophone were amplified by 20 dB (5072 Pulse/Receiver, 1k-35MHz, Olympus, Center Valley, PA) and averaged 56 times, then displayed on an oscilloscope and stored in a computer. The needle PA sensing probe was removed after the measurements.

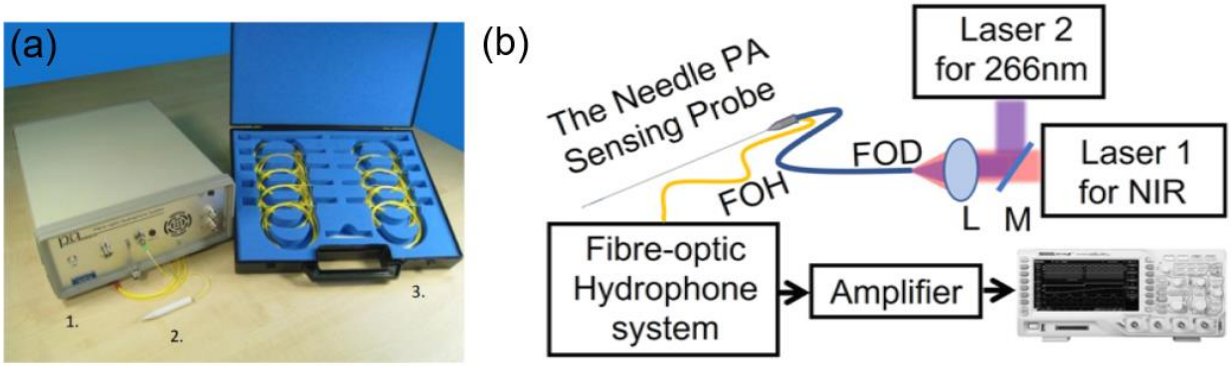


Figure 4-3: The diagram of the laser and hydrophone system. (a) Hydrophone system. The hydrophone system involves a compacted detection system (labeled as 1.) and a connected FOH (labeled as 2.). The labeled objective 3. shows the disposable FOHs in a box. (b) The Laser controlling diagram of the transperineal needle PA sensing probe system. L: Convex Len. M: Mirror. FOH: Fiber optic hydrophone. FOD: Fiber optic diffuser. NIR: Near-infrared. The figure (b) is taken from our published paper [67].

4.2.3 Simulated TRUS Guided Transperineal Needle PA Sensing Probe Insertion Procedure

This study simulated a TRUS guided transperineal biopsy procedure [158] using intact human prostates *ex vivo*. The protocol for procuring the prostate after prostatectomy procedures and

using the prostates in our experiments was approved by the Institutional Review Board of the University of Michigan Medical School. All subjects provided written informed consents. Figure 4-4 depicts the experiment setup, and the procedures are explained below.

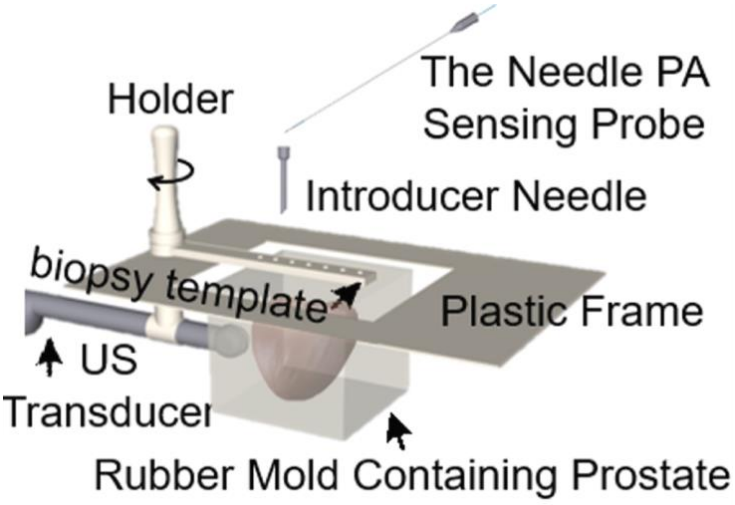


Figure 4-4: Detailed illustration of the experiment components in the red dashed box in Figure 3(a). The figure is taken from our published paper [67].

In the simulated system in Figure 4-4, the 2D imaging plane of an endocavity US array (E9-4, Zonare, Mountain View, CA) was aligned with a biopsy template with evenly distributed sampling holes for the needle PA sensing probe. Before the experiment, the sampling track in US imaging corresponding to each sampling hole were determined, as illustrated in Figure 4-5. A silicone rubber mold (Ecoflex 00-30, Smooth-On Inc., Macungie, PA) imitating the skin and subcutaneous tissue in the perineal region was used to seal the human prostate. The rubber mold containing the prostate was secured underneath the positioning system. The US array was coupled to the surface of the rubber mold with US gel. By rotating the holder attached to the US array, the US field-of-view can cover the whole prostate volume. Most of the prostatectomy patients went through preprocedural MRI. The MRI reports provided the approximate locations of the benign and cancerous regions. Along with the prostate contour shown in the TRUS imaging, we can have samplings targeting either the benign or the cancerous region. Once a needle insertion location was determined through US imaging, an 14G introducer needle (PrecisionPoint, Perineologic, Cumberland, MD) used in regular biopsy procedure were inserted through the sampling template into the rubber mold and made a pathway for the needle PA sensing probe. The needle PA sensing probe was then inserted to the desired location inside the

prostate guided by the needle position presented in the real-time US imaging, as illustrated by Figure 4-5. During the operations, TRUS was only to identify the contour of the prostate and monitor the position of PA sensing probe during insertion.

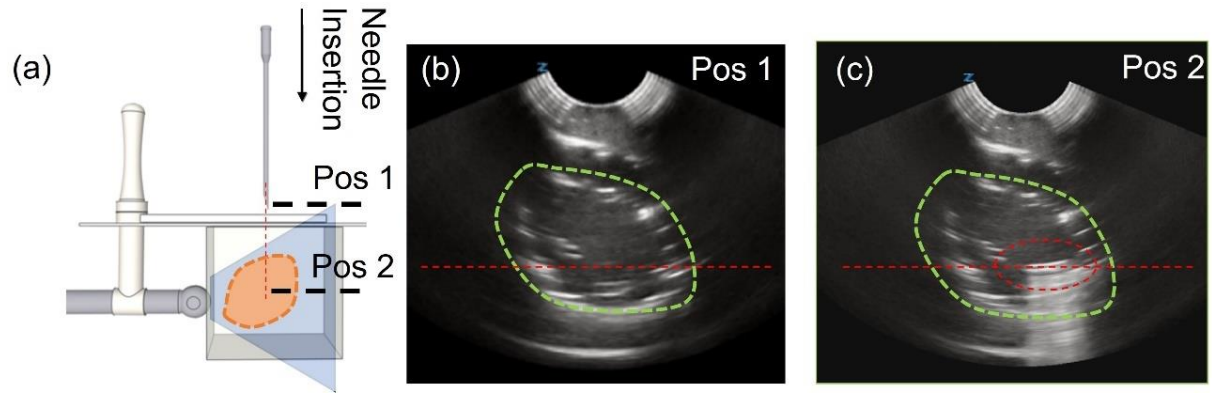


Figure 4-5: TRUS guided insertion of the needle PA sensing probe. (a) The schematic of the US guide system for needle inserting procedures. The US images (b) and (c) were taken before and after the needle insertion, respectively. The needle was marked in the red circle in (c). The red dotted line in (a-c) represents the inserting direction. The figure is taken from our published paper [67].

The needle sensing probe track in the prostate was revisited with a syringe containing a 22G needle under the guidance of US imaging. A depth stop was used to ensure that the tip of the needle was positioned at the distal end of the measured range. 0.05 mL Evans blue dye (E2129, Sigma-Aldrich, St. Louis, MO) was injected. During the needle withdrawal, the dye filled the needle track and stained the whole needle insertion track. For each prostate, 3-5 locations were examined.

4.3 Analysis Method

4.3.1 Histopathology

After the PA measurements, the intact prostates went through routine histological processing. Each prostate was dissected into 7 to 9 slices along the apex-base orientation. The malignant regions in each slice were identified and marked in the gross photo, as shown in Figure 4-6(a). The needle insertions were intentionally oriented perpendicular to the sliced planes. The stained spots in Figure 4-6(a) are the locations where needle track intersected with the sliced planes. Considering that the thickness of the slices is around 4-5 mm and the window exposing the optical components are 12 mm long, the histological gradings within the last three slices before

the staining disappeared were utilized to compare to the interstitial PA measurements. To accurately differentiate the measurements acquired in the cancerous and benign regions, only the signals acquired more than 2 mm away from the cancer boundaries were included in the statistical analysis. Table 4-1 summarizes the diagnoses of all the samples included in the statistical analysis.

Table 4-1: Disease conditions of the sampled locations. The table is taken from our published paper [67].

Groups	Sample Number @ 1220nm, 1370nm, 800nm	Sample Number @ 266nm
Benign	28	22
Cancer	21	15

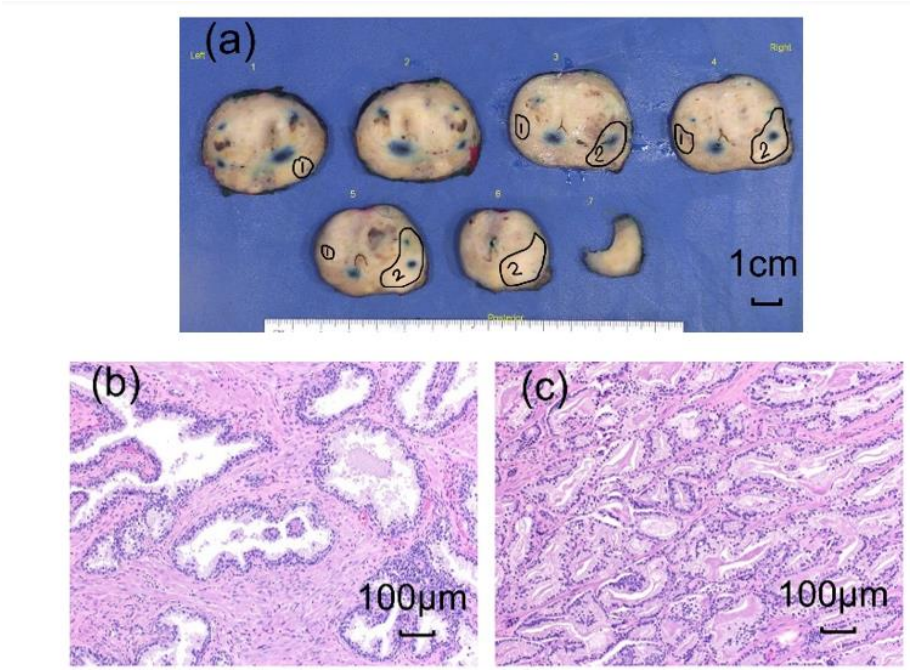


Figure 4-6: Histopathology of the intact prostates. (a) Gross pathology of the prostate by slicing the prostate into 4-5 mm thick samples. The blue spots are the spatial markers of the PA measurements by dye injection. The 2D contours of the cancerous regions were delineated in black. (b-c) represent the histology photos of the benign and the cancerous regions. 10× objective magnification. The figure is taken from our published paper [67].

4.3.2 Quantification Methods

4.3.2.1 PASA

Figure 4-7 shows the representative PA signals acquired at 1220 nm, 1370 nm, 800 nm and 266 nm in a benign and a cancerous region, respectively. The analyzed signal lengths were approximately 8 μs in time and 12 mm in distance (with speed of sound at 1540 m/s), which corresponds to the dimension of the side-view window in the needle probe. The signal power spectra were calculated and calibrated by the frequency domain response of the fiber optic hydrophone in Figure 4-7(a). Figure 4-7(b) shows a representative PA signal power spectrum after calibration.

As shown in Figure 4-7(a), the highest frequency response of the fiber optic hydrophone occurs at 8 MHz and the magnitude of the response drops by 6 dB, i.e., 50%, at 28 MHz. The representative signal power spectrum shows an approximately monotonic descending trend in the 8-28 MHz range. We quantified the magnitude and the frequency component distribution in the spectra using the slope and midbandfit of the linear fit to the spectra in the range of 8-28 MHz. As previously discovered [118, 94], a larger spectral linear slope indicates larger high frequency components compared to low frequency ones and vice versa. A larger midbandfit indicates higher content of the corresponding tissue component.

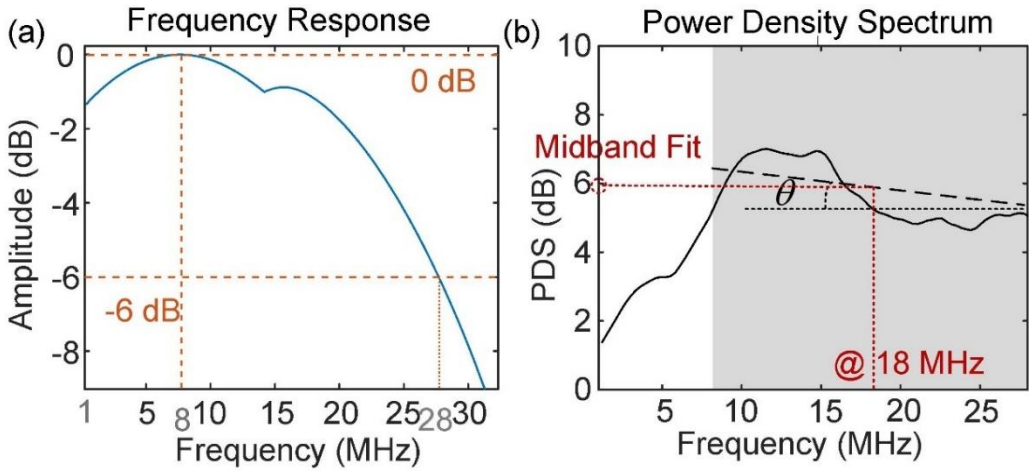


Figure 4-7: Method of PASA. (a) The frequency response of the fiber optic hydrophone system. (b) Representative calibrated PA signal power spectrum and PASA analysis. θ represents the linear slope of the PDS in the frequency range from 8 to 28 MHz. The figure is taken from our published paper [67].

4.3.2.2 Statistics and Multivariate Analysis

Due to the limited sample size, this study focused on differentiating the benign and cancerous regions using the PASA quantifications. T-tests were performed using the built-in function, "ttest", in MATLAB (R2018b, Mathworks Inc., Natick, MA). The null hypothesis is that the PASA of the measurements acquired by the translational needle PA sensing probe cannot distinguish between the benign and the cancerous regions in intact human prostates.

Following the t-tests, the multivariate support vector machine (SVM) was used to differentiate the PASA quantifications acquired from the benign and the cancerous regions using the PA measurements at 1220 nm, 1370 nm, and 800 nm. The measurements at 266nm were excluded because part of the samples do not have measurements at this wavelength. Fitcsvm, a built-in SVM function in MATLAB, was used with a Gaussian kernel and a box constraint value of 5 to achieve low overfitting while accounting for the high cost of penalty. A 5-fold cross-validation method used in our previous study was implemented, where 80% of the samples was used as training set in turns and the remaining 20% was used for testing. The testing accuracy was calculated as the average of all 5 testing cycles.

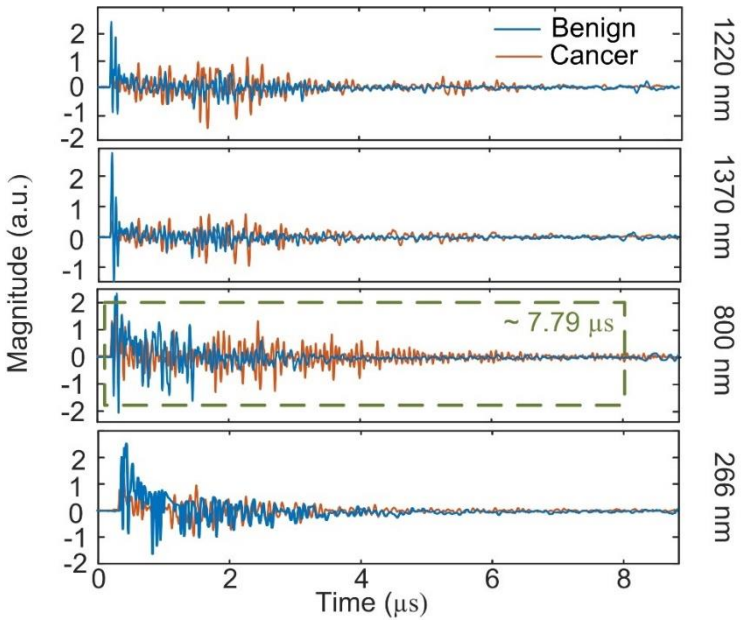


Figure 4-8: Example PA signals acquired at 1220 nm, 1370 nm, 800 nm and 266 nm wavelengths for insertions in the benign and cancer regions in an intact human prostate. The orange curves are the measurements in the cancerous region and the blue curves are the measurements in the benign region. The figure is taken from our published paper [67].

4.4 Results

4.4.1 PASA at Individual Wavelength

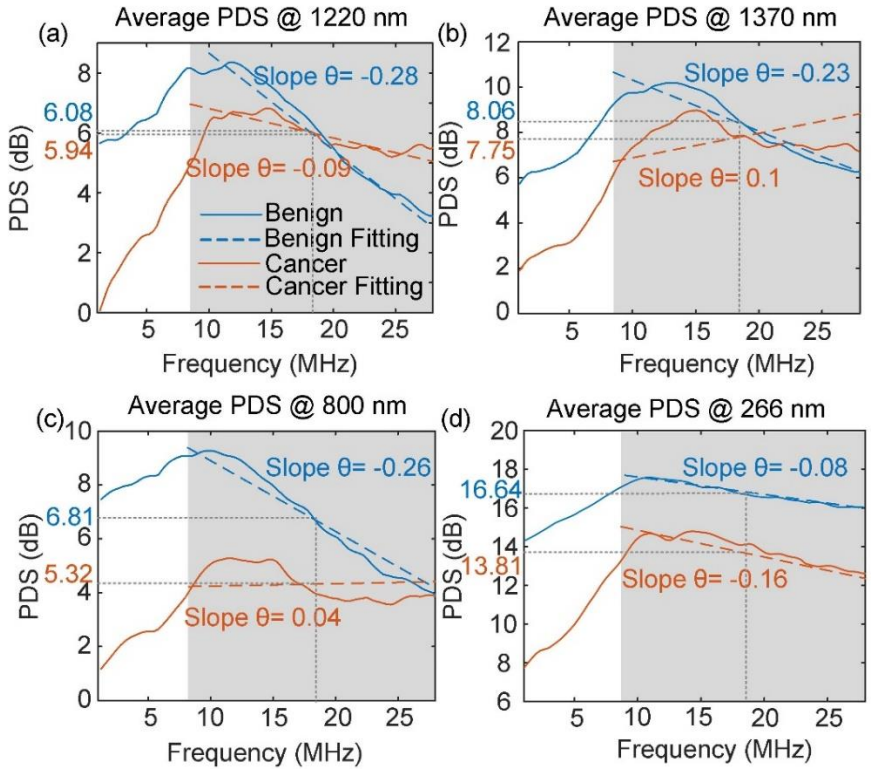


Figure 4-9: Averaged PA signal power spectra acquired within the benign and cancerous regions at (a) 1220 nm, (b) 1370 nm, (c) 800 nm and (d) 266 nm and the corresponding linear fits. The blue curves and the orange curves are the average of all measurements within the benign and cancerous regions, respectively. The dashed lines in all images were located at 18MHz. The figure is taken from our published paper [67].

Figure 4-8 shows the averaged PA signal power spectra and the linear fits for all the benign and the cancerous insertions at the wavelengths of 1220 nm, 1370 nm, 800 nm and 266 nm, respectively. Since the fiber optic hydrophone is less sensitivity to low frequency components [144] compared to piezoelectric hydrophone, the PA signal spectra in this study contain less low frequency components compared to our previous study [144, 120].

In Figure 4-9, at approximately 18 MHz, the signal power spectra of the cancerous group at both 1220 nm and 1370 nm, targeting lipid and collagen contents in the prostate, respectively, intersect with that of the benign group. Larger high-frequency signal components in the cancerous group lead to the larger spectral slopes compared to the benign region, indicating the reduced dimensions of the microarchitectures formed by lipid and collagen. Furthermore, the

midbandfits of the cancerous group are slightly lower than those of the benign group, although no significance is shown. The low midbandfit values reflect the decrease of lipid and collagen contents in the cancerous regions. Considering that the connective tissue in the prostate is rich in lipid and collagen contents, these observations are consistent with previous studies where the connective tissues [98] and collagen [99] contents are lower in cancerous prostates.

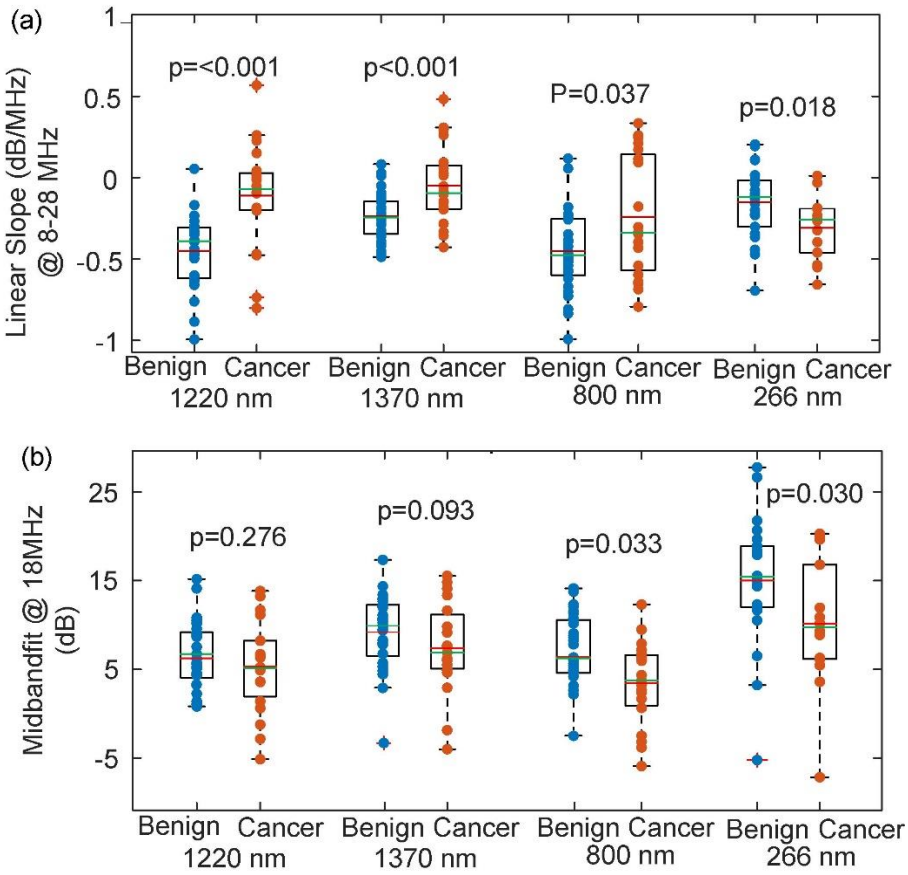


Figure 4-10: Statistics of the PASA quantifications, including (a) The linear slope and (b) The midbandfit for the spectral range of 8-28 MHz, for the benign and the cancerous regions at 1220 nm, 1370 nm, 800 nm, and 266 nm. The green line and the red line in each box represent the median and the average, respectively. The upper and lower limits of the boxes are 75 and 25 percentiles of the data distribution. The figure is taken from our published paper [67].

The measurements at 800 nm targeting the total hemoglobin content show larger spectral slopes and smaller midband-fits in the cancerous group. Larger spectral slope (smaller absolute values as most of the spectra show descending trend) was observed in PCa by our and other groups [120, 122]. The midbanfit at 800nm is lower in the cancerous region. This agrees with a previous study reporting that blood flow decreases in prostate tumor [159].

At 266 nm, the broadband fiber optic hydrophone detected the high frequency signal components generated by the thin layer of epithelium cells in benign prostate tissues [121]. Therefore, the benign group shows high spectral slopes compared to the cancerous group where cancer cells form clusters with large dimensions. The fiber optic hydrophone has limited sensitivity to low frequency components. The low frequency signal components in the cancerous tissue were under-represented in the PASA quantification. As a result, the midbandfit of the cancerous group is lower than the benign group.

Figure 4-10 shows the results from the statistical analysis comparing the quantified PASA parameters from the benign and the cancerous regions at the four wavelengths. By performing the t-tests, the linear slope at each of the wavelength can differentiate the two groups with statistical significance, while the midbandfits at 800 nm and 266 nm can also differentiate the two groups with statistical significance. The midbandfits at 1220 nm and 1370 nm also show some difference between the two groups but no statistical significance.

4.4.2 Multivariate Parameter Analysis Using SVM

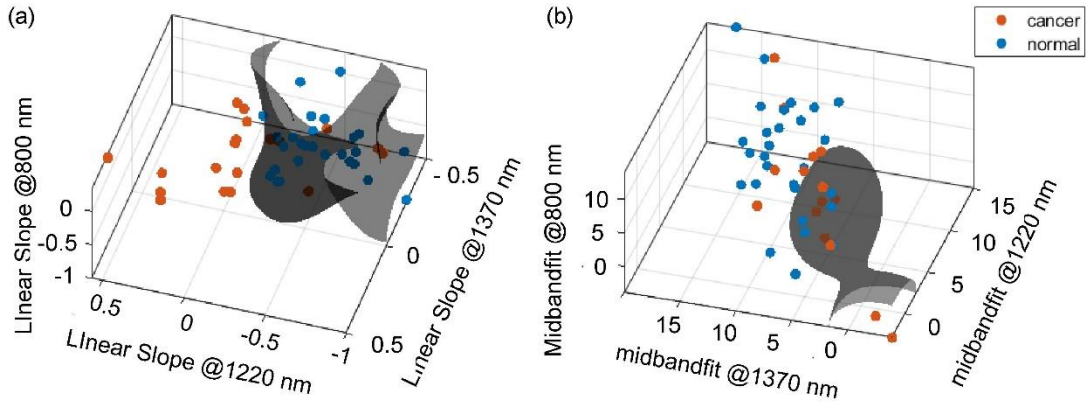


Figure 4-11: SVM based categorization between the benign and the cancerous groups at the wavelengths of 1220 nm, 1370 nm, and 800 nm using 49 measurements for the parameter of (a) linear slope and (b) midbandfit. The figure is taken from our published paper [67].

Since 266 nm measurements were not acquired in some of the samples, the multivariate analysis does not include the PASA quantifications at 266 nm. Figure 4-11 shows the scattered plot of all PASA values at 1220 nm, 1370 nm and 800 nm. The data points show differentiable clustering patterns. The decision surfaces in Figure 4-11 were calculated using all the 49 measurements at

the three wavelengths. The accuracy of the decision surface in separating the benign and the cancerous regions is 92%. Table 4-2 lists the accuracy of SVM classification with the measurements at individual wavelength and combined wavelengths using the 5-fold cross-validation approach described in Chapter 4.3. The highest classification accuracy was achieved by combining the PASA measurements at all the three wavelengths.

Table 4-2: The SVM statistical results using single wavelength or combined wavelengths. (5-fold cross validation, 80% learning, 20% testing) The table is taken from our published paper [67].

Wavelength (nm)	1220	1370	800	266	1220,1370,800
Spectral Slope (dB/MHz)	0.81	0.6	0.6	0.71	0.86
Midbandfit (dB)	0.67	0.67	0.77	0.57	0.8
Both	0.71	0.71	0.71	0.67	0.88

4.5 Discussion

In the simulation setup, a forward looking endocavity US array was used, although a side-viewing endocavity US array is commonly used in transperineal prostate biopsy. To match the US imaging field-of-view to that in the actual biopsy procedure, a 90-degree probe holder was fabricated. The translational needle PA sensing probe, with a diameter tightly fit to the introducer needle, was always oriented perpendicular to the central line of the convex US array surface. In US imaging, this orientation guarantees a robust reflection signal, which helps the operator in accurately positioning the needle probe. Furthermore, there is a marker along the entire needle body indicating the orientation of the measurement window which helps in matching with histologic diagnosis.

With dye injection following the PA measurements, we successfully correlated the PASA quantifications with the pathological diagnosis at each sampled location. The needle PA sensing probe is only capable of 1D measurements. Measurements taken close to the cancer boundaries were excluded from the statistical analysis because these measurements may contain unresolvable spectral characteristics of both benign and cancerous tissues. In future studies, we

plan to investigate uniform sampling and estimating the volume of a cancerous region by the distribution of the PASA quantifications. Considering the large sampling volume provided by the needle PA sensing probe, we may be able to cover the whole prostate volume with limited number of needle probe insertions.

Compared to the piezoelectric hydrophone in our previous studies [121, 120], the broadband fiber optic hydrophone significantly extended the frequency range in PASA. As shown in a pilot study [110], describing the histopathological diagnosis of PCa, i.e. Gleason scoring system, the dimensions of the cancer cell clusters are in the range of 10s to 100s of microns, which were covered by the frequency range of the fiber optic hydrophone in this study. Fine microscopic tissue architectures correlated to high frequency signal components, such as the thin layer of epithelium cells in benign prostate glands and connective tissues in cancerous regions, were resolved. The decrease in collagen and lipid content can also be observed using the midbanfit parameter, but with relatively low significance when compared to slope. The histopathologic diagnosis of PCa is based on tissue architecture rather than tissue content. Therefore, slope representing the tissue architecture is a more reliable parameter in this study compared to the midbandfit, which represents the content of a certain tissue component. These results agree with our predictions drawn from the results derived from piezoelectric hydrophones [121]. Since slope and midbandfit are two natural derivatives of PASA, we included both in this study. The fiber optic hydrophone with broad frequency range in this study improved the differentiability between the benign and cancerous regions. With limited sample number, we observed overlapping between the benign and cancerous group and we did not examine the correlation between the Gleason grades and the PASA quantifications as did in our previous studies [121] and Chapter 3. Further studies with larger sample size will help us understand the performance of the interstitial PA measurement approach in assessing the aggressiveness of PCa. We believe that including measurements at another wavelength, i.e 266 nm, will assist in better separating the samples in SVM analysis.

4.6 Conclusion

In this study, we examined the feasibility of integrating a miniaturized, all-optical needle PA sensing probe in a simulated TRUS guided transperineal biopsy procedure. PASA of the measurements acquired by this translational needle PA sensing probe successfully differentiated

between the benign and the cancerous regions in human prostates. This study using intact human prostates *ex vivo* paved the road toward clinical testing of our interstitial all-optical needle PA sensing probe powered by PASA for detecting and assessing the aggressiveness of PCa.

Chapter 5 Assessing Biomechanics of Aqueous Veins and Perilimbal Sclera Using Dual-Wavelength Photoacoustic Macroscopy System

In this chapter, we have combined dual-wavelength photoacoustic microscopy (PAM) and finite element analysis (FEA) technologies for the first time, enabling us to individually resolve and quantify strains in the aqueous veins and surrounding perilimbal sclera at high resolution. Our successful demonstration highlights that vasodilation of aqueous veins is constrained when the perilimbal scleral tissue they reside in exhibits stiffness. Further information about the integrated imaging and strain analysis method, as well as preliminary results, can be found in our published paper [147]. A more comprehensive description of the imaging method and results, as described in chapter 5.2, is currently in preparation for a separate manuscript. In this collaborative work, my primary contributions involved conducting PAM imaging and pre-processing the data, as detailed in Chapter 5.3.2.1, for subsequent strain analysis.

5.1 Introduction

Glaucoma is a widely prevalent ocular disorder that can cause vision loss among individuals aged 45 years and above. The major risk factor associated with the progression of this disease is an elevated intraocular pressure (IOP) [137]. Prior studies indicate IOP buildup occurs due to the resistance to the outflow of aqueous humor beyond the trabecular meshwork in the aqueous drainage tract [138, 139]. In addition, biomechanics of perilimbal sclera tissues on the aqueous veins have been identified as a potential factor in negative regulator of IOP. This idea has been exploited in several IOP-lowering treatments, including invasive surgical procedures such as

trabeculectomy [139, 142, 143]. However, due to a lack of comprehensive understanding regarding

the mechanisms of perilimbal sclera system, all these treatments have exhibited high failure rates and variable outcomes [144, 140].

In order to gain a deeper understanding of the perilimbal sclera mechanisms governing the aqueous outflow system, imaging has been established as an essential prerequisite approach for histological level analysis [145, 146]. Anatomy imaging uncovers structure features that can be used to explain how aqueous humor passes through the outflow system, thereby providing insights into its functional analysis. Our recent research indicates a strong correlation between IOP and the stiffness of the perilimbal sclera [147, 149]. This relationship manifests as biomechanical responses, including deformation of both the sclera and vessels in aqueous veins. Based on these findings, imaging techniques can be effectively utilized to track deformation and identify potential biomarkers that can predict IOP.

Given the complexity of the aqueous vein anatomy, high-resolution, deep penetration, and three-dimensional (3D) imaging is required. Animal models, such as porcine eye [150, 151], bovine eye [152], and nonhuman primates [151, 153], as well as *ex vivo* human eyes [154, 155] have been studied using traditional optical microscopy, scanning electron microscopy, transmission electron and Optical coherence tomography (OCT). However, these approaches have limitations in terms of either penetration depth or imaging resolution [156, 157]. To achieve 3D imaging, Ribbon-scanning confocal microscopy was initially developed by Dr. Simon C Watkins Group, but the images on porcine and human eye did not capture the entire complex vein structures [158]. Optical coherence tomography (OCT), for the first time, enables non-invasive visualization of the vasculature in the anterior segment of the eye. Nevertheless, OCT has difficulty in resolving the intricate vasculature due to the strong light scattering from the surrounding perilimbal sclera [159]. On the other hand, OCT is impossible to differentiate between vascular structures filled with aqueous and blood. OCT-Angiograpgy (OCT-A) addresses this issue by allowing the detection of blood flow within vessels *in vivo*, though aqueous-carrying vessels remain indistinguishable [160, 161]. The aqueous veins serve as conduits for the aqueous humor from the anterior chamber and the trabecular meshwork or conventional outflow pathway. However, the limited number of red blood cells in aqueous veins is insufficient to provide scattering contrast for OCT-A, making it difficult to clearly define the aqueous vein boundaries for precise strain analysis. Additionally, distinguishing between

episcleral, intrascleral, and aqueous veins necessitates empirical thresholding. Consequently, both OCT and OCT-A involve uncertainty when aqueous veins are of specific interest.

PAM is a non-invasive and non-ionizing imaging technology that uses acoustic waves generated by optical energy to create high-resolution images [162, 163]. With its fast-scanning rate and deep penetration, PAM offers dynamic imaging similar to OCT-A. By utilizing optical contrast agents, PAM can distinguish the aqueous veins from their surrounding perilimbal scleral tissue and other complex vascular structures in 3D. This makes PAM a promising tool for real-time imaging and functional analysis of *ex vivo* human eyes.

The other advantage of PAM system is its ability in targeting different components, such as sclera and veins, based on their unique optical absorption profiles. Imaging both aqueous veins and perilimbal sclera tissues individually is crucial for gaining a deeper understanding of their interrelationship. Although numerous studies have examined the relationship between posterior scleral biomechanics and IOP in glaucoma, there is limited knowledge regarding the perilimbal sclera area. According to our earlier studies [149], we demonstrated a significant correlation between increased mechanical stiffness of the perilimbal sclera and elevated pressure of the steady-state outflow. Therefore, there is a biomechanical interaction between the perilimbal sclera and distal aqueous outflow. In summary, acquiring distinct images of both aqueous veins and perilimbal sclera is critical for obtaining a deeper understanding of their relationship.

The investigation of strain plays a critical role in biomechanics studies of the human eye, and several studies have experimentally determined surface strains on the outer surface of sclera. For example, previous studies employed camera imaging and laser speckle interferometry to measure 2D and 3D surface displacements for computation of biaxial strains in porcine and human eyes [186, 187]. The results revealed that tensile surface strain of the parapapillary sclera was statistically significantly greater than the mid-peripheral sclera, based only on the surface strain measurements. However, calculation of strain within soft tissue demands an imaging modality that can penetrate the tissue, which is more challenging. In an earlier study [188], an ultrasound elasticity microscope in conjunction with finite element methods was employed to determine strains within porcine corneal tissue. This study provides the biomechanical analysis for refractive surgery on cornea. Another work used displacements measured by ultrasound speckle tracking to determine the strains through the tissue's thickness by direct numerical calculation

[189]. The results show in-plane stretching of cornea with through the thickness compression, as also found in the present manuscript for sclera. However, ultrasound imaging has limited spatial resolution and cannot distinguish the deformation of vasculatures from that of the perilimbal sclera tissue. The biomechanics of the connected cornea-limbus-sclera tissues of the porcine eye has also been studied in [190]. Variations in elastic properties as a function of IOP were inferred from measurements of the speed of propagating Lamb waves induced in the tissue. Strains were not measured, but finite element simulations of the tissues provide validation of the measured trends. The strains within the tissues of human lamina cribrosa and adjacent sclera were recently studied in [175]. Whole globes were resected into hemispherical sclera segments that were fixed to a support along the cut edge. Imaging was conducted by laser-scanning microscopy and digital volume correlation to determine displacement fields from which strains were directly calculated from the strain-displacement equations. As the results showed, the method is able to resolve tissue displacements within the sclera with sufficient accuracy for strain calculations. Overall, the investigation of strains can be a useful parameter in biomechanics studies of eyes, and several techniques have been employed to determine strains within ocular tissues, each with its own advantages and limitations.

In this chapter, a new method is introduced that uses dual-wavelength PAM to capture 3D displacement fields within soft tissue and veins along with FEA to calculate the corresponding strains based on the measured data [169]. Initially, the imaging capability of a dual-wavelength PAM system was demonstrated for the capability to image aqueous veins and surrounding perilimbal sclera using two wavelengths, namely 532nm and 1200nm. These wavelengths were employed to target red tattoo ink injected into aqueous veins and collagen-rich sclera. The circumferential limbal of the sclera and vascular anatomy was scanned independently in both porcine and human eyes *ex vivo*. The PAM-FEA approach was subsequently validated for its ability to comprehend the biomechanical behavior of tensile testing and the posterior porcine eye *ex vivo*. Finally, the method was applied to a large batch of porcine eyes for statistical analysis to understand the relationship between aqueous veins and surrounding perilimbal sclera.

5.2 Combined Sclera and Vessel Imaging Using Dual-Wavelength Photoacoustic Microscopy System

5.2.1 Imaging System Setup

Figure 5-1 displays the experimental diagram of the dual-wavelength PAM system. A single mode laser (GLPN-532-QCW, IPG Photonics, duration 1.4 ns, power 100W, wavelength 532nm) was employed to provide pulses at the wavelength of 532nm. The second laser from the same company at the wavelength of 1064 nm (YLPN-1-1×350-50, IPG Photonics, duration 4ns, power 50W, wavelength 1064nm) was tuned to 1200nm-centered pulse using a 60m-long single mode

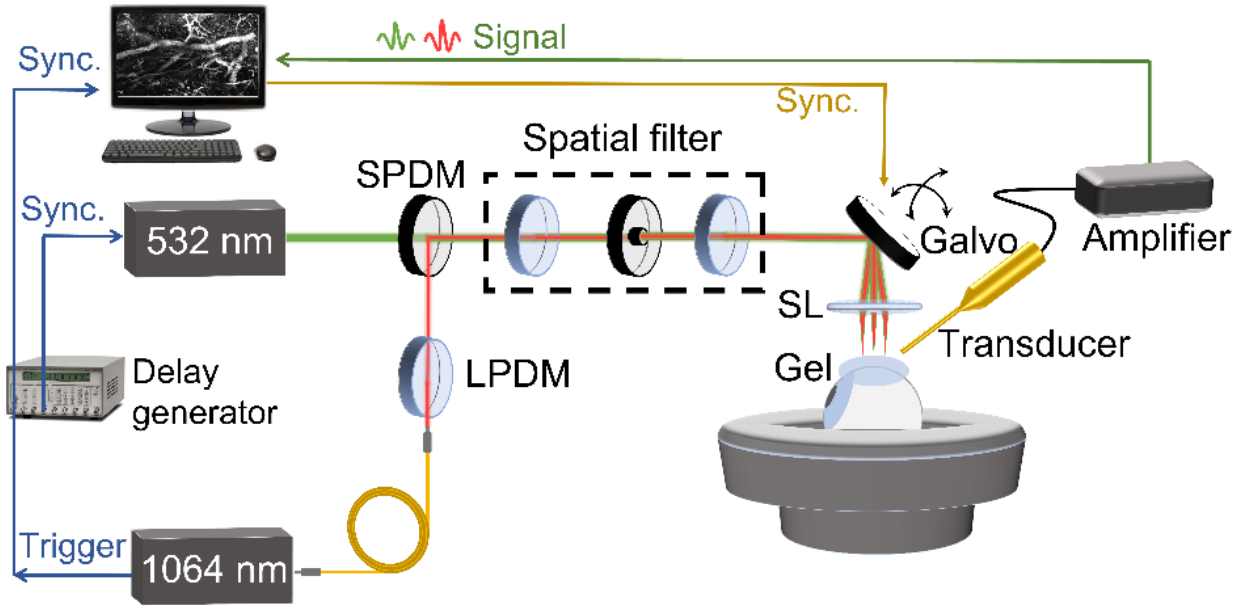


Figure 5-1: The integrated dual-wavelength photoacoustic microscopy system. LPDM: long pass dichroic mirror (cut-off wavelength 1150 nm), SPDM: short pass dichroic mirror (cut-off wavelength 900 nm), BS: beam splitter, SL: scan lens. The green light pass is at the wavelength of 532 nm while the red laser path is centered at the wavelength of 1200 nm. This figure is adapted from a manuscript currently in preparation.

polarized fiber (HB1060Z, Thorlabs) and a long pass filter (cutoff wavelength 1150nm). Both lasers operated at a repetition rate of 11 kHz and were aligned coaxially as shown in Figure 5-1. These two wavelengths were chosen to maximize the difference of optical absorption between vessel contrast agents (red dye) and tissue collagen. Then, the 1200nm-centered wavelength beam (red line) and 532nm wavelength beam (green line) went through a spatial filter to obtain two Gaussian shape beams with 3mm diameter. Following coaxial collimation and beam reshape, these two wavelengths were focused on the sample surface by a scan lens (focal length 36 mm,

LSM03-BB, Thorlabs, Inc., Newton, NJ) and scanned in three dimensions by moving the galvanometer in two directions. The system scanned the porcine eye or human eye using the dual-wavelength laser beams with a delay time of 3 μs between two wavelength pulses.

The generated PA signals at two wavelengths were captured using a needle-like ultrasound transducer (Optosonic Inc., Arcadia, CA, center frequency: 27 MHz, two-way 6 dB bandwidth). The transducer was placed at an angle of approximately 60 degrees vertically to the eye surface. A few drops of the GONAK gel (2.5% sterile Hypromellose ophthalmic demulcent solution, Gonak®) were used as an acoustic coupler to submerge the imaging area and ultrasound transducer. The GONAK gel was chosen because it generates ignorable PA signals at both wavelengths compared to the tissue signals. The PA signals were then amplified using a 70dB amplifier (Pasternack, CA) and converted to digital signals, and stored in the computer using a digital (A/D) card (CSE16502, Gage, Vitrek, LLC 2022, IL). The lasers, galvo component, and digitizer were synced using an I/O card (USB-6353, National Instruments Corporation, Austin, TX). Overall, the system achieved the resolution of 6um in axial directions, 36μm in longitudinal direction.

To ensure a flat region of interest (ROI) on the eye surface, a freely rotating eye holder was utilized in this study. The holder fixed the lower half of the porcine eye at the holder base, while the upper half was exposed for imaging. The scanned image volume in 3D was 400 x 400 x 2048, targeting a projected imaging area of 1.5mm x 1.5mm. The sampling rate in the axial direction was 250 MHz. Due to the porcine eye's larger size and the transducer's limited field of view, a circumferential image view was obtained by rotating the eye at 20-degree increments, based on the eye center. After approximately 20 rotations, the perilimbal area of the entire eye was imaged. Finally, the 20 individual B-mode images at each wavelength were meticulously stitched together based on their overlapping regions to create a complete image.

5.2.2 Imaging of Phantoms

5.2.2.1 Phantom Preparation

In this study, red tattoo ink was selected as the contrast agent for aqueous seins. To investigate the feasibility of distinguishing between the red contrast agent and surrounding tissue components, a phantom was first employed. The phantom comprised a hair, fishing line, and a

line of red tattoo ink, as illustrated in Figure 5-2. The fishing line had an optical absorption peak around 1200 nm [164], while the red tattoo ink could be visualized using green light. All these three lines were secured in 3% porcine gel (G2500, Sigma-Aldrich Co. LLC., Burlington, MA).

5.2.2.2 Results

Figure 5-2 illustrates that, in contrast to the hair that is always visible, the fishing line and red line are only visible at 1200nm and 532nm wavelengths, respectively. The fishing line is rich in C-H bonds, which are similar to the chemical structure of sclera (collagen). Therefore, the phantom study demonstrated the system's capability to differentiate the optical contrasts between red tattoo ink and C-H bond-rich materials, such as sclera.

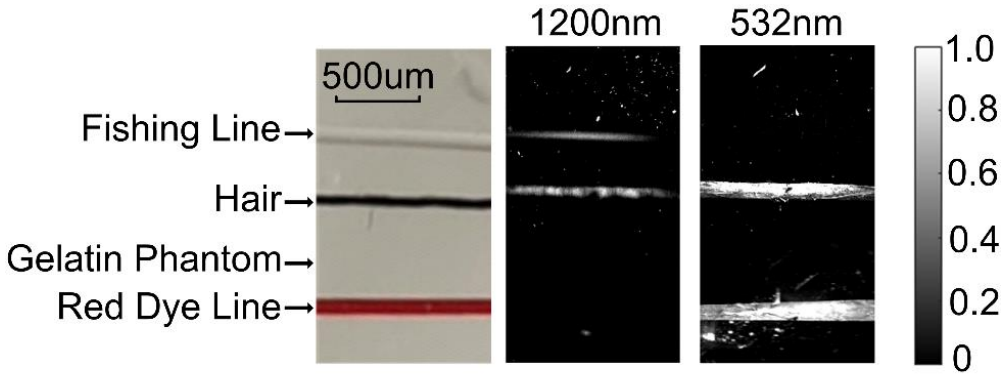


Figure 5-2: Two-dimensional image at 532nm and 1200nm of the three-line phantom made of hair, fishing line and red dye line. The left image is the picture under the camera. The middle and right images were acquired at the wavelengths of 1200nm and 532nm separately. This figure is adapted from a manuscript currently in preparation.

5.2.3 Imaging of *Ex Vivo* Porcine Eyes and Human Eye

5.2.3.1 Eye Preparation

There are two main challenges when it comes to imagining the entire porcine eye. Firstly, the blood in the venous system of *ex vivo* porcine eyes fades away, and secondly, the aqueous humor in other tubular systems such as Schlemm's canal is transparent. To address these challenges, red tattoo ink was utilized to enhance the contrast of the anterior tubular system, and porcine gel was applied to prevent the contrast agent from flowing out of the vessels. The combined contrast agent consisted of 3% porcine gel, which was uniformly mixed with 5% red tattoo ink ("Dragon's Breath," Kuro Sumi Corp., Fort Mill, SC), diluted by the balanced salt solution (BSS).

After injecting the combined contrast agent into the eye, the eye was left to solidify for 30 minutes.

5.2.3.2 Results

The combined dual-wavelength photoacoustic (PA) images of whole *ex vivo* porcine eyes in three cases are shown in Figures 5-3 to 5-5. These images reveal the dense vasculature of aqueous veins, which was enhanced with the injection of red tattoo ink and illumination at the

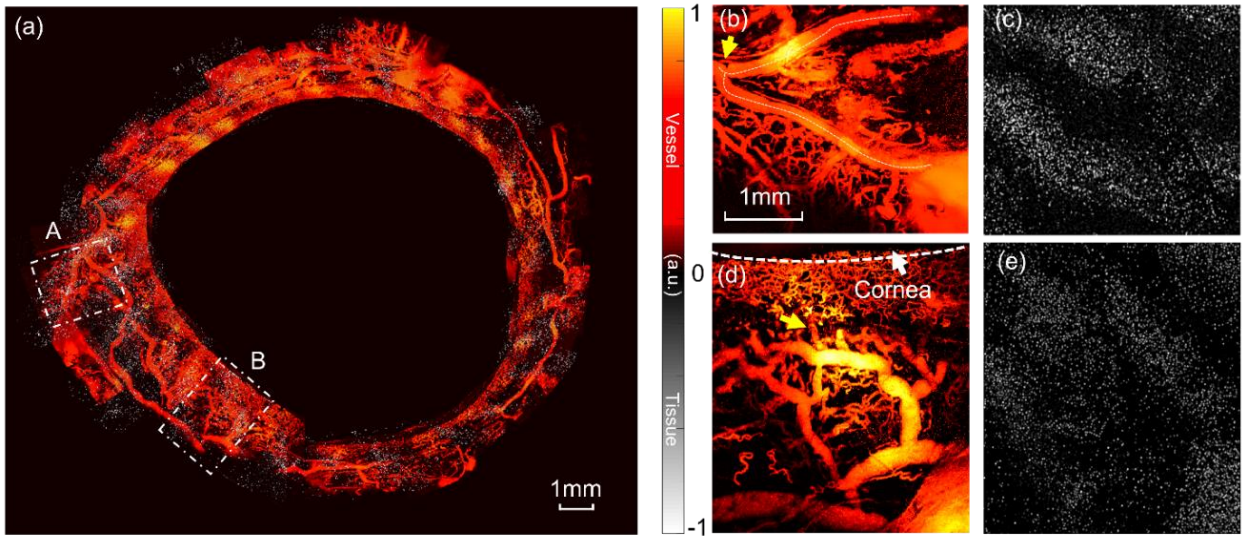


Figure 5-3: Circumferential aqueous vasculatures and surrounding sclera tissues of the whole porcine eye imaged using the integrated dual-wavelength photoacoustic microscopy system in Figure 5-1. (a) The combined whole image of aqueous veins and surrounding sclera tissues. The magnified features of veins and sclera tissues of the area A and B in the white boxes in (a) are shown in (b-c) and (d-e), respectively. The cornea is represented by a white circle and a white arrow in (b) and (d). The yellow arrows represent aqueous veins. This figure is adapted from a manuscript currently in preparation.

wavelength of 532nm. The small vessels are distributed circumferentially in a homogeneous manner from the limbus to the periphery, with primary aqueous veins exhibiting a striated or laminated variety and diameters ranging from 100-300 micrometers, as demonstrated in Figure 5-3(b&d) and Figure 5-5(b). In Figure 5-4(b) and 5-4(d), the aqueous veins are located below the superficial scleral plexus layer or connected to the thin veins, supporting the anastomotic conclusion that aqueous veins are directly related to the small sclera plexus [146]. At the wavelength of 1200 nm, distribution patterns exist around the circle of the eye as seen from Figure 5-3 to Figure 5-5, generated by the collagen-rich sclera tissues [108].

In addition to the porcine eye images, we also imaged the entire human eye, as shown in Figure 5-6. A comparison of these images with those of the porcine eye reveals that the diameter of the aqueous veins in the human eye is finer, ranging from 50-100 micrometers proximally. In Figure 5-6(b-d), the yellow arrow indicates the aqueous veins originating from Schlemm's canal, which has a hook shape and spreads into the dense branch in the lower sclera plexus. The imaging depth of the human eye was found to be as deep as 350 μm, as shown in the subsection picture of vasculatures in Figure 5-7(a), with depth information given in color scalers. Cross-sectional images at the yellow dashed line in Figure 5-7(a) were Figure 5-7(b) shows the PA B-mod e image acquired at the wavelength of 1220 nm, with uniform PA signal background across the thickness of around 400 μm. The imaging depth is related to the imaging penetration, and some PA signals with higher intensities distributed randomly within the uniform PA signals. Current research suggests that the healthy corneal epithelium, which is mostly formed of collagen, is uniformly constructed, but some irregularity appears when the eye is swollen. Therefore, the stronger PA signal distributions may be due to the collagen cluster with a higher concentration caused by the swollen eye during dye injection. The yellow arrows in Figure 5-7(b-c) indicate the PA signals created by melanin precipitation, which can be observed at both wavelengths.

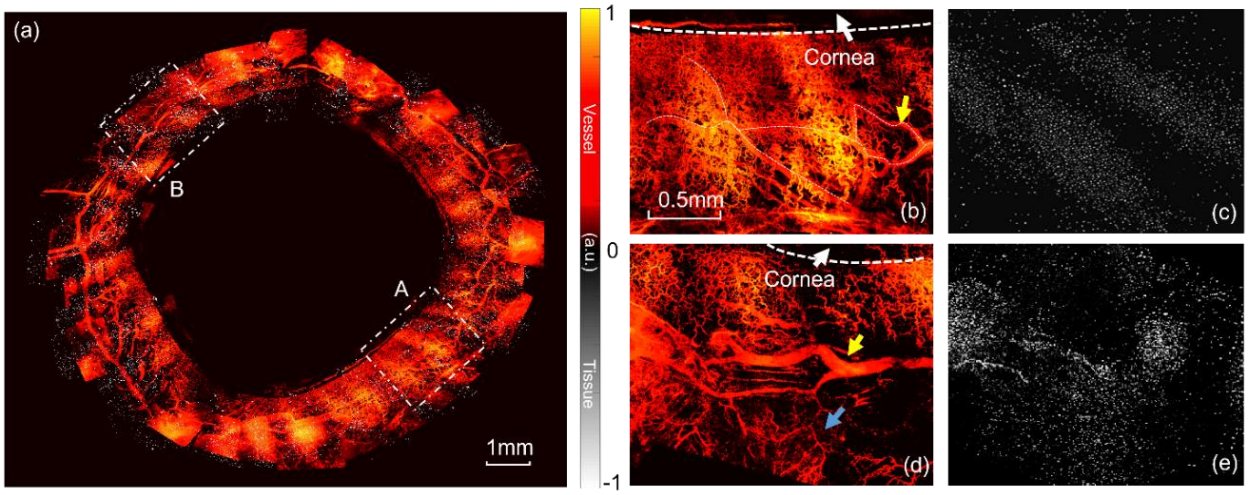


Figure 5-4: Circumferential aqueous vasculatures and surrounding sclera tissues of the 2nd whole porcine eye imaged using the integrated dual-wavelength photoacoustic microscopy system in Figure 5-1. (a) The combined whole image of aqueous veins and surrounding sclera tissues. The magnified features of veins and sclera tissues of the area A and B in the white boxes in (a) are shown in (b-c) and (d-e), respectively. The cornea is represented by a white circle and a white arrow in (b) and (d). The yellow arrows represent aqueous veins, while the blue arrows represent thin and small scleral plexus branches. This figure is adapted from a manuscript currently in preparation.

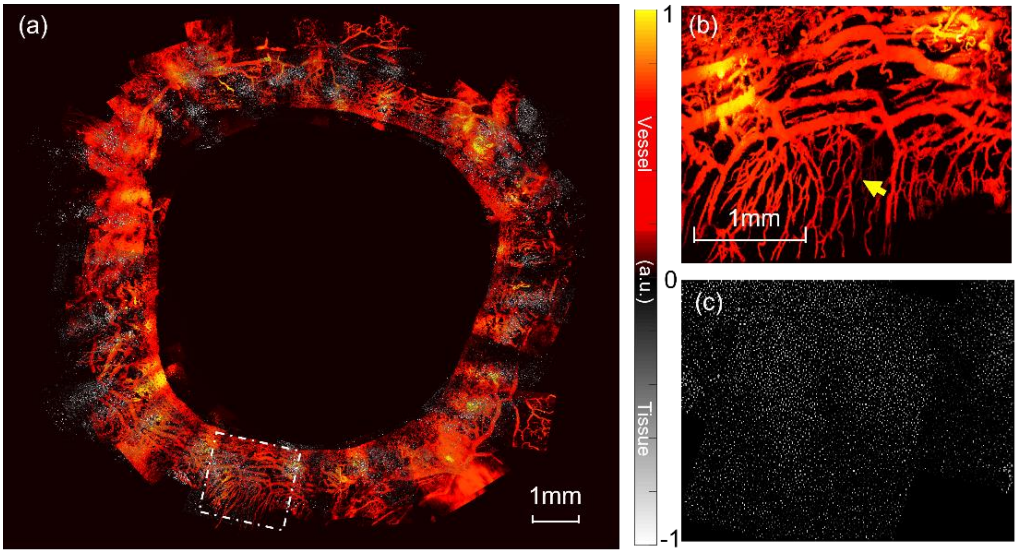


Figure 5-5: Circumferential aqueous vasculatures and surrounding sclera tissues of the 3rd whole porcine eye imaged using the integrated dual-wavelength photoacoustic microscopy system in Figure 5-1. (a) The combined whole image of aqueous veins and surrounding sclera tissues. The magnified features of veins and sclera tissues of the area in the white box in (a) are shown in (b) and (c), respectively. The yellow arrows represent aqueous veins. This figure is adapted from a manuscript currently in preparation.

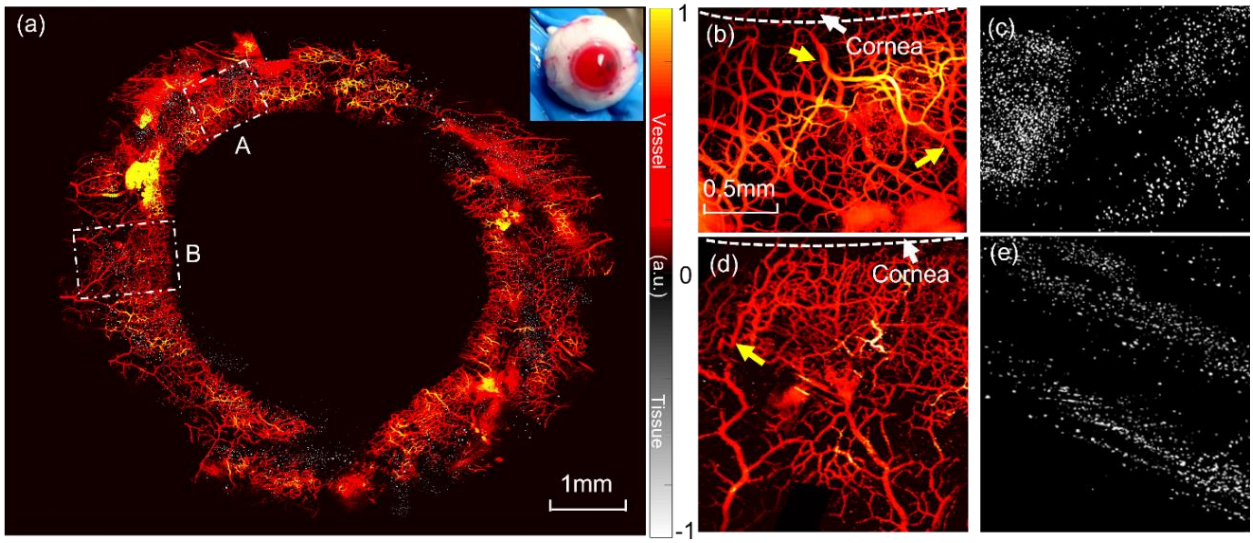


Figure 5-6: Circumferential aqueous vasculature and surrounding sclera tissues of a whole human eye imaged using the integrated dual-wavelength photoacoustic microscopy system in Figure 5-1. The magnified features of veins and sclera tissues of the area A and B in the white boxes in (a) are shown in (b-c) and (d-e), respectively. The cornea is represented by a white circle and a white arrow in (b) and (d). The yellow arrows indicate aqueous veins. This figure is adapted from a manuscript currently in preparation.

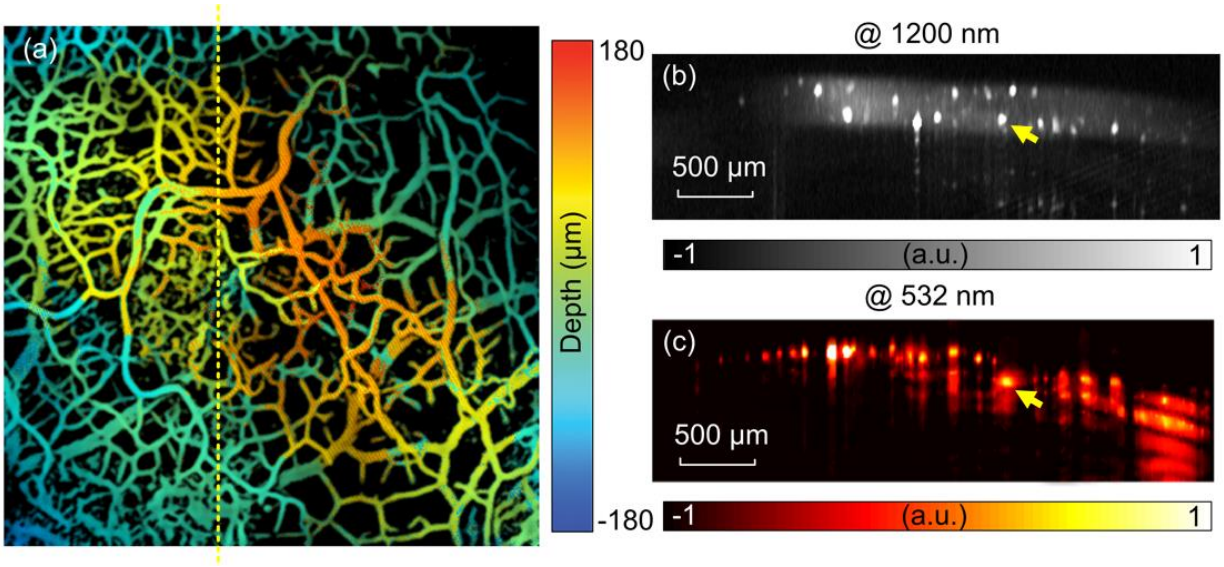


Figure 5-7: Photoacoustic image example of a subsection of the human eye. (a) The vasculature image acquired at 532 nm. The color scale shows the depth of individual vessels. (b) A cross-section image was obtained across the yellow dotted line in (a) at the wavelength of 1220 nm. (c) A cross-section image scanned at the yellow dotted line in (a) at the wavelength of 532 nm. The color scales in (b) and (c) represent the signal intensity. The yellow arrows indicate the signals generated by melanin. This figure is adapted from a manuscript currently in preparation.

5.3 The Biomechanical Analysis of Aqueous Veins and Perilimbal Sclera by Three-dimensional Photoacoustic Imaging and Strain Field Calculation

As described in the preceding section, the PAM system has been successfully validated. In this section, we introduce a novel PAM-based FEM method and utilize it to investigate the

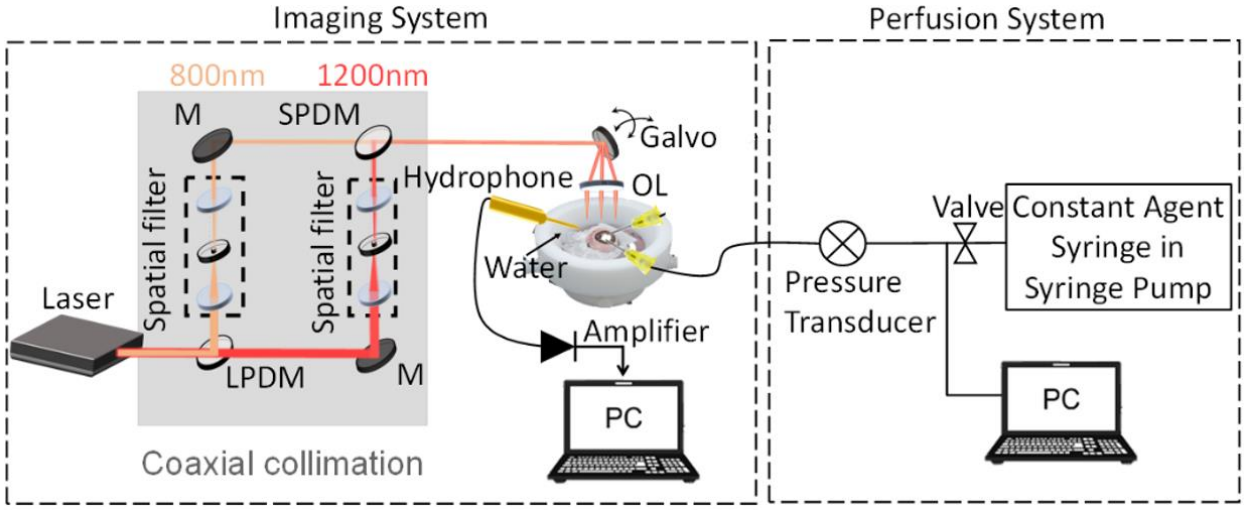


Figure 5-8: Experiment setup. The entire system is composed of imaging system which is the same as the system in Figure 5-1 and a perfusion system to control eye pressure. This figure is adapted from our unpublished data and restructured based on the figure presented in our published paper [147].

correlation between aqueous veins and perilimbal sclera tissues in a significant number of porcine eyes.

5.3.1 System Setup

The experimental setup comprises two primary components, namely the perfusion system and the PAM imaging system, as depicted in Figure 5-8. To maintain the eye in a stable position during perfusion, a custom-made double-wall holder is utilized, and the eye is affixed with ultrasound gel. The holder surrounds the posterior two-thirds of the eye, enabling the eye to expand and contract freely during perfusion while remaining relatively immobile.

5.3.1.1 Perfusion System

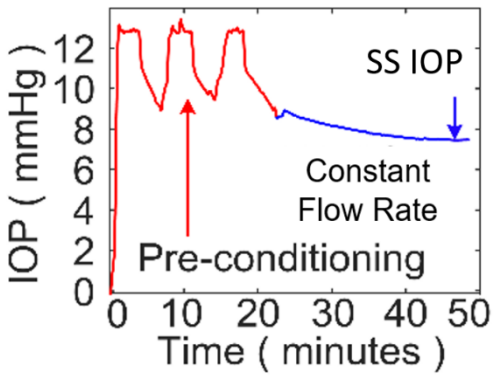


Figure 5-9: The eye perfusion procedures. SS IOP: steady state intraocular pressure. This figure is adapted from unpublished data.

Enucleated eyes were prepared for the experiment by conditioning them in the perfusion system shown in Figure 5-8, following the procedures outlined in a previous study [149]. The arrangement of the perfusion system included 3/32-inch flexible tubing, a pressure sensor (Argon DTXPlus Model DT-XX, Argon Critical Care Systems Singapore Pte. Ltd, Singapore), one 21-gauge needle, a 10 cc syringes, a syringe pump and a data acquisition system. First, Air bubbles were removed from the system by slowly drawing the fluids in and out of the tubing and sensor until all bubbles clear. The needle of the BSS diluted indocyanine green (ICG) (mixed at its stock concentration of 5%) was inserted through the cornea and into the anterior chamber. After inserted, the needle was guided carefully to the drainage angle and gently, yet firmly used to cut through an approximately 45° arc segment of the trabecular meshwork to perform a

trabeculotomy. The trabeculotomy decreases resistance and allows the contrast agent to access the aqueous veins more readily. The eye was then preconditioned with the ICG solution via a pressurization/relaxation process to return the tissues to a near-physiological biomechanical condition [149]. ICG was selected due to its smaller particle size, which minimizes the likelihood of vessel blockage. Three circles of preconditions were performed for each eye as displayed in Figure 5-9. After preconditioning, the IOP tuning procedures were completed by the syringe pump with real-time pressure monitoring. The contrast agent was then perfused at a constant flow rate of 3 µl/min to adjust the intraocular pressure (IOP) to a steady state in the eye. Subsequently, the flow rate was raised to 6 µl/min to elevate the IOP to 35 mmHg.

Steady-state intraocular pressure (IOP) is a measure of outflow facility, defined as the ratio of constant flow rate to the resulting steady-state IOP [194]. A lower steady-state IOP at the same perfusion flow rate indicates greater outflow facility, whereas a higher steady-state IOP indicates lower outflow facility. In Chapter 5.3.2.3 [149], we found a strong correlation between the perilimbal sclera stiffness, based on tensile tests of tissue specimens, and the steady state IOP. A later study showed that the limbus tissue plays an important role in IOP compensation using dissected human tissues [195]. Another study measured the shear moduli of sclera in whole porcine eyes using optical coherence elastography and an inverse finite element model [190]. The results also showed a strong correlation between the biomechanical properties of perilimbal sclera and IOP. Thus, steady state is an important parameter to represent the stiffness of the measured component.

5.3.1.2 Imaging System

Figure 5-8 depicts the dual-wavelength optical resolution PAM system with a lateral resolution of 4 µm for 800nm and 8 µm for 1200nm, and an axial resolution of 37 µm for all wavelengths, as reported by reference [196]. This imaging system is identical to the one presented in Figure 5-1. In this study, illumination at 800nm for ICG agent and 1200 nm for sclera were generated by a diode-pumped solid-state laser (NT-242, Ekspla, Vilnius, Lithuania, tuneable wavelength range 405 – 2600 nm). The laser output was less than 80 µJ per pulse, with a pulse duration of 5 ns and repetition rate of 500 Hz. These two wavelengths were collimated by spatial filters and illuminated at the same location of the objective. The scanning beam, which was directed by a galvo mirror, was focused on the surface of the eye globe that was immersed in GONAK gel

using an objective lens (LSM03-BB, Thorlabs, NJ). The signals were collected by a needle hydrophone (30MHz central frequency with 50% bandwidth at -3 dB range, customized by The Ultrasound Institute at The University of South California), amplified by 57 dB (AU-1647, L3 Narda-MITEQ, NY) and transferred to a computer at a sampling rate of 250MHz. The two-dimensional projection image within the region of interest (ROI) in a volume was approximately 2 mm x 2 mm, as reported in the preliminary study. During the IOP increase for each eye, a series of photoacoustic images were taken at 4 mmHg intervals.

5.3.2 Strain Calculation Method

The subsequent sections delineate our analysis approach, referred to as Photoacoustic Imaging and Finite Element Analysis (PAI-FEA). My personal contributions to this research can be found in Chapter 5.3.2.1, while Chapter 5.3.2.2 highlights the work completed by our collaborators in Dr. Alan Argento's group.

5.3.2.1 Feature Tracking and Finite Element Mesh Generation

For quantifying the deformations within the tissue, the displacements of the spatial features in the photoacoustic image series were first tracked automatically in 2D or 3D. The method used is first described for the 2D case. Pixels with 55% contrast over any of their neighboring ones were identified in the arbitrary reference state (a near-zero strain state) of the image series and iteratively tracked as shown in Figure 5-10(b) and (g). A 21x21 pixel image patch area with the tracked pixel at the center was first selected. The center of a sliding window with the same dimension then scanned a 61x61 pixel area around the current location of the tracked pixel in the following frame. The location in the scanned area with the largest correlation coefficient was determined as the new location of the tracked feature points [168]. For ensuring tracking accuracy, the procedure was empirically repeated with a patch size of 31x31 and 41x41 pixels. If the new locations derived with the three patch sizes fell in a narrow range of 1 pixel, the new location was determined as the averaged location rounded to the nearest pixel. Otherwise, the current pixel was disregarded, and the process proceeded to the next pixel. This method produced displacements of at least 100 pixels in a 100x100 μm^2 region, providing sufficient accuracy for strain calculation. The same method was used in the 3D tracking algorithm, except the correlation coefficients were calculated using 21x21x41, 31x31x51 and 41x41x71 pixel

sliding windows, the center of which scanned over a 61x61x101 voxel space around the tracked voxel. The examples of tracked results at low and high pressures are shown in Figure 5-10 (c) and (h).

Optical contrasts for tracking points were created by passage of the contrast agent into the aqueous veins which stain the veins thereby providing trackable points, as described above. Here, strains in the veins were calculated directly via the tracked displacements of stained points on the deforming veins. The average strain in a segment of sclera bordered by stained veins was also calculated using the displacements of points on the veins.

In any case, the points tracked through all the frames were used for finite element mesh generation. Aimed at element size uniformity, one point was retained within any surface area with a radius of approximately 30 - 300 μm, depending on the size of images, in the reference frame. The retained points were defined as the nodes in the finite element mesh. The element lists were generated using the coordinates of the nodes with a built-in function, delaunayTriangulation, in MATLAB.

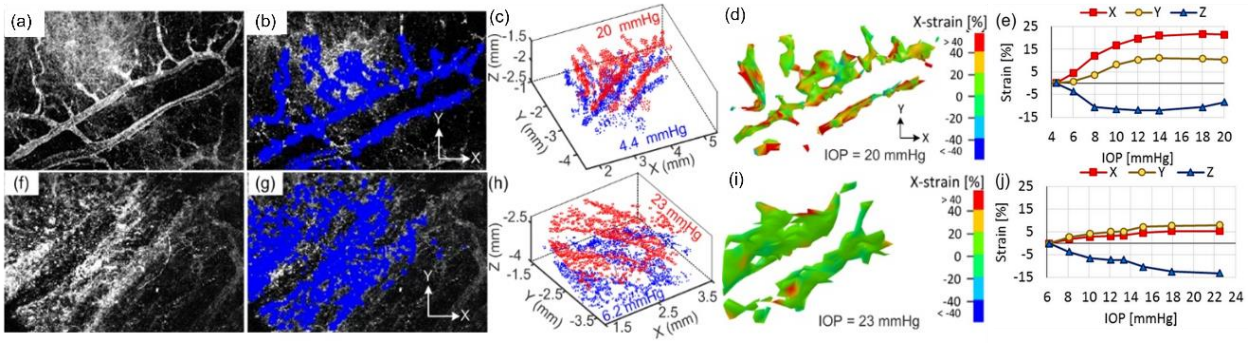


Figure 5-10: The examples using PAM-FEA analysis method. (a) The reference image of vein image acquired at 800 nm. (f) The reference image of the sclera tissue with black tattoo acquired at 800nm. (b), (g) The feature points extracted from reference images in image (a) and (f). (c), (h) The examples of tracked results in the reference image and the last image at the highest pressure. (d), (i) The calculated localized strain distributions in x direction. (e), (j) The averaged strains in x and y and z direction. The direction of x and y is labeled in figure (b) and (g), while z direction is perpendicular to the x and y directions. This figure is adapted from a manuscript currently in preparation. This figure is reorganized using both our published paper [147] and unpublished data.

5.3.2.2 Strain Calculation

To calculate strains, a set of generated elements in the near-zero strain state was imported into LS-DYNA, a finite element package (version 971d, Livermore Software Technology

Corporation, Livermore, CA), resulting in a mesh of constant-strain solid elements. The strain engine of the program was used to calculate the 3D strains of the elements. The average strains of connected elements were determined at each nodal point, and nodal strain values were interpolated within the elements to determine the spatial distribution of strains. The tracked displacement vectors between image frames were incorporated as prescribed nodal motions in the developed finite element model, and the resulting strain fields were computed at various intraocular pressures. This method is similar to the one used to determine the strain fields in scleral collagen fibers in a recent study [169]. The localized strain distributions in three directions (x, y, and z) were calculated using the linear, true strain model in LS-DYNA and are displayed in Figure 5-10(d) and (i). In some results, the average strain (denoted by an overbar, as in $\bar{\varepsilon}$) of an imaged region in three directions was computed as shown in Figure 5-10 (e) and (j). This provides a measure of the overall deformation or strain within a specific ROI, which can be useful for comparing results between different samples or conditions.

5.3.2.3 Validation of the Strain Measurements Using Tensile Preparation

5.3.2.3.1 Tensile Preparation

To validate the PAI-FEA strain measurements, simultaneous conventional tensile tests were conducted on low modulus, thermoplastic elastomer (Dupont Hytrel 4069) rectangle specimen with the size of 13 mm x 3.1 mm x 1 mm (length x width x thickness). As shown in Figure 5-11(a), a pattern of speckles created on the specimen by lightly sprayed red paint was used to create contrast tracking points. The tensile test apparatus consists of a pair of in-line grips attached to a pair of micrometers that were fixed to mounting structures at the free ends of the tensile specimen. After the tensile test apparatus fixed under the PAM system, the rectangle specimen was deformed in 0.05 mm increments by adjustment of the micrometers while PA imaging, tracking and strain calculation were conducted after each step using the methods described above. The imaging wavelength used in this test is 532nm instead of 800nm to target red tattoo dye.

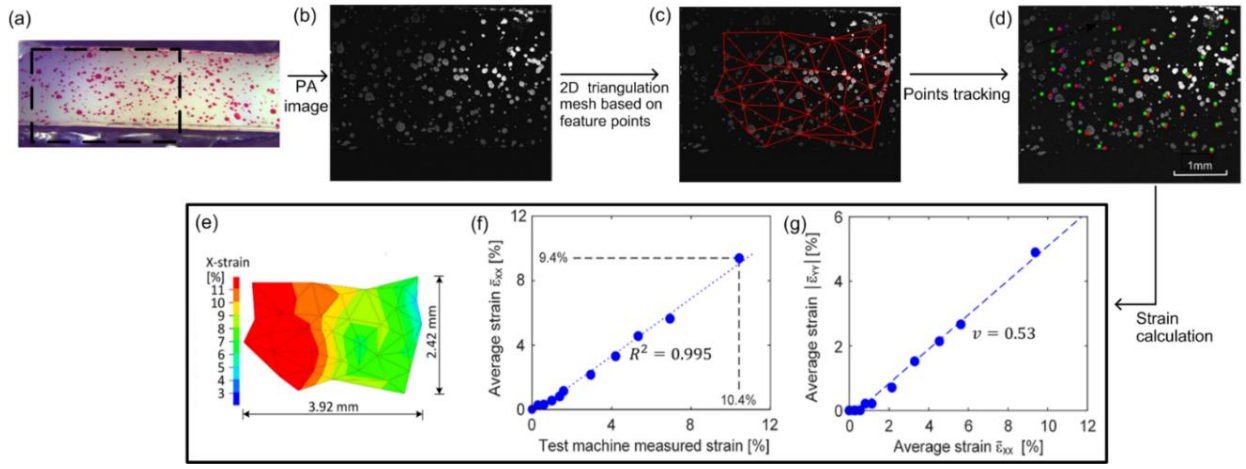


Figure 5-11: Tensile validation using PAM-FEA approach. (a)(b)(c) are photo of an undeformed elastomer specimen, photoacoustic image, and mesh image composed of feature points at each corner of triangle, respectively. (d) is a photoacoustic image with overlaid points identified and tracked from the reference image (blue dots) and two deformed images stretched 0.55 mm (red dots) and 1.4 mm (green dots). (e) is the deformed mesh with the color map of the strain $\bar{\varepsilon}_{XX}$ at the end of the stretch test. (f) is the average strain $\bar{\varepsilon}_{XX}$ determined by PAM-FEA versus strain determined from the distance between the test machine grips. (g) is the average strain $|\bar{\varepsilon}_{YY}|$ (absolute value of compressive strain in the Y-direction) versus $\bar{\varepsilon}_{XX}$ determined by PAM-FEA. This figure is adapted from our published paper [147].

5.3.2.3.2 Results

Figure 5-11(a) shows a portion of the elastomer specimen mounted in grips. Only the left side of the symmetric specimen was imaged and the overall dimension of the undeformed mesh with 52 triangular elements is approximately 3.56 mm by 2.56 mm as shown in the figure. The specimen was stretched in the X-direction. Figure 5-11(b) is the PA 2D images of the picture in Figure 5-11(a). Figure 5-11(c) shows a photoacoustic image of the reference undeformed image with triangle mesh built on retained points. Figure 5-11(d) shows the reference photoacoustic image with identified feature points and two sets of deformed points with the stretched deformation of 0.55 mm (red dots) and 1.4 mm (green dots). Finally, FEA color map of the true normal strain in the X-direction, $\bar{\varepsilon}_{XX}$, at the end of the 1.4 mm stretching process were calculated from tracking results by our collaborators, as shown in Figure 5-11(e). Based on the image location in specimen, local strain concentrations can be seen in the strain map at the left end of the image due to clamping stress at the grip which diminishes toward the center of the specimen.

Two parameters, the average normal strain in the X-direction $\bar{\varepsilon}_{XX}$ and Poisson's ratio $v = -\bar{\varepsilon}_{YY}/\bar{\varepsilon}_{XX}$ ($\bar{\varepsilon}_{YY}$ is the average strain in a transverse direction perpendicular to the axis of tensile loading.) were compared between true values from test machine measurements and measured values using PAM-FEA approach. As shown in the second image of Figure 5-11(f), the relationship between the PAM-FEA measurements and the test machine measurements is seen to be linear with the R^2 value of 0.995. The high correlation indicates the validity of the linear curve-fit line is 0.53 which gives a good approximation of the elastomer material's Poisson's ratio which is known to be approximately 0.5. These results demonstrate the feasibility of proposed PAM-FEA approach in strain measurements.

5.3.2.4 Validation of The Strain Measurements on Posterior Porcine Eye

To authenticate the PAM-FEA methodology for *ex vivo* eye testing, we subsequently applied the approach on the posterior chamber of porcine eyes and validated the outcomes of the PA imaging and computations with the commercially obtained measurements.

5.3.2.4.1 Eye Preparation

In this study, a pattern of speckles was generated on the posterior surface of the porcine eye by delicately spraying red tattoo dye, thereby establishing points of contrast tracking. Subsequently, the eye preparation detailed in Chapter 5.3.1.1 was implemented. The PA images were acquired at intervals of 2 mmHg, ranging from 10 mmHg to 21mmHg.

5.3.2.4.2 Results

Results for the posterior surface strains of a porcine eye are given in Figure 5-12 (d) and (e). Points in the gray shaded region in Figure 5-12 (c) were tracked in 3D as IOP was increased from 10 mmHg to 21 mmHg during perfusion. The deformed mesh and PAM-FEA strain ε_{YY} at the IOP of 21 mmHg are shown in Figure 5-12(d) and 5-12(e) in two different views. The averages of ε_{XX} and ε_{YY} over the entire imaged region are 1.04% and 1.03%, respectively. The strains ε_{XX} and ε_{YY} of the element *C* in the ONH region of Figure 5-12 are 1.9% and 1.5%, respectively, which are substantially larger than the overall average strains.

For comparison, posterior strains were obtained from another test on a porcine eye using the commercial strain imaging system. Normal strains ε_{XX} and ε_{YY} at the IOP of 21 mmHg are given in Figure 5-12(a) and 5-12(b), respectively. At the central location of the ONH, point C in Figure 5-12(a) and 5-12(b), ε_{XX} and ε_{YY} are approximately 1.6 and 1.3%, respectively. These values are in reasonable agreement with those of the element *C* in Figure 5-12(d) and 5-12(e) considering Figure 5-12 are from different tests on different eyes. Additionally, the strains in the boundary region around the ONH are approximately 1% (yellow color) in Figure 5-12 which further confirms the similarity of the measurements made by the two different imaging systems. It should also be noted that in order to achieve sufficient tracking in the case of the commercial imaging system, more paint was needed than in the case of the PAM system. Surface paint tends to stiffen the tissue, thereby lowering surface strains, as seen in the case of the commercial imaging system.

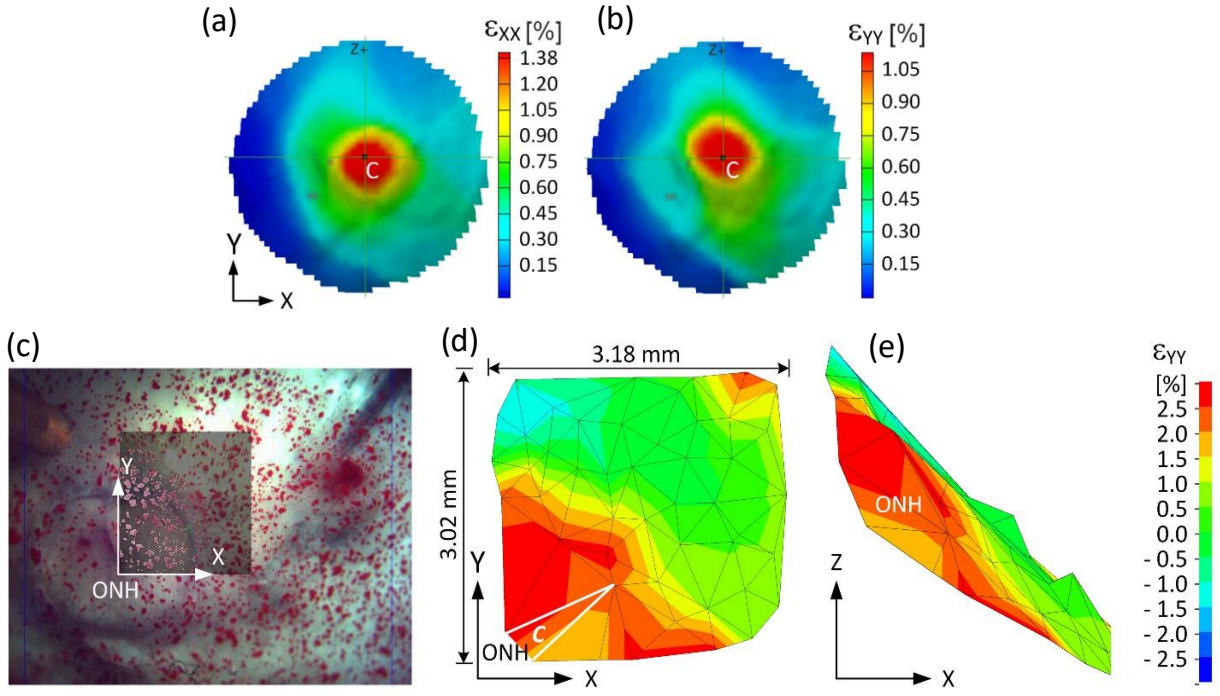


Figure 5-12: The calculated mechanical results. (a) The $\bar{\varepsilon}_{XX}$ and (b) The $\bar{\varepsilon}_{YY}$ in the ONH region of a porcine globe at 21 mmHg measured by a commercial imaging system. (c) The picture of the porcine globe with sprayed speckles. Photoacoustic image in grayscale is overlaid on the photo. (d) The deformed mesh of 78 elements showing the spatial variation of $\bar{\varepsilon}_{YY}$ at 21 mmHg in the XY-plane view, and (e) The $\bar{\varepsilon}_{YY}$ at 21 mmHg in the XZ-plane view. The figure (a) and (b) are from our unpublished data obtained from Dr. Alan Argento's Group, while (c)(d)(e) are from our published paper [147].

The validation experiments in Figure 5-12 were challenging because of known abrupt changes in geometry and stiffness at the junction between the nerve and the sclera that induce large strain gradients. Relatively high strain in the region of the ONH, and its sharp decrease across the interface with the sclera were similarly captured by the commercial system and the PAM-FEA system. A similar trend was observed for the optic nerve head of the bovine eye [198] based on measured displacement magnitudes (strains were not calculated).

5.3.2.5 Statistical Analysis

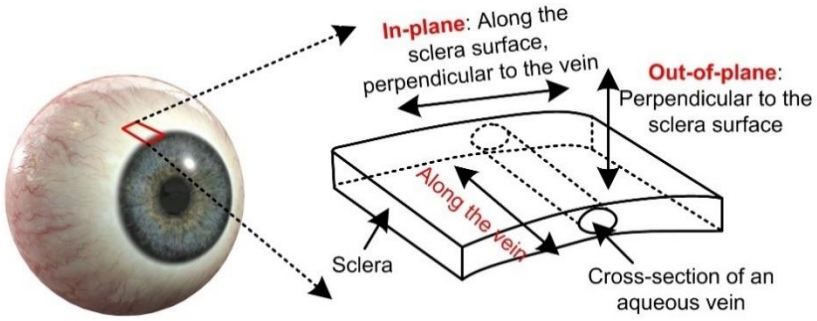


Figure 5-13: The direction diagram of veins and sclera tissues in 3D image. This figure is rebuilt based on our unpublished data.

Based on the procedures outlined in Chapter 5.3.1, statistical analysis was performed on porcine eyes. Specifically, PA images were acquired at 4 mmHg intervals while IOP was increased from 6 mmHg to either 22 mmHg or 18 mmHg, resulting in the acquisition of 4 to 5 images throughout the procedure. The PAM-FEA method was employed to produce a strain curve for each eye with respect to changes in IOP. Our previous research has demonstrated that strain is significantly and exponentially related to IOP [147]. Accounting for image vibration caused by IOP pressure, we employed exponential fitting to each curve and extracted the fitted values at an IOP of 18mmHg to enable further analysis.

To analyze the strain distribution, we initially establish three main directions, as illustrated in Figure 5-13. These directions include: 1) the in-plane direction, which is along the surface of the sclera and intersects with the vein at a 90-degree angle; 2) the out-of-plane direction, which is perpendicular to the sclera surface; and 3) the direction that runs along the vein. The strain that is present in the out-of-plane direction is referred to as the minimal principal strain, while the strain present in the in-plane direction is defined as the maximal principal strain.

Initially, we investigated the correlation between strains in aqueous veins and surrounding perilimbal scleral tissues in both out-of-plane and in-plane directions. Additionally, we analyzed changes in cross-sectional area of the veins in response to scleral strains, aiming to investigate the correlation between these two components. Subsequently, we examined whether there is a correlation between tissue stiffness and measured strains in different components of the perilimbal sclera. This was done by analyzing the relationship between strains or cross-sectional area and steady-state intraocular pressure (IOP).

5.3.3 Results

5.3.3.1 Example Results of Anterior Porcine Eye

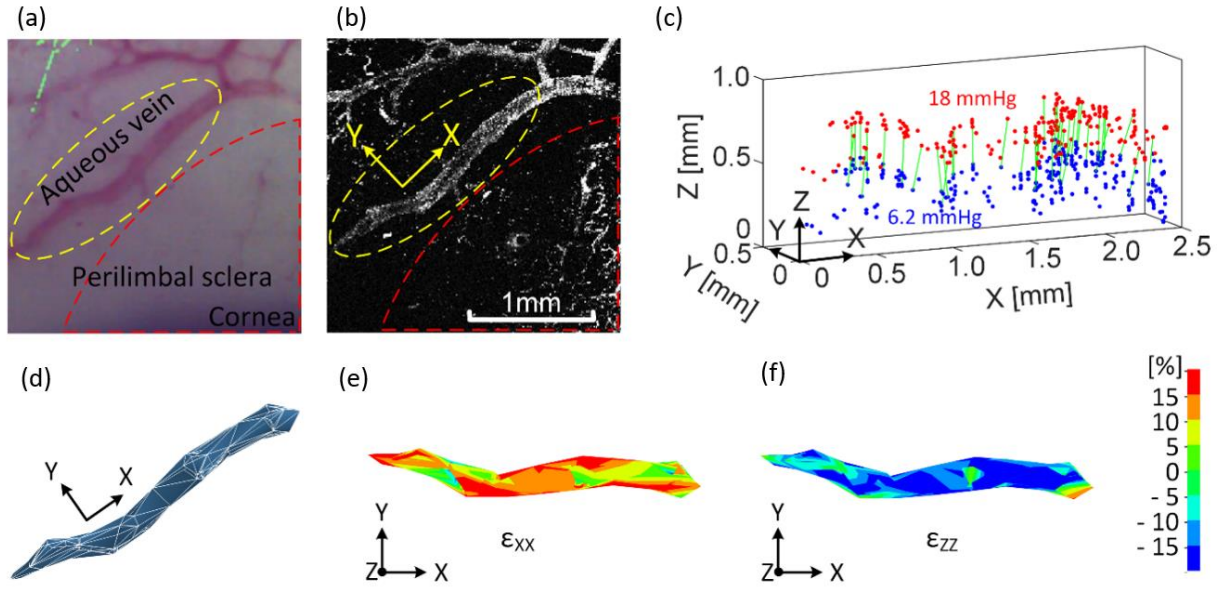


Figure 5-14: Perfused porcine eye (Example 1). (a) Photo of an aqueous vein and branched vein segments, (b) Corresponding photoacoustic image, (c) Tracked points in 3D of the circled vein, where blue and red points are at IOPs of 6.2 and 18 mmHg, respectively, and the green displacements of select identical points showing clear outward movement as the IOP increases, (d) Mesh with tetrahedral elements, and the spatial strain fields of (e) Normal strain ε_{XX} at 18 mmHg and (f) ε_{ZZ} at 18 mmHg. (The sclera under the red dashed line indicates a region of deeper veins.) The figure is reorganized from the figures in our previously published paper [147].

A porcine eye was prepared according to Chapter 5.3.1.1 and perfused with the red contrast agent. A photo of the stained aqueous veins and a corresponding PA image acquired at the wavelength of 532 nm are shown in Figure 5-14(a) and (b), respectively. Here, the red dashed lines delineate the area where the deeper aqueous veins are not visible in white light photograph but are resolved in photoacoustic imaging. The Z-direction is perpendicular to the scleral surface

at the reference point and the X and Y axes lie roughly in the thickness of the sclera with X along the longitudinal direction of the yellow-circled vein and Y along its transverse direction. The strain at the lowest pressure (6.2 mmHg) establishes the near-zero reference strain state. At this pressure, the diameter of the vein is approximately 200 μm at its central location. Five photoacoustic images were taken as IOP gradually increased during perfusion from 6.2 mmHg to 18 mmHg, which spans the porcine IOP from very low to moderate. Blue marker points shown in Figure 5-14(c) were identified at 6.2 mmHg and tracked through 5 images. Red points in Figure 5-14(c) indicate the locations of the tracked points at 18 mmHg. Note that the tracked points are on the inner vein wall within the sclera, not on the eye's surface. Also shown on Figure 5-14(c) are the displacement vectors (green lines) of a subset (for clarity) of the points. These vectors clearly reveal the outward movements of points toward the sclera's outer surface as the eye expands in response to the increase in IOP. The locations of the points relative to their initial locations after this increase in IOP also confirm that the stained marker points were fixed to the vein's wall during the experiment and served as displacement tracers for strain calculation. Figure 5-14(d) shows 695 undeformed tetrahedral elements at 6.2 mmHg, while Figure 5-14(e) and (f) show the normal strain spatial fields ε_{XX} and ε_{ZZ}, respectively, at 18 mmHg.

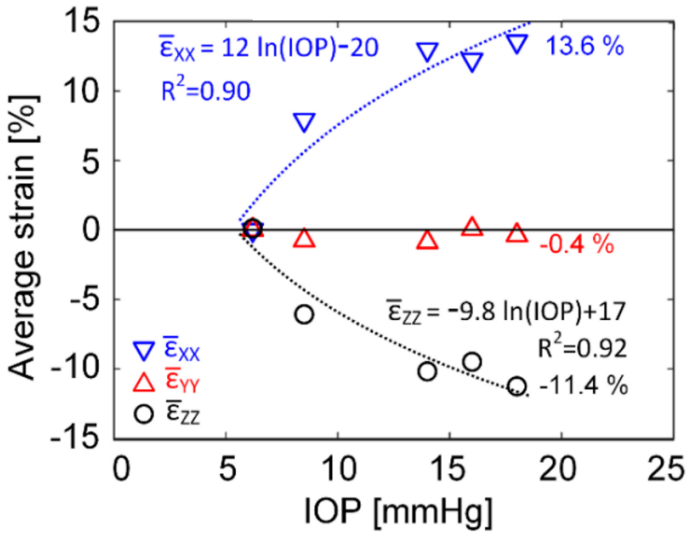


Figure 5-15: Spatial averages of the aqueous vein strain components in Figure 5-14, weighted by element volume, as functions of IOP. The dashed lines are logarithmic fits to the data. The figure also includes the coefficient of determination, R^2. The figure is from our previously published paper [147].

The vein is seen to be stretched in the nearly longitudinal direction, X, while contracted in the Z-direction. Figure 5-15 show $\bar{\varepsilon}_{XX}$, $\bar{\varepsilon}_{YY}$, $\bar{\varepsilon}_{ZZ}$, the volume-weighted average normal strains in the X-, Y-, Z-directions, respectively, as functions of IOP obtained from aqueous vein in Figure 5-14. As most soft tissues stiffen with increases of strain, logarithmic functions were fit to the measured strains as functions of IOP in Figure 5-15. The figures show the dotted line curve fits, their functions and goodness fit values, R^2.

4.3.3.2 Example Results of Anterior Human Eye

The deformed shape of the aqueous veins has been observed in both animals [170] and human [171] eyes when IOP increases. However, most studies relied on 2D imaging that cannot present the deformation of the aqueous vein normal to the eye surface.

As shown in Figure 5-16(a) and 5-16(b), we successfully captured the biomechanical behaviors of an aqueous vein in 3D using PAM-FEA in a whole human eye for the first time. Here, strain trends agree with the findings in previous studies [170, 171], namely, the aqueous vein shows a tensile/stretching strain in the plane of the sclera (x and y directions), or the direction along the vein, as IOP increases while compressive strain is observed normal to the eye surface as shown in Figure 5-16(c). This is expected since the sclera thins in the z direction and stretches in-plane due to IOP increase. In the same way, the strain curves in both the sclera and aqueous veins in Figures 5-16(d) and 5-16(e) qualitatively agree with those determined for a porcine eye in Figure 5-16. These results substantiate the necessity to investigate the deformed shape of aqueous veins in 3D using the proposed PAM-FEA approach.

4.3.3.3 Results of Statistical Analysis

Then we repeated the procedures in Chapter 5.3.2.5 and 5.3.1.1 on 8 porcine eyes. Figure 5-17 displays the statistics of large number of porcine eyes with ICG solution injected. Figures 5-17(a) and (b) present the average PAM-FEA strain measurements obtained from aqueous veins across various eyes, along their entire length, and the corresponding strains in the surrounding perilimbal sclera, within a physiologic range of IOP. The results demonstrate the potential dynamic range achievable in the proposed experiments and reveal a significant contrast between the average strain observed in the perilimbal sclera and the veins, particularly in the in-plane direction as depicted in (a). To obtain a smooth representation, the strain curves were fitted to the

same exponential functions and evaluated at 18 mmHg. Figure 5-17(c) illustrates that the eye with a lower perilimbal sclera strain, indicative of relatively stiff perilimbal sclera, exhibits lower aqueous vein strain in-plane compared to those with a higher perilimbal sclera strain, indicative of relatively soft perilimbal sclera. Hence, the deformation ability of perilimbal sclera influences the strain within the aqueous veins.

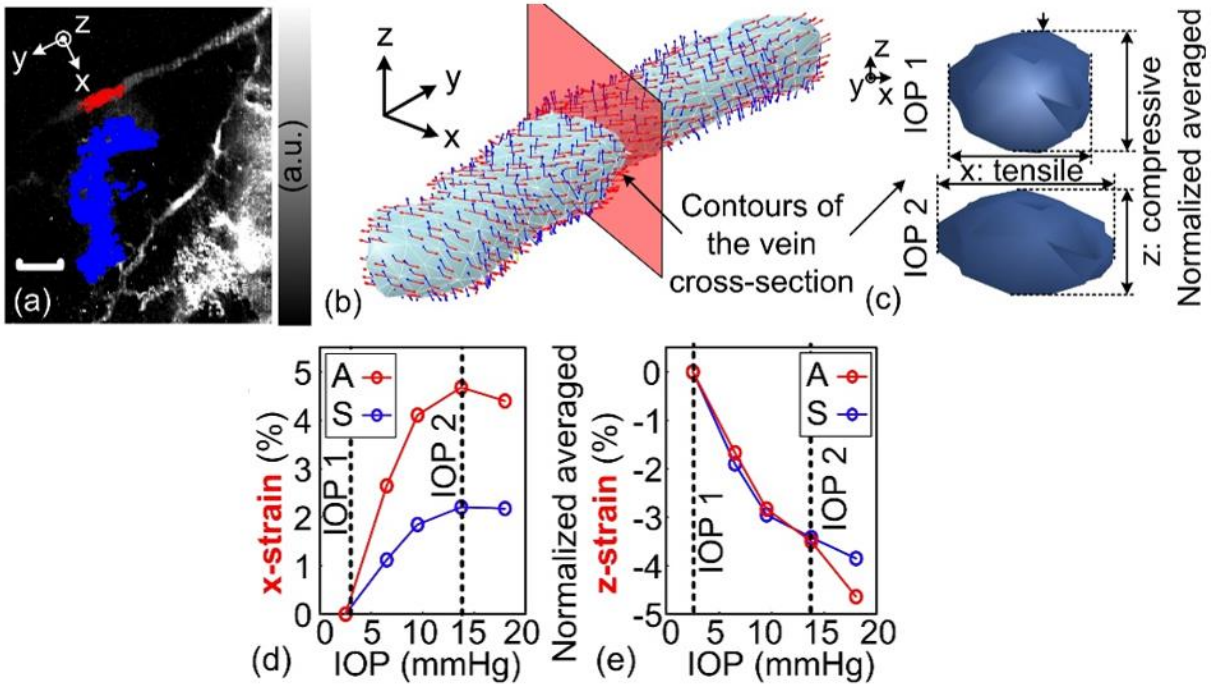


Figure 5-16: PAM-FEA analysis on human eye. (a) PAM image of a small tissue region with tracked spatial features of aqueous veins (red) and surrounding sclera (blue). Scalebar: 500 μm. (b) 3D finite element model of the aqueous vein. (c) Cross-section of the aqueous vein at 2.5 (IOP 1) and 14 (IOP 2) mmHg. (d-e) Strains of the aqueous veins and the surrounding sclera (normalized to the scleral thickness and the eye's diameter) in the directions across the vein (x) and normal to the eye surface (z). This figure is created based on the preliminary data gathered for the manuscript we are currently preparing.

The LS-DYNA software allows for the determination of maximum and minimum principal strain fields, enabling the calculation of the cross-sectional area changes in aqueous veins regardless of their orientation within the perilimbal sclera. The principal strains are averaged over the selected vein length. The relative cross-sectional area of the vein as a function of IOP is calculated with reference to the undeformed cross-section at a specific IOP. As illustrated in Figure 5-17(d) and (e), there are robust correlations between the strains observed in the perilimbal sclera and the cross-sectional area of aqueous veins at 18 mmHg. Eyes with lower perilimbal sclera strain exhibit smaller aqueous vein cross-sectional areas in both in-plane and out-of-plane directions.

These preliminary findings provide compelling evidence that the deformation of aqueous veins is strongly influenced by the biomechanical limitations imposed by the surrounding perilimbal sclera during IOP regulation [171].

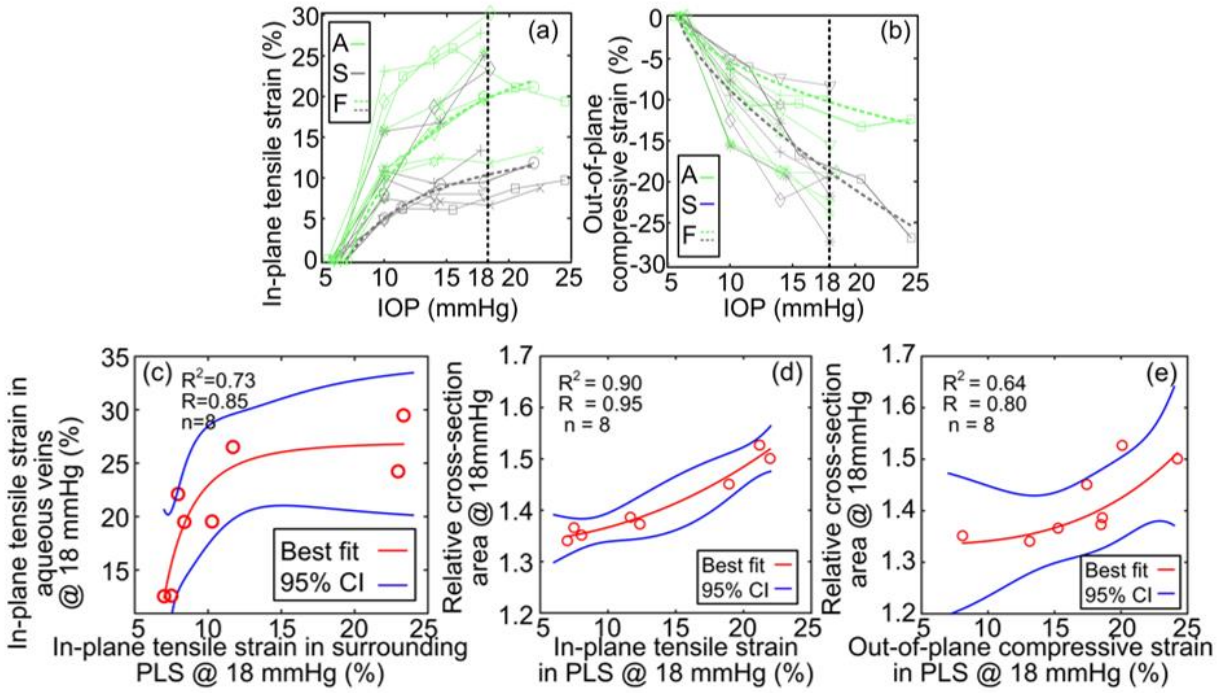


Figure 5-17: PAM-FEA of the aqueous veins and PLS during IOP elevation in porcine eyes. (a) and (b) The strains of the aqueous veins and the adjacent perilimbal sclera measured by PAM-FEA. A: Aqueous veins. S: Perilimbal sclera. F: Fittings to a pair of representative strain curves from the same eye. The fitted curves were evaluated at 18 mmHg, i.e., the black dashed line. (c) The in-plane strains of the veins vs. those of the perilimbal sclera at 18 mmHg, with confidence intervals. (d, e) The relative cross-sectional area of the aqueous veins vs. the in-plane and out-of-plane strains in the adjacent perilimbal sclera, respectively. PLS: Perilimbal sclera. This figure is created based on the preliminary data gathered for the manuscript we are currently preparing.

In our previous study [149], we have demonstrated that the steady-state IOPs of porcine eyes have strong correlation with the tangent moduli of the perilimbal sclera of the eyes (R^2=0.74, n=11), but no significant correlation with the tangent moduli of the other regions of the eye. Recent studies by other research groups also showed strong correlation between the biomechanical properties of the limbus or perilimbal sclera and the IOP [190, 195]. In this experiment, we also measured the steady-state IOPs of the eyes during perfusion at 3 µl/min using porcine eyes. Figure 5-18 (a) and (b) display the strains of aqueous veins and surrounding perilimbal sclera and the fitted curves. The deformed areas of the vein's cross-section were derived. Figure 5-18(c) and (e) show the correlations between the PAM-FEA measurements at 18 mmHg and the steady-state IOPs of the eyes. Figure 5-18 (c) indicates a strong effect of the

area of the veins' cross-section during outflow on the steady-state IOP. Specifically, eyes having aqueous veins that have larger deformed cross-section are seen to have lower steady-state IOP. Figure 5-18(d) shows that the in-plane tensile strain of the sclera near the vessel is well-correlated to the steady-state IOP of the eye, whereas Figure 5-18(e) shows that the out-of-plane strain of the sclera in same region is not correlated to steady-state IOP. The finding demonstrates the resulting effect of sclera with low strain (indicating high stiffness) during IOP elevation, and the attendant vein restriction, on the eye's steady-state IOP. The present preliminary studies in Figure 5-18(d) validate the results in our preliminary study [149] using the local 3D strains quantified by PAM-FEA during whole globe perfusion. This is a more precise measurement since it is in the exact region where the veins reside, it is within the tissue, and it is conducted on the whole, intact eye during perfusion. Furthermore, we are able to simultaneously image the aqueous veins and the surrounding perilimbal sclera, and in so doing, directly determine the effect of perilimbal sclera stiffness on the veins.

Figure 5-18(f) shows the 3D plot of the relative cross-sectional areas of aqueous veins, in-plane strains in the surrounding sclera and the corresponding steady-state IOPs. The 3D data were fitted to a first order linear regression function with steady-state IOP as the output and the other two measurements as input variables using MATLAB linear regression function fitlm.m. Figure(f) shows a strong correlation between the input variables and the output (R^2=0.82). With limited sample size, the prediction error, defined by the root of mean square (RMS) of the differences between the actual measurements and the predictions divided by the mean of actual measurements, is 10%.

5.4 Discussion and Conclusion

The study utilized a photoacoustic microscopy system that effectively captured spatial features, including aqueous veins perfused with an optical contrast agent in 3D (as depicted in Figures 5-3 to 5-6). By targeting the specific optical absorption profile of the contrast agent, the system produced high contrast images, with negligible interference from surrounding tissues. Compared to flow-based imaging technologies such as optical coherence angiography, which have shown non-uniform sensitivities to vessels with varying diameters and flow rate, photoacoustic microscopy offered relatively uniform imaging sensitivity [172]. Furthermore, photoacoustic microscopy reliably captured optical contrast even if the optical absorbers were stationary,

making it well-suited for spatial feature tracking and observing the biomechanical behaviors of aqueous veins in *ex vivo* eyes.

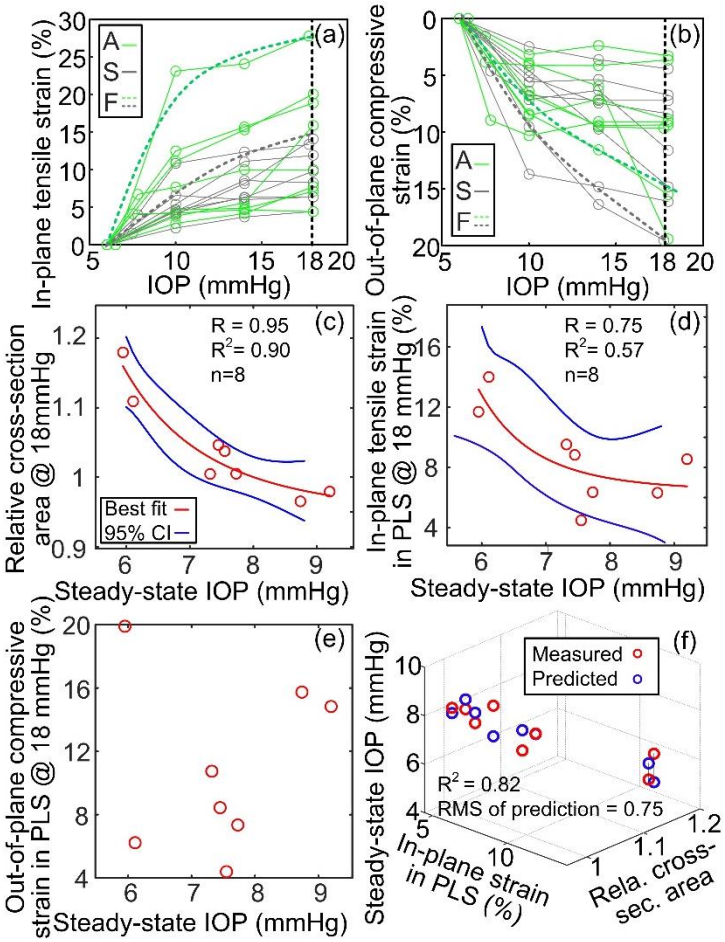


Figure 5-18: Deformations of the aqueous veins and PLS as functions of steady-state IOP in an eye. (a) and (b) The in-plane and out-of-plane strains in the aqueous veins (A) and perilimbal sclera (S), respectively. F: Fittings to a pair of representative strain curves from the same eye. The fitted functions were evaluated at 18 mmHg. (c-e) Relative cross-sectional areas of the aqueous veins, in-plane strains, and out-of-plane strains vs. steady-state IOPs of the eyes, respectively. (f) Scatter plot (red circles) of the measurement data points evaluated at 18 mmHg in (c) and (d). The blue circles are the steady-state IOPs predicted from the relative aqueous vein strains and in-plane perilimbal sclera strains using the linear regression model derived using the red circles. RMS: Root of mean square. PLS: Perilimbal sclera. This figure is created based on the preliminary data gathered for the manuscript we are currently preparing.

The PAM system in this study has axial resolution that is limited by the receiving bandwidth and aperture of the ultrasound detector, i.e. the needle hydrophone. Since scleral tissue has limited thickness [176], using ultrasound transducers with higher receiving frequency and larger aperture may further improve the axial resolution without sacrificing the capability of observing the deeply embedded aqueous veins. Furthermore, the distance between the eye surface and the tip

of the needle probe is close due to the fluidity of the coupling gel we used. This caused limited imaging field of view, higher artifacts, and distortion of the 3D information. To overcome these problems, we intend to use a backward receiving design in which the transducer is positioned behind the eye. In addition, since the methods described in this study target calculation of the dynamic strain of the aqueous veins during the variation of IOP, rapid image acquisition is desired. The imaging speed of the present system on ICG injected porcine eyes is limited by a 500 Hz laser repetition rate. A laser with a higher repetition rate will significantly increase the data acquisition rate reducing changes of strain during the acquisition.

The strain calculations were performed using a dynamic finite element software package, which utilized a series of deforming meshes to calculate the strain-displacement. Material properties were not necessary since stresses were not calculated. In this study, a finite element mesh was created from the reference image to develop an FEA model. This model can provide additional mechano-biological context for the measured behavior by calculating stresses using a suitable constitutive formulation available in the program and tissue properties. Furthermore, the model can be used in an inverse method with LS-OPT to determine properties based on a constitutive formulation [173, 174]. The FEA system allows for immediate tensor transformations to determine strains in any direction, including principal directions that indicate the extrema of the strains, or any coordinate system, including curvilinear.

There are several limitations in our studies: 1) This technique does not quantify or measure the flow within the vein. Strains in the veins and the immediate sclera are the result of three factors, IOP, venous pressure and flow stresses. The relative, quantitative contribution of these factors to the strains is difficult to parse and would require additional study design having that specific objective. 2) Due to the segmental (i.e., nonuniform) outflow around the eye, aqueous veins in the perilimbal sclera segment with high stiffness may have less optical contrast agent. If so, we will adjust the concentration of the ICG or wait for longer time until desired optical contrast is established before imaging. 3) It should be noted that there are differences between porcine eyes and human eyes, and therefore, further studies on human eyes are necessary for statistical analysis. However, the present study does not include the effects of human aging on the tissues. To minimize aging effects as a variable in all aims, human eyes from donors over 75 years old will be excluded from the study.

In conclusion, this study introduces an innovative method for image-based biomechanical analysis that combines dual-wavelength PAM for tissue identification and FEM for strain calculation. To ensure the accuracy of the proposed method, the imaging system's capacity to differentiate between aqueous veins and perilimbal sclera was validated on porcine and human eyes *ex vivo*, followed by validation of the PAM-FEA strain calculation method on tensile and posterior porcine eyes *ex vivo*. Furthermore, a larger number of porcine eyes were tested, and statistical analysis was conducted to explore the relationship between the distribution of aqueous veins and surrounding perilimbal sclera. These findings indicate that the deformations of aqueous veins are strongly influenced by biomechanical restrictions imposed by the perilimbal sclera during IOP regulation. Importantly, the study demonstrates that the steady-state IOP of a porcine eye can be predicted using the strains of aqueous veins and perilimbal sclera, which suggests the potential clinical relevance of the proposed method.

Chapter 6 Characterizing Intestinal Fibrosis Using Endoscopic Photoacoustic Strain Imaging

In this chapter, we employed a previously developed PA-US parallel endoscopic catheter probe on *in vivo* rabbit models to measure multiple parameters. These parameters encompass biomechanical modulus utilizing our proposed PA-strain method, and unmixed concentrations of hemoglobin and collagen using a previously proposed multi-spectral analysis. All these parameters can be measured *in vivo.* Our investigation focused on the ability to differentiate between fibrosis states in intestinal fibrosis by employing the biomechanical parameter and multi-parameter evaluations. This chapter presents some preliminary data results that will be included in the manuscript we are currently working on.

6.1 Introduction

Crohn's disease is classified as a chronic inflammatory bowel disease (IBD) that begins with transmural granulomatous inflammation and progresses to obstructive intestinal strictures [184, 185]. The management of this disease is condition dependent. Acute inflammatory strictures with broad areas can be treated with anti-inflammatory medicine, while chronic fibromuscular strictures require to be excised surgically [186]. Thus, the presence and extent of fibrosis is a critical pro-diagnosis indicator for treatment decisions. In addition, recent research indicates that both inflammation-dependent and independent pathways contribute to fibrosis [184]. Even though intestinal inflammation is the primary cause of fibrosis, only anti-inflammatory therapy may not halt the progression of fibrosis [187, 188]. Therefore, technologies that target fibrosis are critical for predicting and monitoring patient response to treatment and the need for surgery [189].

Endoscopy, as a conventional and standard imaging method, has a restricted view of the intestinal wall surface and cannot identify transmural or extramural disease [190, 191]. Even though cross-sectional imaging approaches, including bowel ultrasonography, computed tomography enterography and magnetic resonance imaging enterography, can fully assess the presence of inflammatory in whole thickness, these modalities are not able to differentiate inflammatory from fibrotic strictures [193, 192]. Photoacoustic (PA) imaging is a non-ionizing, non-radiative method and has spectral fingerprint absorption that can provide both structural and functional information [11]. Transabdominal/transrectal multispectral PA imaging was proven in previous studies to be capable of discriminating inflammatory levels *in vivo* based on unmixed hemoglobin content [194, 195]. However, it is limited in resolution and is inhibited by optical attenuation through thick walls. To achieve high accuracy, only employing a hemoglobin-based biomarker to diagnose inflammation is inadequate. To address these issues, we developed a minimized endoscopic PA-ultrasound (US) balloon catheter that maintains both optical resolution and US penetrations [196, 193].

Previous studies have demonstrated the efficacy of the endoscopic PA-US balloon catheter in diagnosing inflammation through the use of *ex vivo* human tissues and animal models [196, 193]. The endoscopic PA-US balloon catheter was found to accurately identify hemoglobin and collagen content in two wavelength ranges of 700-850 nm and 1220-1370 nm using multi-spectral unmixing. However, all these studies focused only on collagen-and-hemoglobin content-based biomarkers limiting the accuracy to distinguish between inflammation and fibrosis. Several studies have shown that the accumulating extracellular matrix formed during Crohn's disease might eventually contribute to more stiffness due to increased tissue fibrosis [184, 197, 198]. Our pilot study and other groups' using US elastography also discovered that increased stiffness has high correlation with the intestinal fibrosis levels in Crohn's disease [199, 200, 201, 202]. Nevertheless, US elastography has difficulty in the detecting of early fibrosis and measuring stress [203]. Our designed real-time endoscopic PA-US balloon catheter was composed of a hydrostatic balloon that has the capability to changed shape with water dilation [196]. Thus, it is able to track the changes of the PA signals and shape deformation during the balloon expansion, defined as PA-strain, noninvasively. Overall, by monitoring PA compressing images, we were able to quantify the stiffness of intestinal strictures. In our earlier publication [109], we proposed this idea for measuring strain and Young's modulus using PA imaging, but it

was not mathematically or experimentally explained and only tested on a small number of rabbit samples.

In this study, we further demonstrated the feasibility of the prototype endoscopic PA-US imaging balloon catheter in stiffness measurement on *in vivo* rabbit model. The performance of PA-strain was examined by comparing with the *ex vivo* measurements at the same position using the microelastometer. Multivariate parameter analysis using stiffness and the content ratio between collagen and hemoglobin were subsequently conducted to prove the sensitivity of the design.

6.2 Experiment Setup

6.2.1 System Setup

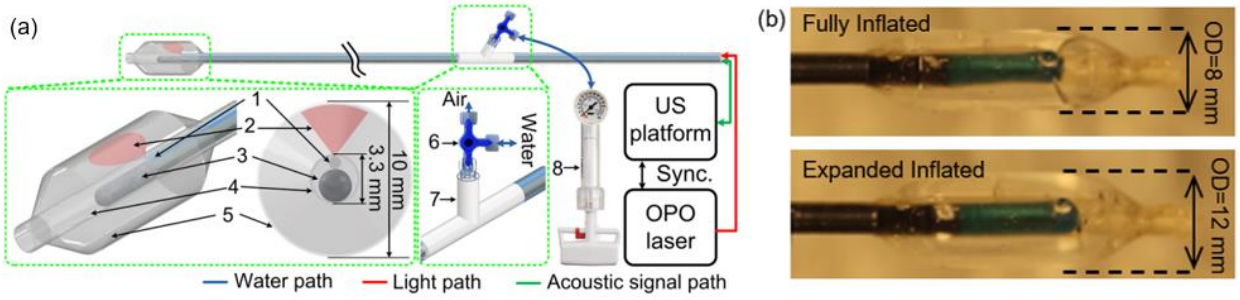


Figure 6-1: The diagram of experiment design. (a) The system setup of prototype endoscopic PA-US catheter probe from our previous published paper [244]. The structures marked with green boxes on top are magnified in the bottom. 1) Side-firing fiber optics with 800 μm core. 2) Illumination delivered by the side-firing fiber optic. 3) US array. 4) Semi-rigid tube to hold the relative positions of the side-firing fiber and the US transducer. 5) Hydrostatic balloon. 6) Three-way stopcock. 7) T adapter. 8) Hydrostatic pump. (b) Images of the probe head in its fully inflated and expanded states as its diameter increased from 8 mm to 12 mm. Figure (b) is from our unpublished data.

In our previous studies, a prototype endoscopic PA-US catheter probe that integrated a miniaturized US transducer array (Acunav, Siemens, 2.7mm diameter, central frequency 7.4Mhz) and a 800 μm side-firing fiber in a medical grade hydrostatic balloon was developed [196]. As shown in Figure 6-1(a), the probe was composed of an imaging head and a pump end. For the pump end, a hydrostatic pump was connected using a T-adapter and three-way stopcock, enabling manual control of the balloon inflation. For the probe head, the laser at 800 nm targeting hemoglobin content was coupled into the side-firing fiber. The laser pulses delivered 1.5 mJ per mm^2 per pulse at the balloon surface and in front of the US detector head when fully inflated (OD=8 mm), labeled in red in Figure 6-1(a). Then, the balloon can be inflated to a

diameter of 12 mm from a fully inflated diameter in Figure 6-1(b), allowing for intestinal wall pressing *in vivo* in rabbits. During the pressing, the PA-US parallel imaging was displayed and saved through a Verasonic platform in real time at the frequency of 10 Hz.

6.2.2 Data Acquisition and Analysis Method

During the experiment, the rabbits were anesthetized and placed in the left lateral position. Initially, a 3.8mm diameter endoscope lubricated with surgical lubricant was introduced into the rectum of the rabbit. This allowed for the identification of suspected disease sites, and their depths were recorded for subsequent PA scanning. Following this, the endoscopic PA-US balloon catheter with an uninflated balloon was inserted and stopped at the suspected sites. The balloon was then fully inflated, and images were obtained at the wavelength of 720 nm and 1310 nm, separately. After imaging, the laser wavelength was adjusted to 800nm, and the balloon was further expanded by pumping water until it reached an expanded state in Figure 6-1(b). During the pumping process, both US and PA images were captured at a frequency of 10Hz. The rabbit was promptly euthanized, and partial tissues at the scanned location were dissected for *ex vivo* microelastometer measurement. The remaining tissues were preserved for subsequent histological analysis. Following imaging, the scanned results were analyzed using multispectral analysis and PA-strain analysis, which will be explained in the subsequent sections.

6.2.2.1 Multispectral Analysis

In this study, we investigated the concentrations of hemoglobin c_{Hb} and collagen c_{cg} using optical absorption coefficients and reconstructed optical absorption from PA images. The method followed the procedures in our previous study [218, 220]. Two wavelengths at 720 nm and 1310 nm were selected for characterizing the hemoglobin caused by inflammation and collagen caused by fibrosis, respectively. The concentrations of total hemoglobin and collagen can be unmixed using the equation below:

$$\begin{bmatrix} c_{Hb} \\ c_{cg} \end{bmatrix} = \begin{bmatrix} \mu_{Hb720} & \mu_{cg720} \\ \mu_{Hb1310} & \mu_{cg1310} \end{bmatrix}^{-1} \times \begin{bmatrix} Ab_{720} \\ Ab_{1310} \end{bmatrix} \quad \text{Equation 6-1}$$

where μ_{Hb720} and μ_{Hb1310} are the absorption coefficients of total hemoglobin at the wavelength of 720nm and 1310nm, respectively, by taking the average of deoxygenated and oxygenated

hemoglobin absorption coefficients. The absorption coefficients of collagen (μ_{cg720} and μ_{cg1310}) were also determined at these wavelengths. All the absorption coefficients can be found in reference [221]. The reconstructed optical absorption from PA images, which is proportional to the image magnitudes, were denoted as Ab_{720} and Ab_{1310}, respectively.

6.2.2.2 PA-strain Analysis

This section comprises of two main parts. In the first part, we will establish the mathematical relationships between changes in PA magnitude and tissue modulus and propose a final equation to characterize tissue stiffness. In the second part, we will present the experimental procedures, which includes experimental measurements and data analysis.

6.2.2.2.1 Mathematical Demonstration of PA-strain

To describe the relationship between cross-section area and external pressures of thin-wall tube, Shapiro [207] firstly constructed an experimental model with a simple equation. This equation, as shown in Equation 6-2, is consistent with the simple mechanical behavior of physiologic vessels:

$$-\frac{p_i - p_e}{k_p} \propto \left(\frac{A}{A_0}\right)^{-n} \qquad \text{Equation 6-2}$$

where p_i is the internal pressure of the blood vessel, p_e is the external pressure imposed on the blood vessel, k_p is the pressure at which vessels collapse, A is the varied cross-sectional area, A_0 is the uncompressed cross-sectional area and n is size reduction constant, known to be $\frac{2}{3}$ for veins.

During the *in vivo* compression process, it is assumed that the veins have undergone significant collapse. According to the analytical tube law, which is derived from experimental findings, the difference in pressure within and outside the tube can be represented as $p_e - p_i = k_p \left(\frac{A}{A_0}\right)^{-\frac{3}{2}}$ in reference [207]. Based on this equation, the initial state is $p_e^{state\ 0} - p_i^{state\ 0} = 0$ when A equals to A_0 and the final state is $p_e^{state\ 1} - p_i^{state\ 1} = k_p \left(\frac{A^{state\ 1}}{A_0}\right)^{-\frac{3}{2}}$.

The initial PA signal distribution P_0, written as $P_0 = constant \times \mu_a \phi$, is proportional to optical absorption coefficient μ_a and light fluence ϕ [208, 209]. The effects caused by inhomogeneous

light fluence distribution $\phi(x, y)$ can be removed after calibration based on laser distribution. If we assume the PA signals were only generated by blood in tissues and blood vessels, the average of calibrated PA signals in the intestine tissue of each frame can be simplified to $PA_{mean} = \frac{A\mu_a}{S}$, where S is the tissue area and A is the total vessel area inside.

In order to determine the Young's Modulus for intestinal tissues surrounding blood vessels, we made two primary assumptions to simplify the calculation process. Firstly, we assumed that the stress experienced by the perivascular tissue is uniformly distributed throughout the tissue. Secondly, we considered the stress within the tissue to be equivalent to the transmural pressure surrounding the vessels, which accounts for the pressure difference across the vessel walls. Combining the average PA density and external pressure change between stages, the stress during pressing can be finally shown as $Stress = p_e^{state\ 1} - p_i^{state\ 1} = k_p \left(\frac{PA_{mean}^{state\ 1} S^{state\ 1}}{PA_{mean}^{state\ 0} S^{state\ 0}}\right)^{-\frac{3}{2}}$. The deformation proportional to the changes of intestine tissue thickness can also be tracked in the pressing images, which is describes as $Strain = 1 - \frac{S^{state\ 1}}{S^{state\ 0}}$. Based on the results we acquired, young's modulus E of tissues has the final description in Equation 6-3. This equation demonstrates the relationship between PA signals, tissue deformation, and Young's Modulus, which we define as PA-strain.

$$E = \frac{Stress}{Strain} = k_p[strain^{-1} \times \left(\frac{(1-strain)PA_{mean}^{state\ 1}}{PA_{mean}^{state\ 0}}\right)^{-\frac{3}{2}}] \quad \text{Equation 6-3}$$

6.2.2.2.2 Procedures of PA-strain Measurement

In this experiment, we applied the endoscopic PA-US balloon catheter to quantify stiffness by calculating Young's Modulus using strain from shape deformation in US images and stress from PA intensity variations. The balloon probe was tested in live rabbits. We first applied colonoscopy to locate the treated position. The deflated balloon catheter was then inserted through the distal colon and positioned at the treated location for each rabbit. The balloon was manually inflated up to a diameter of 12 mm in around 15 seconds. PA-US parallel imaging was displayed and saved through a Verasonic platform in real time at the rate of 10Hz.

According to previous studies, the speckle patterns caused by tissue scattering contain trackable information of tissues in time sequence stock US images [26, 210]. By exploiting the 2D

correlation of the speckle patterns with the apparent movement between two frames of US images, the changes of tissue deformation can be recovered [211, 212]. The tracking method follows our previous 2D tracking procedures in Chapter 5.3.2.1. Feature points at two different depths representing the inner and outer boundary of the intestinal wall were chosen in the t_0 (t=0s, the start image) US image shown in Figure 6-2. Then, the center of a tracking window with the size of 10x10 pixel units (0.25mmx0.125mm) were moved in a 50x10 pixel units searching region (1.25mmx1.25mm) centered at the chosen point in the US image of the next time frame. The correlation matrix between the tracking windows in the US image at $t_0 + dt$ and the reference window, the 10x10 pixel unit window centered in the US image at t_0, were calculated. The position with the highest correlation was considered as the estimated displacement of each chosen point. Repeating the procedures in US images acquired over time can achieve movement tracking. The strain can finally be described as $strain = 1 - \frac{d(t)}{d_0}$, where $d(t)$ is the distance between the lower and upper boundary in longitudinal direction and d_0 is the original distance in t_0 US image.

The averaged PA amplitudes during pressing were calculated in the co-registered region between the tracked lower and upper intestine boundaries and normalized based on the initial average PA amplitude. The scatter plots of the normalized PA amplitudes in average are shown in the third image in Figure 6-2. We selected strain equal to 0.15 for comparison, as the strain distributions of all data ranged between 0 and 0.15. The fitted line of the scatter points was used to obtain the fitted value of the normalized average PA amplitude at strain equal to 0.15. (The gray dashed line in the third image of Figure 6-2). Finally, the Young's modulus was calculated by inputting the fitted normalized average PA amplitude ($\frac{PA_{mean}^{state\ 1}}{PA_{mean}^{state\ 0}}$) at the strain of 0.15 and the corresponding strain value of 0.15 into Equation 6-3.

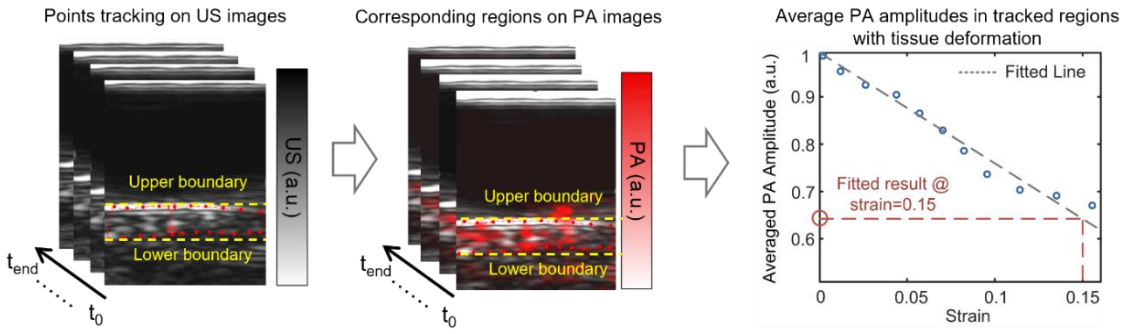


Figure 6-2: Data processing processes in PA-strain analysis. In the data processing pipeline for PA-strain analysis, the first step involves tracking feature points on the upper and lower boundary of the intestinal tissue in US images over time (as indicated by red dots in the left image), while the longitudinal borders of the tissue are marked by yellow dashed lines. In the second step, co-registered regions in PA images are extracted based on the tracking results from step one. Finally, the normalized changes in the average PA amplitudes of the extracted sections are computed as the strain increases. The average PA amplitude was normalized based on the initial average PA amplitude (Strain=0). The strain is determined by measuring the thickness changes between the upper and lower boundaries in US images. The scattered points are then fitted linearly, and the averaged PA amplitude at a strain equal to 0.15 is extracted and input into Equation 6-3 to calculate the Young's modulus. The figure is from our unpublished data.

6.2.2.3 Ex Vivo Microelastometer Measurements

To evaluate the stiffness of the tissue samples, an *ex vivo* microelastometer was used to measure their mechanical properties. The microelastometer employed a custom-built indenter, which had a contact area of 6.48 x 14.35 mm and was affixed to a force sensor (Loadstar sensors, DI-100U, REB7-001M-S, Fremont, CA), as illustrated in Figure 6-3(b) [213]. The animal bowel samples were subjected to mechanical characterization using a single-axial motor, which drove the force sensor and indenter at a rate of 0.1 mm/s to a depth of 50% of the soft tissue. To ensure a smooth contact surface, a glass panel was placed beneath the tissue sample during the pressing. The time-variant force data were automatically saved in the unit of Newton (N) with the sampling rate of 40Hz. As the PA-strain measurements performed *in vivo* in Chapter 6.2.3.2 were limited to 15% strain, only measurements below 15% were utilized to calculate Young's modulus for the *ex vivo* measurements presented in Figure 6-3(c).

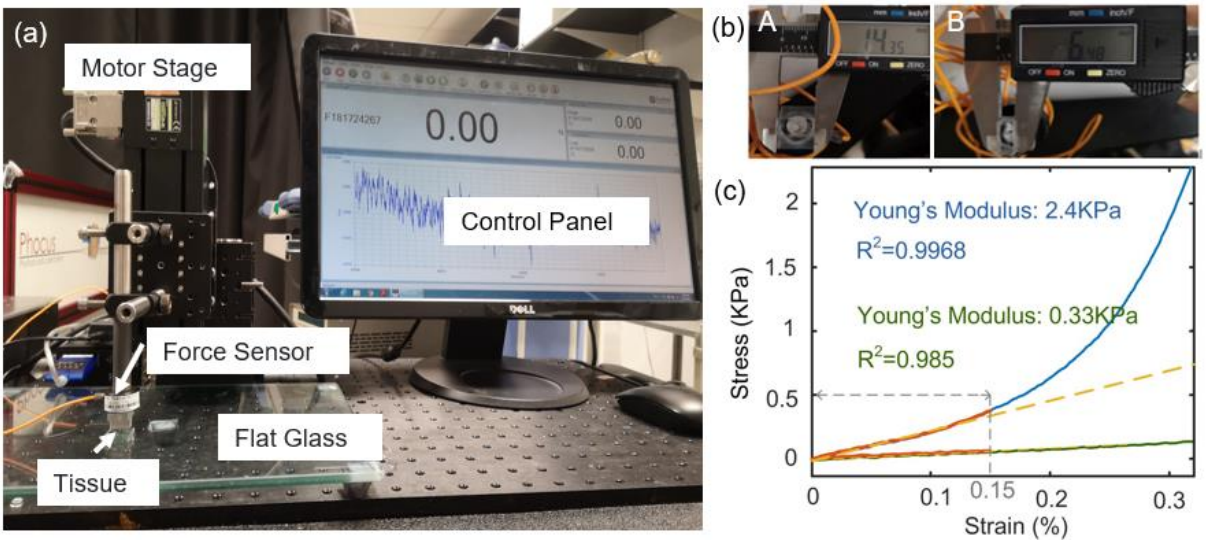


Figure 6-3: The procedures of microelastometer measurements. (a) The setup of the microelastometer system. (b) The contact area of the indenter. (c) The measured stress and strain distributions of two tissues. The blue line and green line are the measured results of chronic and acute tissue, respectively. The linear fitting (orange lines are the fitted region, and the yellow dashed lines are the fitted results) was applied between 0 and 15% strain. The figure is from our unpublished data.

To assess the relationship between the Young's modulus obtained from PA-strain imaging and the microelastometer measurements, we conducted a linear analysis. We calculated the R square and correlation to evaluate the feasibility of the mechanical model based on PA-strain imaging. This analysis allowed us to determine if there was a significant dependence between the two sets of data.

6.2.2.4 Multivariate Parameter Analysis

6.2.2.5 Histopathology

Figure 6-4 displays the histopathological findings of varying degrees of fibrosis, as seen through H&E staining images. As fibrosis progresses, there is a noticeable increase in the thickness of the muscle layer, particularly the longitudinal muscle layer. In the mucosal layer, histological analysis at a score of 2, which is indicative of a low fibrosis state, reveals localized and focally distributed collagen. However, at higher fibrosis scores, such as score 7, larger collagen scars are observed as indicated by the arrow in the corresponding example presented in Figure 6-4. The clustering of muscle and collagen can result in tissue stiffness, which is an important factor in identifying the presence and severity of fibrosis [199, 200, 201, 202].

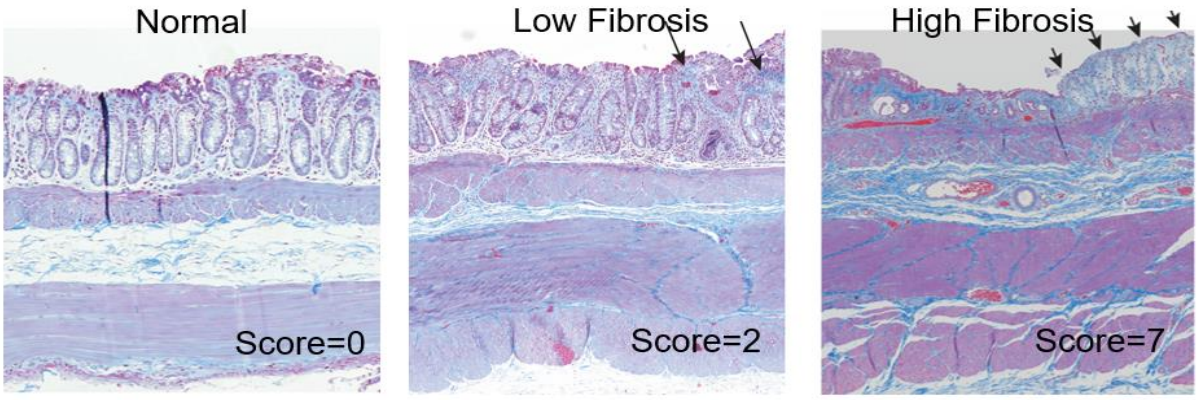


Figure 6-4: Histopathology examples of tissues at scanned positions. (a) The histology example at normal position with score equal to 0. (b) The histology example at low fibrosis position with score equal to 2. The arrow indicates the focal areas of fibrosis. (c) The histology example at high fibrosis position with score equal to 7. The arrow denotes high fibrosis areas with collagen scars. The Histopathology examples are taken from our unpublished data.

6.2.3 Animal Model

Table 6-1: The scoring system of fibrosis. Normal: score=0; Low Fibrosis: score=1-3; High Fibrosis: score=4-7.

histopathological State	Score	state
None	0	normal
Minimal	1	Low fibrosis (mild)
Mild	2	
Focally moderate	3	
Moderate	4	High fibrosis (severe)
Moderate widespread	5	
Focally severe	6	
severe	7	

In vivo evaluation of the endoscopy PA-US catheter probe was performed on rabbits, with various stages of intestinal fibrosis generated in the distal colons using trinitrobenzenesulfonic (TNBS) acid. Each rabbit was administered 40 mg of TNBS solution containing 25% to 30% ethanol on the inner surface of the rectum/distal colon at a depth of 7 cm using a syringe. Images were captured between the second and fifth day following TNBS injection. The TNBS model used in this study has been validated in previous studies conducted on rabbits [204, 205] and rats

[199, 206]. Wirtz's grading system, which ranges from score 0 to 7, was utilized in this and previous studies, as shown in Table 6-1 [222, 226]. A score of 0 indicates normal intestinal tissue, while a score of 1 to 3 is indicative of low fibrosis, with limited or focally scattered fibrotic tissues observed. A score of 4 to 7 represents a significant level of fibrosis due to the presence of severe and numerous fibrotic tissues. The histopathological results were used to determine the actual condition of each rabbit at the location of imaging. A total of 24 rabbits were scanned at 40 measured positions with 1-2 locations per rabbit, as indicated in Table 6-2.

Table 6-2: The sample size for each score using the scoring method shown in Table 6-1.

	Normal	Low fibrosis			High fibrosis				total
Score	0	1	2	3	4	5	6	7	0~7
Measured #	3	4	9	5	1	5	6	7	40
Measured #	3	18			19				40

6.3 Results

Figure 6-5 displays a set of representative images depicting normal, mild, and severe fibrosis locations. The images were obtained at different time intervals (t=0s, t=5s, and t=10s) during *in vivo* compression, and were presented as grayscale US images and co-registered PA-US dual images using a hot colormap. The PA signal changes from t=0 to t=end indicate that the severe fibrosis case exhibits a notably greater decrease in PA amplitudes than the mild fibrosis case, as presented in Figure 6-5. This finding is consistent with earlier studies indicating that the presence of more fibrosis components in severe fibrosis tissues can facilitate the squeezing out of blood during compression [109]. Furthermore, the intestinal wall thickness of the high fibrosis, outlined in green, is thicker than that of the low fibrosis. This accords with histological observations that fibrosis accumulation may induce an increase in intestinal tissue thickness, although this is not a significant marker in fibrosis categorization [222, 226]. Moreover, the processing method described in Chapter 6.2.2.2 was used to calculate the PA-strain during compression, and the examples with strain increasing were displayed in Figure 6-6. It was found

that as fibrosis progresses, the calculated PA-strain decreases more significantly when compressed with the same strain.

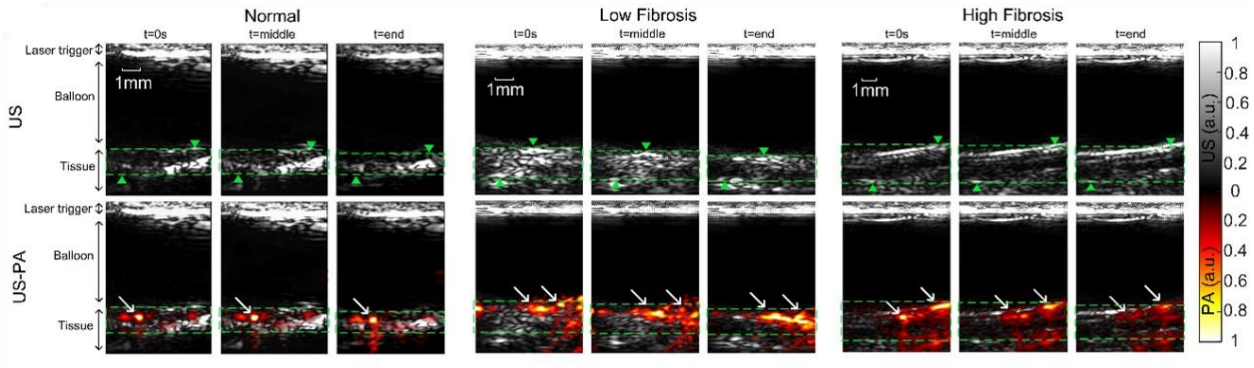


Figure 6-5: Examples of *in vivo* compression using PA-strain imaging in rabbits with normal, low, and high fibrosis. The images include US and PA images taken at the beginning, middle, and end of compression at low and high fibrosis locations. The US images are displayed in a gray colormap, while the PA images are displayed in a hot colormap. The examples are taken from our preliminary results.

In addition to PA-strain imaging, the study conducted multispectral analysis using the method described in Chapter 6.2.2.1 [196]. Figure 6-7 presents the results obtained from three representative PA-US dual images acquired *in vivo* at normal, low, and high fibrosis locations. The left column shows the B-mode US image with a gray colormap, while the middle and right columns display the PA images obtained at 720nm and 1310nm wavelengths, respectively. As described in Chapter 6.2.2.1 the signals generated at 720nm and 1310nm primarily originate from total hemoglobin and collagen, respectively. The image reveals an increase in the thickness of the intestinal walls in both the low and high fibrosis areas, as indicated by the green triangles representing the upper and lower boundaries of the rabbit colons. At the low fibrosis location, the PA images at 720nm exhibit stronger and more widely dispersed hemoglobin signals on the inner surface and inside the colon tissues, which can be attributed to the active inflammation and bleeding associated with the ulceration stage that typically precedes low fibrosis [214]. The study found that as fibrosis progresses, there is a gradual increase in the collagen signals at 1310nm, consistent with previous findings [196, 193].

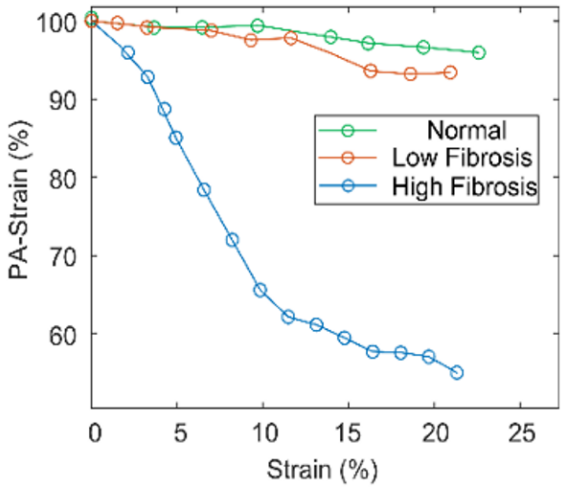


Figure 6-6: The measured PA-strain with strain increases of examples in Figure 6-5. The blue dotted line and the orange dotted line represent the results of high fibrosis and low fibrosis, respectively. The examples are taken from our preliminary results.

Next, the concentration ratios between collagen and hemoglobin were calculated by averaging the PA signals within the green dashed regions in intestine wall tissues. The resulting distribution of concentration ratios is shown in Figure 6-8(a), according to the scoring system in Table 6-1, which ranges from 0 to 7. The observed correlation coefficient between the concentration ratio and histological scores is 0.63, indicating a moderate positive association. However, due to small sample sizes, such as one for score 4 and three for the normal, the association may be underestimated (see Table 6-2). In contrast, the microelastometer measurements and PA-strains, displayed in Figure 6-8(b) and 6-8(c), respectively, exhibit insignificant correlations with the histological scores (correlation=0.41 for microelastometer measurements and correlation=0.46 for PA-strains). It should be noted that the spectral unmixing technique has demonstrated higher sensitivity in distinguishing fibrosis states, as demonstrated in our previous investigations [196, 193].

To evaluate whether the PA-strain imaging technique can accurately reflect the mechanical properties of the tissue, we performed microelastometer measurements on *ex vivo* tissue samples obtained from the imaging region. The results of the two methods were compared, and as shown in Figure 6-9, a strong correlation exists between the Young's modulus values calculated using PA-strain analysis and those measured using microelastometer (Corr=0.84, R^2=0.71). These findings demonstrate the feasibility and high sensitivity of the PA-strain imaging technique for assessing tissue mechanical properties.

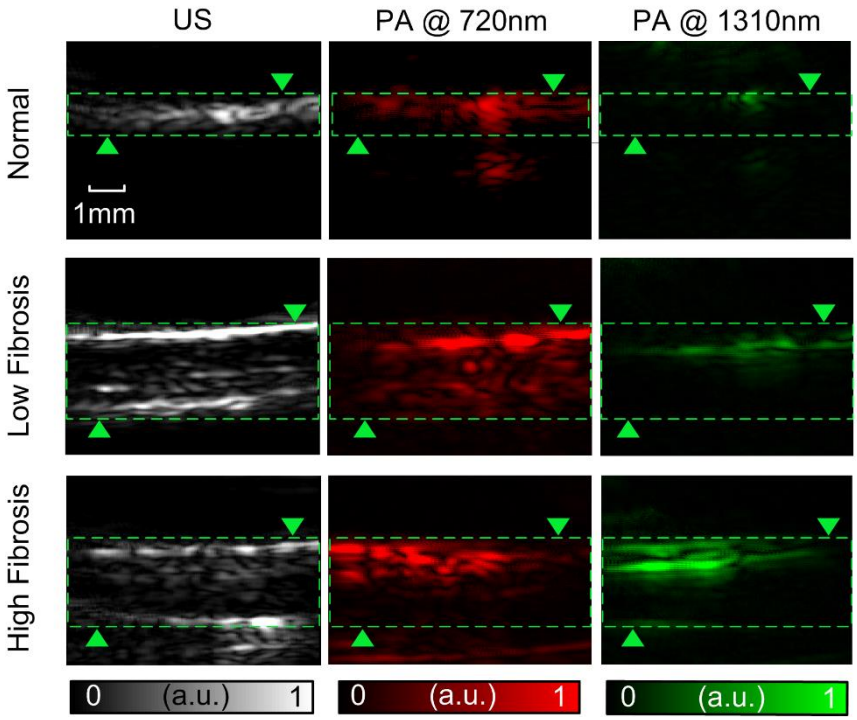


Figure 6-7: The PA-US dual images of rabbit colon acquired at the wavelength of 720 nm and 1310 nm for spectral unmixing. The images in the three columns are B-mode US images (in gray colormap), PA images at 800 nm (in red colormap), and PA images at 1310 nm (in green colormap). The PA-US pictures in the three rows were scanned in the normal, low, and high fibrosis positions. The average PA amplitudes used for spectral unmixing were calculated in the green dashed regions. The examples are taken from our preliminary results.

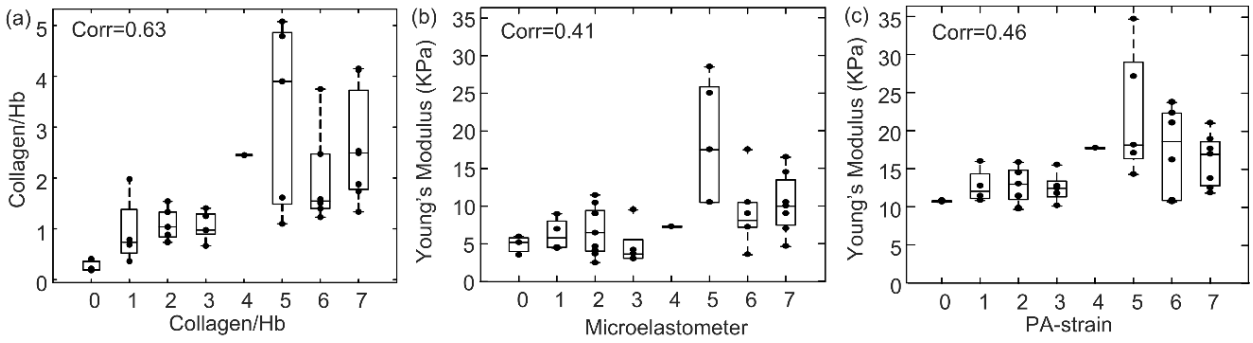


Figure 6-8: The present study investigates the distribution of three key parameters related to fibrosis states. (a) The concentration ratio between collagen and hemoglobin, (b) The Young's modulus obtained from microelastometer measurements, and (c) The Young's modulus obtained from PA-strain, as a function of increasing score ranging from 0 to 7. The examples are taken from our preliminary results.

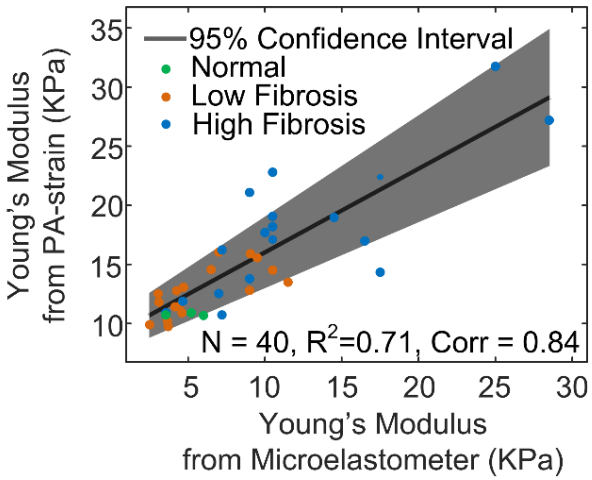


Figure 6-9: Linear Regression of Young's Modulus measured by microelastometer measurements and PA-strain analysis. The data are taken from our preliminary results.

According to Chapter 6.2.3, fibrosis states are divided into three groups: the normal (no fibrosis), low fibrosis, and high fibrosis. Figure 6-10 depicts boxplots to differentiate the three categories using three parameters: microelastometer measurements, PA-strains, and the concentration ratio of collagen to hemoglobin (Collagne/HB). Because of the low sensitivity of elastometer measurements, microelastometer classification is poor, with p-value=0.247 distinguishing between the normal and low fibrosis, and p-value =0.043 distinguishing between low fibrosis and high fibrosis. Overall, all three parameters have the capability to differentiate between the normal, low fibrosis and high fibrosis with p-value smaller than 0.05 except the classification between the normal and low fibrosis using microelastometer measurements.

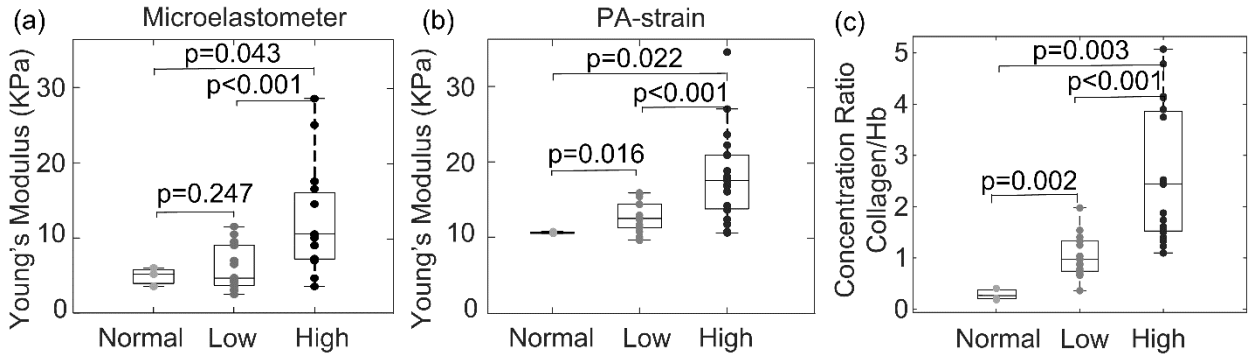


Figure 6-10: Boxplots to differentiate the normal, the low fibrosis, and high fibrosis using three parameters. (a-c) Boxplots of the normal, low and high fibrosis using microelastometer measurements, PA-strain measurements, and concentration ratio between collagen and hemoglobin, respectively. The statistical analysis was based on our preliminary results.

Then, we applied 5-fold SVM on the separative and combined parameters to further validate its ability in distinguishing between low and high fibrosis. Due to the fact in Table 6-2 that the normal only contains three datasets, the classification between normal and low fibrosis was not tested. Figure 6-11 depicts the receiver operating characteristic curve (ROC) results. Collagen/Hb has the best classification performance with an AUC of 0.94, while microelastometer and PA-strain have AUC values of 0.82 and 0.84, respectively. Since PA-strain and concentration ratio are two *in vivo* measurable characteristics, their combination was evaluated using the same SVM model. Table 6-4 demonstrates that the multivariate parameters enhance model performance (AUC increases from 94% to 95%). As indicated in Table 6-3, the correlation between the PA-strain and Collagen/Hb is as high as 0.7566, therefore the improvement is restricted.

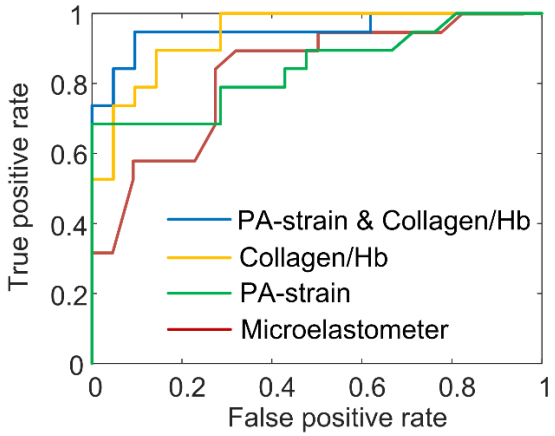


Figure 6-11: ROC curves of 5-fold SVM using single parameter or multi-variable parameters to differentiate low fibrosis and high fibrosis. It includes the ROC curves using microelastometer measurements, concentration ratio of collagen and hemoglobin, PA-strain, and the combination of the last two. The classification was based on our preliminary results.

Table 6-3: The correlations between each pair of the parameters.

Correlation	microelastometer	PA-strain	Collagen/Hb
microelastometer	1	-	-
PA-strain	0.8189	1	-
Collagen/Hb	0.7527	0.7566	1

Table 6-4: The area under the curve (AUC) for each ROC curve in Figure 6-11. Solid line displays the AUCs under the ROC curves in Figure 9. 95% CI represents the AUCs of the positive and negative bound of 95% confidence interval for each ROC curve in Figure 6-11. CI: confidence interval.

AUC	Microelastometer	PA-strain	Collagen/Hb	PA-strain & Collagen/Hb
Solid line	0.82	0.84	0.94	0.95
95% CI	0.63-0.92	0.64-0.94	0.85-0.98	0.82-0.99

6.4 Discussion and Conclusion

In our earlier work, we validated the feasibility of two-wavelength imaging to differentiate the inflammation and fibrosis Crohn's disease utilizing prototype endoscopic PA tomography and US imaging balloon catheter [196, 215]. The balloon was previously designed for the coupling of US and PA signals between the water and the intestinal wall [196, 215]. In this experiment, we replaced the balloon with a medical grade hydrostatic balloon with a moderate durometer, which allows it to inflate without shape distortion in the compression range we used. As shown in Figure 6-1(b), this medical balloon can increase the diameter of the cylinder component of the balloon from 8mm to 12mm. According to our results, this range of diameter variation provides 10% to 20% strain change of the intestinal wall in rabbit model. Based on our assumption, manually increasing the contacting pressure may partially collapse the vasculatures in the intestinal wall and produce hemoglobin signal changes. This setup has been successfully applied to differentiate fibrosis stages (including normal, low fibrosis, and high fibrosis) of rabbits *in vivo*. However, the pressure gauge we used with the water pump was insufficiently sensitive to accurately indicate the compressing pressure. A highly sensitive pressure gauge will be fitted to enable the controlling of the manual water injection.

In this paper, compared with the distribution of the concentration ratio between collagen and hemoglobin with score increasing from 0 to 7, the distribution of findings utilizing PA-strain imaging has shown low correlation which is only 0.46. Even though the PA-strain measurements in Figures 6-8 and 6-10 can differentiate between normal, low fibrosis, and high fibrosis, they are

not sensitive enough to discriminate more precise stages in the subgroups of high or low fibrosis. The distribution of the *ex vivo* microelastometer measurements in appendix also shows 0.41 correlation. This further confirms that mechanical parameters are not a highly sensitive feature in differentiating accurate stages.

To demonstrate the accuracy of the Young's modulus measured by PA-strain imaging, we fitted the results with microelastometer measurements obtained *ex vivo* linearly. Each experiment's extracted tissue depended on the depth at which it was marked. Consequently, there might be a mismatch between *ex vivo* measured location and imaging location. Given that the illness zone was always greater than the measured field of view, we may assume that the fibrosis stage of the extracted tissue corresponds to the imaging position. On the other hand, the highly sensitive pressure gauge that we will employ in the subsequent step can provide the pressure *in vivo* that can be used as the other landmark together with observed strains in US images to validate the PA-strain measurements.

The ROC curves for 5-fold SVM in Figure 6-11 illustrate that incorporating more factors can enhance the discrimination between low and high fibrosis. The dichotomy between normal and low fibrosis was not examined due to the small number of normal data in Table 6-2. In addition, the ROC curves are not smooth, indicating that the model cannot predict the group continuously. This is because we lack sufficient data size to provide continuous model features. In the subsequent stage, additional rabbits will be added to further validate this method. Simultaneously, a prototype dual imaging PA-US balloon catheter will be redesigned to fit inside the endoscope for human measurements. As illustrated in our previous paper, the balloon size and material, catheter probe size, water bump will all be improved [196].

In conclusion, we differentiated fibrosis stages (normal, mild fibrosis, and severe fibrosis) in a large number of rabbit models using our prototype endoscopic PA-US dual-imaging balloon catheter. This probe can measure multiple parameters, including collagen and hemoglobin content, as well as mechanical parameters (PA-strain imaging for strain and Young's modulus). Microelastometer and PA-strain data provide a strong correlation and R square, validating the precision of PA-strain. Moreover, the results indicated that the stages of fibrosis can be identified using each parameter individually. In addition, the combined factors enhance the distinction.

Chapter 7 Conclusions and Future Plans

7.1 Conclusions

The objective of this research is to investigate the potential of PA modalities for the quantification of tissue characteristics. The investigation encompassed three specific applications: (1) the utilization of a translational needle photoacoustic (PA) sensing probe to quantify tissue microarchitectures based on histochemical components, with the aim of assessing prostate cancer stages; (2) the implementation of a dual-wavelength PA microscopy system to evaluate the biomechanical process of aqueous veins and surrounding perilimbal sclera tissues using PA microscopy (PAM) feature tracking and finite element analysis (FEA); and (3) the assessment of fibrosis states in patients with IBD using an endoscopic PA-US balloon catheter, utilizing both elastography analysis and multi-spectral analysis. Through these applications, we sought to advance the use of PA modalities as a non-invasive and sensitive tool for characterizing tissues.

In **Chapter 3 and Chapter 4**, we present the first application of our proposed interstitial all-optical design for acquiring PA signals with deep penetration and high resolution. In the initial phase, we utilized microsphere phantom studies to demonstrate the design's ability to differentiate various microsphere sizes and concentrations through PA spectrum analysis (PASA). Subsequently, we applied the all-optical probe to *ex vivo* human prostate tissue slices, targeting various tissue components such as lipid, collagen, and nuclear cells at multiple wavelengths. The findings demonstrate the probe's potential in distinguishing between aggressive and non-aggressive tissues. In Chapter 4, we focused on refining the all-optical design to develop a translational needle PA sensing probe that could be used with biopsy needles to improve the accuracy of prostate biopsies. To achieve this, we minimized the probe's size and ensured compatibility with biopsy needles. We then conducted experiments on *ex vivo* human intact prostate to simulate clinical biopsy procedures. The results demonstrate the probe's potential for

cancer detection through multiple insertions, highlighting its potential for improving the accuracy of prostate cancer targeting.

The main contributions of this application are:

We developed a translational needle PA sensing probe that can be utilized in biopsy procedures. The probe design addresses the challenge of maintaining both the deep penetration of light and high resolution of received signals through limited invasive measurements. This innovative approach has the potential to improve the accuracy of prostate biopsies while being compatible with biopsy needles, making it highly suitable for clinical applications.

Our results show that the probe measurements can successfully differentiate between cancerous and normal tissue positions using the PASA quantification method at multiple wavelengths that target different tissue microarchitectures. This feasibility study of the design highlights its potential to improve the accuracy of prostate cancer positioning before clinical studies.

In **Chapter 5**, we employed the dual wavelength PAM system to capture images of aqueous veins and perilimbal sclera tissues separately. We conducted a biomechanical analysis using our proposed PAI-FEA method to explore the relationship between these two components. Initially, we tested the imaging system on *ex vivo* human and porcine eyes to obtain circumferential images. The results confirmed the imaging system's capability to provide rich information on both components. Subsequently, we validated the analysis method through tensile and posterior eye measurements, comparing the outcomes with published results. Finally, we applied the method to a large number of anterior chamber porcine eyes, and statistical analysis was performed to investigate the correlation between aqueous veins and the perilimbal sclera tissues. Our investigation of the biomechanical behaviors of these two components highlights the potential to establish a connection between these behaviors and the regulation of intraocular pressure (IOP).

The main contributions of this application include:

(1) We have introduced a novel approach of utilizing PAM to image various tissue components within the limbal area of the eye, followed by conducting a 3D biomechanical analysis using FEA. This pioneering approach represents the first attempt

to simultaneously perform both imaging and biomechanical analysis on different tissue components within the anterior chamber of the eye.

(2) Thus far, our PAM-FEA method has proven effective in quantifying strains in both aqueous veins and the surrounding perilimbal sclera during variations in IOP, all within a single experiment. The results obtained indicate a robust correlation between the strains of aqueous veins and perilimbal sclera during IOP variations, as well as a strong correlation between steady state pressure and sclera strain. These findings underscore the potential of our PAI-FEA method in exploring the interactive biomechanical behaviors of various anatomies within the limbal segment of the eye.

Chapter 6 outlines the development of a novel technique called Photoacoustic Strain (PA-strain) analysis, aimed at differentiating between fibrosis states of Inflammatory Bowel Disease (IBD) using an endoscopic PA catheter probe. The proposed PA-strain analysis is based on a mathematical principle that correlates PA magnitudes with tissue stiffness. *In vivo* experiments were conducted on rabbits, where the PA catheter probe was applied, and both multi-spectral analysis and PA-strain analysis were employed during data analysis.

The main contributions in this Chapter are:

(1) We conducted further validation of our previously developed PA endoscopic catheter probe on a large cohort of rabbits *in vivo*, utilizing multi-spectral analysis. This additional experimentation confirms the efficacy of our method in accurately differentiating between fibrosis states.

(2) We introduced a novel technique called PA-strain, which is capable of quantifying tissue stiffness. Our results demonstrate the effectiveness of this approach in distinguishing between normal, low fibrosis, and high fibrosis states in live rabbits. The promising outcomes suggest that our proposed PA-strain method has the potential to be a valuable tool in diagnosing fibrosis-related diseases such as IBD.

7.2 Future Plans

7.2.1 System Improvements

The present thesis describes the development of three types of PA systems: translational probe, endoscopic probe, and microscopy, for signal and imaging measurements. The translational PA sensing probe employed A-mode signals for collecting volume information, at the expense of 2D imaging. However, 2D imaging provides a visual representation that incorporates a more comprehensive and accurate understanding of the anatomy or pathology being studied. In addition, the only receiver in the translational PA sensing probe is a single-element hydrophone with wide angle. Thus, the attenuation of high-frequency signals still exists. Linear array receivers distributed in depth can improve this problem and acquire more high-frequency signals along the fiber diffusor. The development of needle-sized ultrasound transducers is constrained by several factors, including the physical size of the transducer elements (approximately 1mm in diameter), the number of elements in the array, and the imaging quality and resolution requirements. In this regard, Ansari et al. introduced a forward-viewing optical fiber array with a diameter of 3.2mm, but this design has a limited field of view of only a few millimeters [228, 229]. Notably, the fiber hydrophone principle utilized in Chapter 3 and Chapter 4 is based on Fabry-Pérot (FP) interferometers. It is feasible to incorporate multiple micro-ring resonators on the side of a single-mode fiber to enable linear array measurements. This design has been demonstrated in references [230, 231], highlighting its feasibility and potential.

For the PAM system utilized in Chapter 5, the imaging depth is limited to 350 μm, which might be shallower than the thickness of the human cornea, which can be as deep as 500 μm. To enable imaging at greater depths within corneal tissues, scan lens with longer focal length should be considered to replace the current scan lens. Our study primarily focuses on relatively larger aqueous veins, with diameters of around 100-200 μm. However, the resolution in axial resolution, as determined by the features of the US transducer, places a limit on our ability to investigate smaller or more complex vein distributions. To address this limitation, a US transducer with a higher bandwidth should be utilized.

The designs presented in Chapter 6 for the endoscopy PA catheter were developed for *in vivo* rabbit measurements. To advance this project towards clinical application, further improvements

and adaptations must be made to these designs to ensure suitability for human endoscopy procedures. It should be noted that the current design is only capable of detecting strain changes, and no stress information or pressure force can be measured. We measured the tissue stiffness *ex vivo* using microelastometer to verify the accuracy of the PA-strain method. However, if the Young's modulus can be measured *in vivo* at the scanned position, the results can be more precise. This requires a GEMS sensor or gauge sensor to be incorporated into the water injection path.

7.2.2 Quantification Improvements

Chapters 3 and 4 focused on tissue characterization using power density spectrum analysis as the main quantification method. Multiple wavelengths were utilized to study different tissue components. The results indicated that the frequency response and sensitivity of hydrophones, as well as the signal calibration method, can impact the trends of the measured parameters. Additionally, the choice of frequency window can greatly influence the results, as different trends of the linear slope and midbandfit may appear in the low and high frequency range. Therefore, a more comprehensive discussion on the explanation is required based on a large number of tissue studies.

In Chapter 5, the eye pressure changes cause the deformation of the perilimbal sclera tissues, including aqueous veins and surrounding perilimbal sclera tissues. The method used to track and analyze the changes in the anterior chamber is based on PAM-FEA which has a limited imaging field of view. As a result, it is only possible to investigate a localized region of the anterior chamber at a time. Additionally, the complex structure of the aqueous veins makes it challenging to obtain a comprehensive view of the entire anterior chamber in a single experiment. Therefore, multiple experiments may be necessary to obtain a complete understanding of the biomechanical changes in the anterior chamber due to changes in eye pressure.

In Chapter 6, we applied multi-spectral analysis and PA-strain analysis to PA-US dual images. The 7-score system was categorized into three states based on the distribution of fibrosis, predominantly in the mucosal layer, as outlined in Table 6-1. The differentiation between separative scores in low fibrosis, ranging from score 1 to score 3, did not reveal any significant difference using PA-strain, as demonstrated in Figure 6-8(c). The correlation between the 7-score

and multi-spectral analysis results, depicted in Figure 6-8(a), only achieved a moderate value of 0.63. While multivariate parameter analysis has the potential to enhance classification, the differentiation between scores is limited due to the scarcity of measurements, as indicated in Table 6-2. Furthermore, Figure 6-11 and Table 6-3 highlight the high correlation between PA-strain and multi-spectral analysis results. The result demonstrates that combining these two parameters may not lead to a significant improvement in the outcomes. In addition, although a mathematical model for PA-strain was discussed in Chapter 6.2.2.2.1, the model was developed under the assumption that high-contrast PA signals acquired at 800 nm are generated exclusively from the vessels within the tissue. However, previous studies and Figure 6-7 suggest that diffuse hemoglobin signals, as displayed in PA images of low and high fibrosis examples at 720nm, may also exist within the tissue, which could lead to a constant term in the stress equation. Consequently, further studies and phantom experiments are necessary to determine the final description of Equation 6-3.

Bibliography

[1] Yao, J. and L.V. Wang, *Photoacoustic microscopy.* Laser & Photonics Reviews, 2013. **7**(5): p. 758-778.

[2] Ni, L., et al., *Method for the biomechanical analysis of aqueous veins and perilimbal sclera by three-dimensional photoacoustic imaging and strain field calculation.* Scientific Reports, 2021. **11**(1): p. 22108.

[3] Ni, L., et al., *Assessment of prostate cancer progression using a translational needle photoacoustic sensing probe: Preliminary study with intact human prostates ex-vivo.* Photoacoustics, 2022. **28**: p. 100418.

[4] Gröhl, J., et al., *Deep learning for biomedical photoacoustic imaging: A review.* Photoacoustics, 2021. **22**: p. 100241.

[5] Kim, C., M. Jeon, and L.V. Wang, *Nonionizing photoacoustic cystography in vivo.* Optics Letters, 2011. **36**(18): p. 3599-3601.

[6] Choi, W., et al., *Clinical photoacoustic imaging platforms.* Biomedical Engineering Letters, 2018. **8**(2): p. 139-155.

[7] Daoudi, K., et al., *Handheld probe integrating laser diode and ultrasound transducer array for ultrasound/photoacoustic dual modality imaging.* Optics Express, 2014. **22**(21): p. 26365-26374.

[8] Kim, C., et al., *Performance benchmarks of an array-based hand-held photoacoustic probe adapted from a clinical ultrasound system for non-invasive sentinel lymph node imaging.* Philosophical Transactions of the Royal Society A: Mathematical, Physical and Engineering Sciences, 2011. **369**(1955): p. 4644-4650.

[9] Guan, X., et al., *Photoacoustic and ultrasound dual-modality imaging of human peripheral joints.* Journal of Biomedical Optics, 2012. **18**(1): p. 010502.

[10] Zhu, Y., et al., *Towards Clinical Translation of LED-Based Photoacoustic Imaging: A Review.* Sensors, 2020. **20**(9): p. 2484.

[11] Zhu, Y., et al., *LED-based photoacoustic imaging for monitoring angiogenesis in fibrin scaffolds.* Tissue Engineering Part C: Methods, 2019. **25**(9): p. 523-531.

[12] Kolkman, R.G., W. Steenbergen, and T.G. van Leeuwen, *In vivo photoacoustic imaging of blood vessels with a pulsed laser diode.* Lasers in medical science, 2006. **21**(3): p. 134-139.

[13] Jo, J., et al., *Detecting joint inflammation by an LED-based photoacoustic imaging system: a feasibility study.* Journal of biomedical optics, 2018. **23**(11): p. 110501.

[14] Cox, B.T., S.R. Arridge, and P.C. Beard, *Estimating chromophore distributions from multiwavelength photoacoustic images.* Journal of the Optical Society of America A, 2009. **26**(2): p. 443-455.

[15] Laufer, J., et al., *Quantitative spatially resolved measurement of tissue chromophore concentrations using photoacoustic spectroscopy: application to the measurement of blood oxygenation and haemoglobin concentration.* Physics in Medicine & Biology, 2007. **52**(1): p. 141.

[16] Laufer, J., et al., *In vitro measurements of absolute blood oxygen saturation using pulsed near-infrared photoacoustic spectroscopy: accuracy and resolution.* Physics in Medicine & Biology, 2005. **50**(18): p. 4409.

[17] Beard, P., *Biomedical photoacoustic imaging.* Interface Focus, 2011. **1**(4): p. 602-31.

[18] Fu, Q., et al., *Photoacoustic Imaging: Contrast Agents and Their Biomedical Applications.* Advanced Materials, 2019. **31**(6): p. 1805875.

[19] Wang, L.V., *Prospects of photoacoustic tomography.* Medical Physics, 2008. **35**(12): p. 5758-5767.

[20] Yang, J., S. Choi, and C. Kim, *Practical review on photoacoustic computed tomography using curved ultrasound array transducer.* Biomedical Engineering Letters, 2022. **12**(1): p. 19-35.

[21] Guo, H., et al., *Photoacoustic endoscopy: A progress review.* Journal of Biophotonics, 2020. **13**(12): p. e202000217.

[22] Zhao, T., et al., *Minimally invasive photoacoustic imaging: Current status and future perspectives.* Photoacoustics, 2019. **16**: p. 100146.

[23] Joon-Mo, Y., et al. *Endoscopic photoacoustic microscopy*. in *Proc.SPIE*. 2009.

[24] Chen, S.-L., L.J. Guo, and X. Wang, *All-optical photoacoustic microscopy.* Photoacoustics, 2015. **3**(4): p. 143-150.

[25] Kumar, V., et al.,, *Robbins & Cotran pathologic basis of disease.* Elsevier Health Sciences, 2009.

[26] Kumar, V., A. Abbas, and J. Aster, *Robbins & Cotran pathologic basis of disease*. Elsevier Health Sciences. 2009: Elsevier.

[27] Yuan, Z. and H. Jiang, *Quantitative photoacoustic tomography.* Philos Trans A Math Phys Eng Sci, 2009. **367**(1900): p. 3043-54.

[28] Yuan, Z., Q. Wang, and H. Jiang, *Reconstruction of optical absorption coefficient maps of heterogeneous media by photoacoustic tomography coupled with diffusion equation based regularized Newton Method.* Optics Express, 2007. **15**(26): p. 18076-18081.

[29] Liu, Y., H. Jiang, and Z. Yuan, *Two schemes for quantitative photoacoustic tomography based on Monte Carlo simulation.* Medical Physics, 2016. **43**(7): p. 3987-3997.

[30] Wang, L.V. and S. Hu, *Photoacoustic tomography: in vivo imaging from organelles to organs.* Science, 2012. **335**(6075): p. 1458-62.

[31] Wang, X., et al., *Noninvasive laser-induced photoacoustic tomography for structural and functional in vivo imaging of the brain.* Nature Biotechnology, 2003. **21**(7): p. 803-806.

[32] Xu, G., et al., *Quantifying Gleason scores with photoacoustic spectral analysis: feasibility study with human tissues.* Biomedical Optics Express, 2015. **6**(12): p. 4781-4789.

[33] Huang, S., et al., *Interstitial assessment of aggressive prostate cancer by physio-chemical photoacoustics: An ex vivo study with intact human prostates.* Medical Physics, 2018. **45**(9): p. 4125-4132.

[34] Amidi, E., et al., *Classification of human ovarian cancer using functional, spectral, and imaging features obtained from in vivo photoacoustic imaging.* Biomedical Optics Express 2019. **10**(5): p. 2303-2317.

[35] Xu, G., et al., *The Functional Pitch of an Organ: Quantification of Tissue Texture with Photoacoustic Spectrum Analysis.* Radiology, 2014: p. 130777.

[36] van den Berg, P.J., et al., *Preclinical detection of liver fibrosis using dual-modality photoacoustic/ultrasound system.* Biomedical Optics Express, 2016. **7**(12): p. 5081-5091.

[37] Hysi, E., et al., *Insights into photoacoustic speckle and applications in tumor characterization.* Photoacoustics, 2019. **14**: p. 37-48.

[38] Xu, G., et al., *Photoacoustic imaging features of intraocular tumors: Retinoblastoma and uveal melanoma.* PLOS ONE, 2017. **12**(2): p. e0170752.

[39] Hysi, E., R.K. Saha, and M.C. Kolios, *Photoacoustic ultrasound spectroscopy for assessing red blood cell aggregation and oxygenation.* Journal of Biomedical Optics, 2012. **17**(12): p. 1-10, 10.

[40] Chitnis, P.V., J. Mamou, and E.J. Feleppa, *Spectrum analysis of photoacoustic signals for characterizing lymph nodes.* The Journal of the Acoustical Society of America, 2014. **135**(4): p. 2372-2372.

[41] Eno, H., K.S. Ratan, and C.K. Michael, *Photoacoustic ultrasound spectroscopy for assessing red blood cell aggregation and oxygenation.* Journal of Biomedical Optics, 2012. **17**(12): p. 1-10.

[42] May, J.P., et al., *Photoacoustic Imaging of Cancer Treatment Response: Early Detection of Therapeutic Effect from Thermosensitive Liposomes.* PLOS ONE, 2016. **11**(10): p. e0165345.

[43] Fung, Y.C., *Biomechanics: Mechanical Properties of Living Tissues*. 1993: Springer.

[44] Krouskop, T.A., et al., *Elastic Moduli of Breast and Prostate Tissues under Compression.* Ultrasonic Imaging, 1998. **20**(4): p. 260-274.

[45] Chen, E.J., et al., *Young's modulus measurements of soft tissues with application to elasticity imaging.* IEEE Transactions on Ultrasonics, Ferroelectrics, and Frequency Control, 1996. **43**(1): p. 191-194.

[46] Guo, Z., Z. Xu, and L.V. Wang, *Dependence of photoacoustic speckles on boundary roughness.* J Biomed Opt, 2012. **17**(4): p. 046009.

[47] Guo, Z., L. Li, and L.V. Wang, *On the speckle-free nature of photoacoustic tomography.* Medical physics, 2009. **36**(9): p. 4084-4088.

[48] Mateo, J.L. and A. Fernández-Caballero, *Finding out general tendencies in speckle noise reduction in ultrasound images.* Expert Systems with Applications, 2009. **36**(4): p. 7786-7797.

[49] Burckhardt, C.B., *Speckle in ultrasound B-mode scans.* IEEE Transactions on Sonics and Ultrasonics, 1978. **25**(1): p. 1-6.

[50] Takeguchi, T., et al., *Practical considerations for a method of rapid cardiac function analysis based on three-dimensional speckle tracking in a three-dimensional diagnostic ultrasound system.* J Med Ultrasonics, 2010. **37**: p. 41-49.

[51] Sadhwani, A., et al., *Determination of Teflon thickness with laser speckle. I. Potential for burn depth diagnosis.* Appl. Opt., 1996. **35**: p. 5727-5735.

[52] Pastore, M.C., et al., *Speckle Tracking Echocardiography: Early Predictor of Diagnosis and Prognosis in Coronary Artery Disease.* BioMed Research International, 2021. **2021**: p. 6685378.

[53] Xu, G., et al., *Photoacoustic spectrum analysis for microstructure characterization in biological tissue: A feasibility study.* Applied Physics Letters, 2012. **101**(22): p. 221102-5.

[54] Chua, H.L., A. Huong, and K.G. Tay, *Photoacoustic systems for biomedical imaging application: A comparison study.* AIP Conference Proceedings, 2019. **2173**(1): p. 020018.

[55] Du, C., et al., *Fiber Optic Photoacoustic-Based Steering Imaging Transducer.* IEEE Photonics Technology Letters, 2022. **34**(8): p. 428-431.

[56] Kottmann, J., et al., *Mid-Infrared Fiber-Coupled Photoacoustic Sensor for Biomedical Applications.* Sensors, 2013. **13**(1): p. 535-549.

[57] Beard, P.C., et al., *Optical fiber photoacoustic–photothermal probe.* Optics Letters, 1998. **23**(15): p. 1235-1237.

[58] Omar, M., J. Aguirre, and V. Ntziachristos, *Optoacoustic mesoscopy for biomedicine.* Nature Biomedical Engineering, 2019. **3**(5): p. 354-370.

[59] Attia, A.B.E., et al., *A review of clinical photoacoustic imaging: Current and future trends.* Photoacoustics, 2019. **16**: p. 100144.

[60] Taruttis, A., G.M. van Dam, and V. Ntziachristos, *Mesoscopic and Macroscopic Optoacoustic Imaging of Cancer.* Cancer Research, 2015. **75**(8): p. 1548-1559.

[61] Das, D., et al., *Another decade of photoacoustic imaging.* Physics in Medicine & Biology, 2021. **66**(5): p. 05TR01.

[62] Wang, Y., et al., *Review of methods to improve the performance of linear array-based photoacoustic tomography.* Journal of Innovative Optical Health Sciences, 2019. **13**(02): p. 2030003.

[63] Manwar, R., K. Kratkiewicz, and K. Avanaki *Overview of Ultrasound Detection Technologies for Photoacoustic Imaging*. Micromachines, 2020. **11**, DOI: 10.3390/mi11070692.

[64] Jeon, S., et al., *Review on practical photoacoustic microscopy.* Photoacoustics, 2019. **15**: p. 100141.

[65] Zhang, H.F., et al., *Functional photoacoustic microscopy for high-resolution and noninvasive in vivo imaging.* Nature Biotechnology, 2006. **24**(7): p. 848-851.

[66] Yoon, T.J. and Y.S. Cho, *Recent advances in photoacoustic endoscopy.* World J Gastrointest Endosc, 2013. **5**(11): p. 534-9.

[67] Li, H., et al., *Advanced endoscopic methods in gastrointestinal diseases: a systematic review.* Quant Imaging Med Surg, 2019. **9**(5): p. 905-920.

[68] Basij, M., et al. *Development of an Ultrasound and Photoacoustic Endoscopy System for Imaging of Gynecological Disorders*. in *2018 IEEE International Ultrasonics Symposium (IUS)*. 2018.

[69] Liu, C., et al., *In vivo transrectal imaging of canine prostate with a sensitive and compact handheld transrectal array photoacoustic probe for early diagnosis of prostate cancer.* Biomedical Optics Express, 2019. **10**(4): p. 1707-1717.

[70] *Photoacoustic Tomography*, in *Biomedical Optics*. 2009. p. 283-321.

[71] Haisch, C., *Photoacoustic spectroscopy for analytical measurements.* Measurement Science and Technology, 2012. **23**(1): p. 012001.

[72] Hoelen, C.G.A. and F.F.M.d. Mul, *A new theoretical approach to photoacoustic signal generation.* The Journal of the Acoustical Society of America, 1999. **106**(2): p. 695-706.

[73] Cox, B., et al., *Quantitative spectroscopic photoacoustic imaging: a review*. Journal of Biomedical Optics, 2012. **17**(6): p. 061202.

[74] Xia, J., J. Yao, and L.V. Wang, *Photoacoustic tomography: principles and advances.* Electromagn Waves (Camb), 2014. **147**: p. 1-22.

[75] Krumholz, A., et al., *Photoacoustic microscopy of tyrosinase reporter gene in vivo*. Journal of Biomedical Optics, 2011. **16**(8): p. 080503.

[76] Shin, H.C., et al., *Estimation of average speed of sound using deconvolution of medical ultrasound data.* Ultrasound Med Biol, 2010. **36**(4): p. 623-36.

[77] Zhou, Y., J. Yao, and L.V. Wang, *Tutorial on photoacoustic tomography.* J Biomed Opt, 2016. **21**(6): p. 61007.

[78] Guo, Z., L. Li, and L.V. Wang, *On the speckle-free nature of photoacoustic tomography.* Med Phys, 2009. **36**(9): p. 4084-8.

[79] Glatz, T., O. Scherzer, and T. Widlak, *Texture Generation for Photoacoustic Elastography*. Journal of Mathematical Imaging and Vision, 2015. **52**(3): p. 369-384.

[80] Le, T.D., S.-Y. Kwon, and C. Lee *Segmentation and Quantitative Analysis of Photoacoustic Imaging: A Review*. Photonics, 2022. **9**, DOI: 10.3390/photonics9030176.

[81] Fadhel, M.N., et al., *Use of photoacoustic imaging for monitoring vascular disrupting cancer treatments.* J Biophotonics, 2020: p. e202000209.

[82] Kempski, K.M., et al., *In vivo photoacoustic imaging of major blood vessels in the pancreas and liver during surgery.* J Biomed Opt, 2019. **24**(12): p. 1-12.

[83] Steinberg, I., et al., *Photoacoustic clinical imaging.* Photoacoustics, 2019. **14**: p. 77-98.

[84] Lao, Y., et al., *Noninvasive photoacoustic imaging of the developing vasculature during early tumor growth.* Physics in Medicine & Biology, 2008. **53**(15): p. 4203.

[85] Mallidi, S., G.P. Luke, and S. Emelianov, *Photoacoustic imaging in cancer detection, diagnosis, and treatment guidance.* Trends in biotechnology, 2011. **29**(5): p. 213-221.

[86] Rahbar, G., et al., *Benign versus Malignant Solid Breast Masses: US Differentiation.* Radiology, 1999. **213**(3): p. 889-894.

[87] Liberman, L., et al., *Breast Lesions Detected on MR Imaging: Features and Positive Predictive Value.* American Journal of Roentgenology, 2002. **179**(1): p. 171-178.

[88] Shankar, P.M., *A general statistical model for ultrasonic backscattering from tissues.* IEEE Transactions on Ultrasonics, Ferroelectrics, and Frequency Control, 2000. **47**(3): p. 727-736.

[89] Raju, B.I. and M.A. Srinivasan, *Statistics of envelope of high-frequency ultrasonic backscatter from human skin in vivo.* IEEE Transactions on Ultrasonics, Ferroelectrics, and Frequency Control, 2002. **49**(7): p. 871-882.

[90] Saha, R.K. and M.C. Kolios, *A simulation study on photoacoustic signals from red blood cells.* The Journal of the Acoustical Society of America, 2011. **129**(5): p. 2935-2943.

[91] Amidi, E., et al., *Role of blood oxygenation saturation in ovarian cancer diagnosis using multi-spectral photoacoustic tomography.* Journal of Biophotonics, 2021. **14**(4): p. e202000368.

[92] Ratan, K.S. and C.K. Michael, *Effects of erythrocyte oxygenation on optoacoustic signals.* Journal of Biomedical Optics, 2011. **16**(11): p. 115003.

[93] Hu, S., *Emerging concepts in functional and molecular photoacoustic imaging.* Current Opinion in Chemical Biology, 2016. **33**: p. 25-31.

[94] Xu, G., et al., *The Functional Pitch of an Organ: Quantification of Tissue Texture with Photoacoustic Spectrum Analysis.* Radiology, 2014. **271**(1): p. 248-254.

[95] Feng, T., et al., *Characterization of bone microstructure using photoacoustic spectrum analysis.* Optics Express, 2015. **23**(19): p. 25217-25224.

[96] Cao, Y., et al., *Spectral analysis assisted photoacoustic imaging for lipid composition differentiation.* Photoacoustics, 2017. **7**: p. 12-19.

[97] Wu, S., et al., *Quick identification of prostate cancer by wavelet transform-based photoacoustic power spectrum analysis.* Photoacoustics, 2022. **25**: p. 100327.

[98] Glatz, J., et al., *Blind source unmixing in multi-spectral optoacoustic tomography.* Optics Express, 2011. **19**(4): p. 3175-3184.

[99] Tzoumas, S., et al., *Unmixing Molecular Agents From Absorbing Tissue in Multispectral Optoacoustic Tomography.* IEEE Transactions on Medical Imaging, 2014. **33**(1): p. 48-60.

[100] Ding, L., et al., *Constrained Inversion and Spectral Unmixing in Multispectral Optoacoustic Tomography.* IEEE Transactions on Medical Imaging, 2017. **36**(8): p. 1676-1685.

[101] Olefir, I., et al., *Deep Learning-Based Spectral Unmixing for Optoacoustic Imaging of Tissue Oxygen Saturation.* IEEE Transactions on Medical Imaging, 2020. **39**(11): p. 3643-3654.

[102] Singh, M.S. and A. Thomas, *Photoacoustic elastography imaging: a review.* J Biomed Opt, 2019. **24**(4): p. 1-15.

[103] Hwang, J.Y., et al., *Non-contact acoustic radiation force impulse microscopy via photoacoustic detection for probing breast cancer cell mechanics.* Biomedical Optics Express, 2015. **6**(1): p. 11-22.

[104] Dumont, D., et al., *Lower-limb vascular imaging with acoustic radiation force elastography: demonstration of in vivo feasibility.* IEEE Trans Ultrason Ferroelectr Freq Control, 2009. **56**(5): p. 931-44.

[105] Wang, Q., et al., *Quantitative photoacoustic elasticity and viscosity imaging for cirrhosis detection.* Applied Physics Letters, 2018. **112**(21): p. 211902.

[106] Kelly, C., et al. *An Automated Breast Ultrasound Scanner with Integrated Shear Wave Elastography, Doppler Flow Imaging and Photoacoustic Tomography*. in *2018 IEEE International Ultrasonics Symposium (IUS)*. 2018.

[107] Pengfei, H., et al., *Quantitative photoacoustic elastography in humans.* Journal of Biomedical Optics, 2016. **21**(6): p. 066011.

[108] Schoonover, R.W. and M.A. Anastasio, *Compensation of shear waves in photoacoustic tomography with layered acoustic media.* J Opt Soc Am A Opt Image Sci Vis, 2011. **28**(10): p. 2091-9.

[109] Huan, H., et al., *Mechanical Strength Evaluation of Elastic Materials by Multiphysical Nondestructive Methods: A Review.* Applied Sciences, 2020. **10**(5): p. 1588.

[110] Park, S., et al. *1E-5 Synergy and Applications of Combined Ultrasound, Elasticity, and Photoacoustic Imaging (Invited)*. in *2006 IEEE Ultrasonics Symposium*. 2006.

[111] Zhi, H., et al., *Comparison of ultrasound elastography, mammography, and sonography in the diagnosis of solid breast lesions.* J Ultrasound Med, 2007. **26**(6): p. 807-15.

[112] Karlas, A., et al., *Cardiovascular optoacoustics: From mice to men – A review.* Photoacoustics, 2019. **14**: p. 19-30.

[113] Zhu, Y., et al., *Strain-Photoacoustic Imaging as a Potential Tool for Characterizing Intestinal Fibrosis.* Gastroenterology, 2019. **157**(5): p. 1196-1198.

[114] Wilson, K.E., et al., *Multiparametric spectroscopic photoacoustic imaging of breast cancer development in a transgenic mouse model.* Theranostics, 2014. **4**(11): p. 1062.

[115] Kim, J., et al., *Multiparametric Photoacoustic Analysis of Human Thyroid Cancers In Vivo.* Cancer Research, 2021. **81**(18): p. 4849-4860.

[116] Guo, H., et al., *Assessing the development and treatment of rheumatoid arthritis using multiparametric photoacoustic and ultrasound imaging.* Journal of Biophotonics, 2019. **12**(11): p. e201900127.

[117] Jin, D., et al., *Biomechanical and morphological multi-parameter photoacoustic endoscope for identification of early esophageal disease.* Applied Physics Letters, 2017. **111**(10): p. 103703.

[118] Wang, P., Z. Chen, and D. Xing, *Multi-parameter characterization of atherosclerotic plaques based on optical coherence tomography, photoacoustic and viscoelasticity imaging.* Optics express, 2020. **28**(9): p. 13761-13774.

[119] Ishihara, M., et al., *Possibility of transrectal photoacoustic imaging-guided biopsy for detection of prostate cancer*, in *SPIE BiOS*. 2017, SPIE.

[120] Horiguchi, A., et al., *Pilot Study of Prostate Cancer Angiogenesis Imaging Using a Photoacoustic Imaging System.* Urology, 2017. **108**: p. 212-219.

[121] Wang, X., et al., *Photoacoustic tomography: a potential new tool for prostate cancer.* Biomedical Optics Express, 2010. **1**(4): p. 1117-1126.

[122] Zhang, H.K., et al., *Prostate-specific membrane antigen-targeted photoacoustic imaging of prostate cancer in vivo.* Journal of Biophotonics, 2018. **11**(9): p. e201800021.

[123] Ni, L., et al., *Characterizing the aggressiveness of prostate cancer using an all-optical needle photoacoustic sensing probe: feasibility study.* Biomedical Optics Express, 2021. **12**(8): p. 4873-4888.

[124] Jo, J., et al., *Photoacoustic spectral analysis at ultraviolet wavelengths for characterizing the Gleason grades of prostate cancer.* Optics Letters, 2020. **45**(21): p. 6042-6045.

[125] Zhu, Y., et al., *Prototype endoscopic photoacoustic-ultrasound balloon catheter for characterizing intestinal obstruction.* Biomedical Optics Express, 2022. **13**(6): p. 3355-3365.

[126] Lei, H., et al., *Characterizing intestinal strictures of Crohn’s disease in vivo by endoscopic photoacoustic imaging.* Biomedical Optics Express, 2019. **10**(5): p. 2542-2555.

[127] Joy, D., V.R. Thava, and B.B. Scott, *Diagnosis of fatty liver disease: is biopsy necessary?* European journal of gastroenterology & hepatology, 2003. **15**(5): p. 539-543.

[128] Gortzak-Uzan, L., et al., *Sentinel lymph node biopsy vs. pelvic lymphadenectomy in early stage cervical cancer: Is it time to change the gold standard?* Gynecologic Oncology, 2010. **116**(1): p. 28-32.

[129] Loeb, S., et al., *Infectious Complications and Hospital Admissions After Prostate Biopsy in a European Randomized Trial.* European Urology, 2012. **61**(6): p. 1110-1114.

[130] Litwin, M.S. and H.-J. Tan, *The Diagnosis and Treatment of Prostate Cancer: A Review.* JAMA, 2017. **317**(24): p. 2532-2542.

[131] De Visschere, P., et al., *Clinical and imaging tools in the early diagnosis of prostate cancer, a review.* Journal Belge de Radiologie, 2010. **93**(2): p. 62.

[132] Chen, Y., et al., *Prostate cancer identification via photoacoustic spectroscopy and machine learning.* Photoacoustics, 2021. **23**: p. 100280.

[133] Xu, G., et al., *Photoacoustic Spectrum Analysis for Microstructure Characterization in Biological Tissue: Analytical Model.* Ultrasound in Medicine & Biology, 2015. **41**(5): p. 1473-1480.

[134] Xu, G., et al., *High resolution Physio-chemical Tissue Analysis: Towards Non-invasive In Vivo Biopsy.* Scientific Reports, 2015: p. 16937.

[135] Xu, G., et al., *Photoacoustic imaging features of intraocular tumors: Retinoblastoma and uveal melanoma.* PLOS ONE, 2017. **12**(2): p. 0170752.

[136] Feng, T., et al., *Characterizing cellular morphology by photoacoustic spectrum analysis with an ultra-broadband optical ultrasonic detector.* Optics Express, 2016. **24**(17): p. 19853-19862.

[137] Flax, S.W., et al., *Spectral characterization and attenuation measurements in ultrasound.* Ultrasonic Imaging, 1983. **5**(2): p. 95-116.

[138] Zhang, H., et al., *Interstitial photoacoustic spectral analysis: instrumentation and validation.* Biomedical Optics Express, 2017. **8**(3): p. 1689-1697.

[139] Stamey, T.A., et al., *Localized prostate cancer. Relationship of tumor volume to clinical significance for treatment of prostate cancer.* Cancer, 1993. **71**(S3): p. 933-38.

[140] Jo, J., et al., *Photoacoustic spectral analysis at ultraviolet wavelengths for characterizing the Gleason grades of prostate cancer.* Optics Letters, 2020. **45**(21): p. 6042-6045.

[141] Morris, P., et al., *A Fabry–Pérot fiber-optic ultrasonic hydrophone for the simultaneous measurement of temperature and acoustic pressure.* 2009. **125(6)**: p. 3611.

[142] Lai, P., X. Xu, and L.V. Wang, *Dependence of optical scattering from Intralipid in gelatin-gel based tissue-mimicking phantoms on mixing temperature and time.* J Biomed Opt., 2014. **19**(3): p. 035002.

[143] Flock, S.T., et al., *Optical properties of intralipid: A phantom medium for light propagation studies.* Lasers in Surgery and Medicine, 1992. **12** (5): p. 510-519

[144] Stacy, E.W., *A Generalization of the Gamma Distribution.* Annals of Mathematical Statistics, 1962. **33(3)**: p. 1187-1192.

[145] Gomes, O., C. Combes, and A. Dussauchoy, *Parameter estimation of the generalized gamma distribution.* Mathematics and Computers in Simulation, 2008. **79**: p. 955-963.

[146] Pu, Y., et al., *Changes of collagen and nicotinamide adenine dinucleotide in human cancerous and normal prostate tissues studied using native fluorescence spectroscopy with selective excitation wavelength.* Journal of Biomedical Optics, 2010. **15**(4): p. 047008-047008-5.

[147] Morrison, C., J. Thornhill, and E. Gaffney, *The connective tissue framework in the normal prostate, B.P.H and prostate cancer: analysis by scanning electron microscopy after cellular digestion.* Urological Research, 2000. **28**(5): p. 304-307.

[148] Force, U.P.S.T., *Screening for Prostate Cancer: US Preventive Services Task Force Recommendation Statement.* JAMA, 2018. **319**(18): p. 1901-1913.

[149] Gulati, R., et al., *Individualized Estimates of Overdiagnosis in Screen-Detected Prostate Cancer.* JNCI: Journal of the National Cancer Institute, 2014. **106**(2): p. 1-5.

[150] Guggenheim, J.A., et al., *Ultrasensitive plano-concave optical microresonators for ultrasound sensing.* Nature Photonics, 2017. **11**(11): p. 714-719.

[151] Gleason, D.F. and G.T. Mellinger, *Prediction of prognosis for prostatic adenocarcinoma by combined histological grading and clinical staging.* J Urol, 1974. **111**(1): p. 58-64.

[152] Taira, A.V., et al., *Performance of transperineal template-guided mapping biopsy in detecting prostate cancer in the initial and repeat biopsy setting.* Prostate Cancer Prostatic Dis, 2010. **13**(1): p. 71-7.

[153] Ehdaie, B. and S.F. Shariat, *Magnetic resonance imaging-targeted prostate biopsy: back to the future.* Eur Urol, 2013. **63**(1): p. 141-2; discussion 143-4.

[154] Fiard, G., et al., *Targeted MRI-guided prostate biopsies for the detection of prostate cancer: initial clinical experience with real-time 3-dimensional transrectal ultrasound guidance and magnetic resonance/transrectal ultrasound image fusion.* Urology, 2013. **81**(6): p. 1372-8.

[155] Moore, C.M., et al., *Image-guided prostate biopsy using magnetic resonance imaging-derived targets: a systematic review.* Eur Urol, 2013. **63**(1): p. 125-40.

[156] Xu, G., et al., *The functional pitch of an organ: quantification of tissue texture with photoacoustic spectrum analysis.* Radiology, 2014. **271**(1): p. 248-54.

[157] Huang, S., et al., *Interstitial assessment of aggressive prostate cancer by physio-chemical photoacoustics: An ex vivo study with intact human prostates.* Med Phys, 2018.

[158] Sinha, S., et al., *Evaluation of Frequency Domain Analysis of a Multiwavelength Photoacoustic Signal for Differentiating Malignant From Benign and Normal Prostates.* Journal of Ultrasound in Medicine, 2016. **35**(10): p. 2165-2177.

[159] Patterson, M.P., et al., *Optoacoustic characterization of prostate cancer in an in vivo transgenic murine model.* J Biomed Opt, 2014. **19**(5): p. 056008.

[160] Rietbergen, J.B., et al., *Complications of transrectal ultrasound-guided systematic sextant biopsies of the prostate: evaluation of complication rates and risk factors within a population-based screening program.* Urology, 1997. **49**(6): p. 875-80.

[161] Narayana, P.A. and J. Ophir, *On the Frequency Dependence of Attenuation in Normal and Fatty Liver.* IEEE Transactions on Sonics and Ultrasonics, 1983. **30**(6): p. 379-382.

[162] Choi, W.-H. and I. Papautsky, *Fabrication of a needle-type pH sensor by selective electrodeposition.* J. Micro/Nanolith. MEMS MOEMS, 2011. **10**(2): p. 020501-1 – 020501-3.

[163] Wong, T.T.W., et al., *Fast label-free multilayered histology-like imaging of human breast cancer by photoacoustic microscopy.* Sci Adv, 2017. **3**(5): p. e1602168.

[164] Yao, D.K., et al., *In vivo label-free photoacoustic microscopy of cell nuclei by excitation of DNA and RNA.* Opt Lett, 2010. **35**(24): p. 4139-41.

[165] Power, J., et al., *Transperineal ultrasound-guided prostate biopsy: what the radiologist needs to know.* Insights into Imaging, 2022. **13**(1): p. 77.

[166] Xu, G., et al., *Photoacoustic spectrum analysis for microstructure characterization in biological tissue: A feasibility study.* Appl Phys Lett, 2012. **101**(22): p. 221102.

[167] Morrison, C., J. Thornhill, and E. Gaffney, *The connective tissue framework in the normal prostate, BPH and prostate cancer: analysis by scanning electron microscopy after cellular digestion.* Urol Res, 2000. **28**(5): p. 304-7.

[168] Pu, Y., et al., *Changes of collagen and nicotinamide adenine dinucleotide in human cancerous and normal prostate tissues studied using native fluorescence spectroscopy with selective excitation wavelength.* J Biomed Opt, 2010. **15**(4): p. 047008.

[169] Lissbrant, I.F., et al., *Blood vessels are regulators of growth, diagnostic markers and therapeutic targets in prostate cancer.* Scand J Urol Nephrol, 2001. **35**(6): p. 437-52.

[170] Kim, J.H. and J. Caprioli, *Intraocular Pressure Fluctuation: Is It Important?* J Ophthalmic Vis Res, 2018. **13**(2): p. 170-174.

[171] Johnstone, M., E. Martin, and A. Jamil, *Pulsatile flow into the aqueous veins: manifestations in normal and glaucomatous eyes.* Exp Eye Res, 2011. **92**(5): p. 318-27.

[172] Agrawal, P. and S.E. Bradshaw, *Systematic Literature Review of Clinical and Economic Outcomes of Micro-Invasive Glaucoma Surgery (MIGS) in Primary Open-Angle Glaucoma.* Ophthalmol Ther, 2018. **7**(1): p. 49-73.

[173] Binibrahim, I.H. and A.K. Bergström, *The role of trabeculectomy in enhancing glaucoma patient's quality of life.* Oman J Ophthalmol, 2017. **10**(3): p. 150-154.

[174] Saheb, H. and I.I.K. Ahmed, *Micro-invasive glaucoma surgery: current perspectives and future directions.* Current Opinion in Ophthalmology, 2012. **23**(2).

[175] Cecchin, E., S. De Marchi, and F. Tesio, *Intraocular pressure and hemodialysis.* Nephron, 1986. **43**(1): p. 73-74.

[176] Lusthaus, J.A., et al., *Aqueous outflow imaging techniques and what they tell us about intraocular pressure regulation.* Eye (Lond), 2021. **35**(1): p. 216-235.

[177] Lee, W.D., et al., *Optical coherence tomography angiography for the anterior segment.* Eye and Vision, 2019. **6**(1): p. 4.

[178] Ashton, N., *Anatomical study of Schlemm's canal and aqueous veins by means of neoprene casts. Part I. Aqueous veins.* Br J Ophthalmol, 1951. **35**(5): p. 291-303.

[179] Man, X., et al., *Perilimbal sclera mechanical properties: Impact on intraocular pressure in porcine eyes.* PLOS ONE, 2018. **13**(5): p. e0195882.

[180] Loewen, R.T., et al., *Quantification of Focal Outflow Enhancement Using Differential Canalograms.* Invest Ophthalmol Vis Sci, 2016. **57**(6): p. 2831-8.

[181] Wang, K., et al., *Estimating Human Trabecular Meshwork Stiffness by Numerical Modeling and Advanced OCT Imaging.* Invest Ophthalmol Vis Sci, 2017. **58**(11): p. 4809-4817.

[182] Huang, A.S., et al., *Aqueous Angiography with Fluorescein and Indocyanine Green in Bovine Eyes.* Transl Vis Sci Technol, 2016. **5**(6): p. 5.

[183] Huang, A.S., et al., *Aqueous Angiography in Living Nonhuman Primates Shows Segmental, Pulsatile, and Dynamic Angiographic Aqueous Humor Outflow.* Ophthalmology, 2017. **124**(6): p. 793-803.

[184] Li, P., et al., *Phase-sensitive optical coherence tomography characterization of pulse-induced trabecular meshwork displacement in ex vivo nonhuman primate eyes.* J Biomed Opt, 2012. **17**(7): p. 076026.

[185] Huang, A.S., et al., *Aqueous Angiography-Mediated Guidance of Trabecular Bypass Improves Angiographic Outflow in Human Enucleated Eyes.* Invest Ophthalmol Vis Sci, 2016. **57**(11): p. 4558-65.

[186] Overby, D., et al., *The mechanism of increasing outflow facility during washout in the bovine eye.* Invest Ophthalmol Vis Sci, 2002. **43**(11): p. 3455-64.

[187] Keller, K.E., et al., *Segmental versican expression in the trabecular meshwork and involvement in outflow facility.* Invest Ophthalmol Vis Sci, 2011. **52**(8): p. 5049-57.

[188] Watson, A.M., et al., *Ribbon scanning confocal for high-speed high-resolution volume imaging of brain.* PLoS One, 2017. **12**(7): p. e0180486.

[189] Gottschalk, H.M., et al., *Lipid Emulsion-Based OCT Angiography for Ex Vivo Imaging of the Aqueous Outflow Tract.* Invest Ophthalmol Vis Sci, 2019. **60**(1): p. 397-406.

[190] Akagi, T., et al., *Conjunctival and Intrascleral Vasculatures Assessed Using Anterior Segment Optical Coherence Tomography Angiography in Normal Eyes.* Am J Ophthalmol, 2018. **196**: p. 1-9.

[191] Gao, S.S., et al., *Optical Coherence Tomography Angiography.* Investigative Ophthalmology & Visual Science, 2016. **57**(9): p. OCT27-OCT36.

[192] Hu, Z., Q. Liu, and Y.M. Paulus, *New frontiers in retinal imaging.* International Journal of Ophthalmic Research, 2016. **2**(3): p. 148-158.

[193] Maslov, K., et al., *Optical-resolution photoacoustic microscopy for in vivo imaging of single capillaries.* Optics Letters, 2008. **33**(9): p. 929-931.

[194] Lari, D.R., et al., *Scleral mechanics: comparing whole globe inflation and uniaxial testing.* Experimental Eye Research, 2012. **94**(1): p. 128.

[195] Fazio, M.A., et al., *Regional Variations in Mechanical Strain in the Posterior Human Sclera.* Investigative Ophthalmology & Visual Science, 2012. **53**(9): p. 5326-5333.

[196] Hollman, K.W., et al., *Strain imaging of corneal tissue with an ultrasound elasticity microscope.* Cornea, 2002. **21**(1): p. 68-73.

[197] Clayson, K., et al., *3D Characterization of corneal deformation using ultrasound speckle tracking.* Journal of innovative optical health sciences, 2017. **10**(06): p. 1742005.

[198] Zvietcovich, F., et al., *Dynamic Optical Coherence Elastography of the Anterior Eye: Understanding the Biomechanics of the Limbus.* Investigative Ophthalmology & Visual Science, 2020. **61**(13): p. 7-7.

[199] Midgett, D.E., et al., *The inflation response of the human lamina cribrosa and sclera: Analysis of deformation and interaction.* Acta Biomaterialia, 2020.

[200] Chakraborty, N., et al., *Imaging of scleral collagen deformation using combined confocal raman microspectroscopy and polarized light microscopy techniques.* PLoS One, 2016. **11**(11): p. e0165520.

[201] Justin Rajesh Rajian, R.L., Pu Wang, and Ji-Xin Cheng, *Vibrational Photoacoustic Tomography: Chemical Imaging beyond*

the Ballistic Regime

J. Phys. Chem. Lett. , 2013. **4**: p. 3211−3215.

[202] Boote, C., et al., *Scleral structure and biomechanics.* Prog Retin Eye Res, 2020. **74**: p. 100773.

[203] Stamper, R.L., et al., *Becker-Shaffer's diagnosis and therapy of the glaucomas*. 2009: Elsevier Health Sciences.

[204] Wilson, A., et al., *An interferometric ex vivo study of corneal biomechanics under physiologically representative loading, highlighting the role of the limbus in pressure compensation.* Eye and Vision, 2020. **7**(1): p. 43.

[205] Tian, C., et al., *Noninvasive chorioretinal imaging in living rabbits using integrated photoacoustic microscopy and optical coherence tomography.* Optics express, 2017. **25**(14): p. 15947-15955.

[206] Kleinbaum, D.G., et al., *Applied regression analysis and other multivariable methods*. 2013: Nelson Education.

[207] Myers, K.M., et al., *The inflation response of the posterior bovine sclera.* Acta Biomaterialia, 2010. **6**(11): p. 4327-4335.

[208] Funk, R.H.W., J. Gehr, and J.W. Rohen, *Short-term hemodynamic changes in episcleral arteriovenous anastomoses correlate with venous pressure and IOP changes in the albino rabbit.* Current Eye Research, 1996. **15**(1): p. 87-93.

[209] Dobree, J.H., *Vascular Changes that occur during the Phasic Variations of Tension in Chronic Glaucoma.* British Journal of Ophthalmology, 1953. **37**(5): p. 293.

[210] Spaide, R.F., J.G. Fujimoto, and N.K. Waheed, *Image artifacts in optical coherence angiography.* Retina (Philadelphia, Pa.), 2015. **35**(11): p. 2163.

[211] Olsen, T.W., et al., *Human sclera: Thickness and surface area.* American Journal of Ophthalmology, 1998. **125**(2): p. 237-241.

[212] Girard, M.J.A., et al., *Peripapillary and Posterior Scleral Mechanics---Part II: Experimental and Inverse Finite Element Characterization.* Journal of Biomechanical Engineering, 2009. **131**(5): p. 051012-10.

[213] Grytz, R., et al., *Material properties of the posterior human sclera.* Journal of the Mechanical Behavior of Biomedical Materials, 2014. **29**(0): p. 602-617.

[214] Li, J., et al., *Pathogenesis of fibrostenosing Crohn's disease.* Translational Research, 2019. **209**: p. 39-54.

[215] Seyedian, S.S., F. Nokhostin, and M.D. Malamir, *A review of the diagnosis, prevention, and treatment methods of inflammatory bowel disease.* J Med Life, 2019. **12**(2): p. 113-122.

[216] Kumar, A., et al., *A review of the therapeutic management of Crohn's disease.* Therapeutic Advances in Gastroenterology, 2022. **15**: p. 17562848221078456.

[217] Cosnes, J., et al., *Factors affecting outcomes in Crohn's disease over 15 years.* Gut, 2012. **61**(8): p. 1140-1145.

[218] Johnson, L.A., et al., *Intestinal fibrosis is reduced by early elimination of inflammation in a mouse model of IBD: impact of a "Top-Down" approach to intestinal fibrosis in mice.* Inflamm Bowel Dis, 2012. **18**(3): p. 460-71.

[219] Higgins, P.D.R., *Measurement of Fibrosis in Crohn's Disease Strictures with Imaging and Blood Biomarkers to Inform Clinical Decisions.* Digestive Diseases, 2017. **35**(1-2): p. 32-37.

[220] Roda, G., et al., *Crohn's disease.* Nature Reviews Disease Primers, 2020. **6**(1): p. 22.

[221] Benitez, J.-M., et al., *Role of endoscopy, cross-sectional imaging and biomarkers in Crohn's disease monitoring.* Gut, 2013. **62**(12): p. 1806-1816.

[222] Furukawa, A., et al., *Cross-sectional Imaging in Crohn Disease.* RadioGraphics, 2004. **24**(3): p. 689-702.

[223] Waldner, M.J., et al., *Multispectral Optoacoustic Tomography in Crohn's Disease: Noninvasive Imaging of Disease Activity.* Gastroenterology, 2016. **151**(2): p. 238-240.

[224] Knieling, F., et al., *Multispectral Optoacoustic Tomography for Assessment of Crohn's Disease Activity.* New England Journal of Medicine, 2017. **376**(13): p. 1292-1294.

[225] Mao, R., et al., *The Mesenteric Fat and Intestinal Muscle Interface: Creeping Fat Influencing Stricture Formation in Crohn's Disease.* Inflammatory Bowel Diseases, 2018. **25**(3): p. 421-426.

[226] Rieder, F., C. Fiocchi, and G. Rogler, *Mechanisms, Management, and Treatment of Fibrosis in Patients With Inflammatory Bowel Diseases.* Gastroenterology, 2017. **152**(2): p. 340-350.e6.

[227] Stidham, R.W., et al., *Ultrasound elasticity imaging for detecting intestinal fibrosis and inflammation in rats and humans with Crohn's disease.* Gastroenterology, 2011. **141**(3): p. 819-826.e1.

[228] Chen, Y.-j., et al., *Real-Time Shear Wave Ultrasound Elastography Differentiates Fibrotic from Inflammatory Strictures in Patients with Crohn's Disease.* Inflammatory Bowel Diseases, 2018. **24**(10): p. 2183-2190.

[229] Lu, C., et al., *Ultrasound Shear Wave Elastography and Contrast Enhancement: Effective Biomarkers in Crohn's Disease Strictures.* Inflammatory Bowel Diseases, 2017. **23**(3): p. 421-430.

[230] Vestito, A., et al., *Role of Ultrasound Elastography in the Detection of Fibrotic Bowel Strictures in Patients with Crohn's Disease: Systematic Review and Meta-Analysis.* Ultraschall Med, 2019. **40**(05): p. 646-654.

[231] Allocca, M., et al., *Noninvasive Multimodal Methods to Differentiate Inflamed vs Fibrotic Strictures in Patients With Crohn's Disease.* Clinical Gastroenterology and Hepatology, 2019. **17**(12): p. 2397-2415.

[232] Zhu, Y., et al., *Prototype endoscopic photoacoustic-ultrasound balloon catheter for characterizing intestinal obstruction.* Biomed Opt Express, 2022. **13**(6): p. 3355-3365.

[233] Lei, H., et al., *Characterizing intestinal strictures of Crohn's disease in vivo by endoscopic photoacoustic imaging.* Biomed Opt Express, 2019. **10**(5): p. 2542-2555.

[234] Lei, H., et al., *Characterizing intestinal inflammation and fibrosis in Crohn's disease by photoacoustic imaging: feasibility study.* Biomed Opt Express, 2016. **7**(7): p. 2837-48.

[235] Wang, H.W., et al., *Label-free bond-selective imaging by listening to vibrationally excited molecules.* Phys Rev Lett, 2011. **106**(23): p. 238106.

[236] Shapiro, A.H., *Steady Flow in Collapsible Tubes.* Journal of Biomechanical Engineering, 1977. **99**(3): p. 126-147.

[237] Cox, B.T., et al. *Quantitative photoacoustic imaging: fitting a model of light transport to the initial pressure distribution*. in *Proc.SPIE*. 2005.

[238] Wang, L.V. and H.-i. Wu, *Biomedical optics: principles and imaging*. 2012: John Wiley & Sons.

[239] Burckhardt, C.B., *Speckle in ultrasound B-mode scans.* IEEE Transactions on Sonics and Ultrasonics, 1978. **25**(1): p. 1-6.

[240] Korstanje, J.-W.H., et al., *Development and validation of ultrasound speckle tracking to quantify tendon displacement.* Journal of Biomechanics, 2010. **43**(7): p. 1373-1379.

[241] Fai, Y., et al., *Feature-adaptive motion tracking of ultrasound image sequences using a deformable mesh.* IEEE Transactions on Medical Imaging, 1998. **17**(6): p. 945-956.

[242] Notomi, Y., et al., *Measurement of Ventricular Torsion by Two-Dimensional Ultrasound Speckle Tracking Imaging.* Journal of the American College of Cardiology, 2005. **45**(12): p. 2034-2041.

[243] Stewart, D.C., et al., *Quantitative assessment of intestinal stiffness and associations with fibrosis in human inflammatory bowel disease.* PLOS ONE, 2018. **13**(7): p. e0200377.

[244] Lei, H., et al., *Characterizing intestinal inflammation and fibrosis in Crohn’s disease by photoacoustic imaging: feasibility study.* Biomedical Optics Express, 2016. **7**(7): p. 2837-2848.

[245] Anthony, D., et al., *The characterization of a rabbit model of inflammatory bowel disease.* Int J Exp Pathol, 1995. **76**(3): p. 215-24.

[246] Dillman, J.R., et al., *US elastography-derived shear wave velocity helps distinguish acutely inflamed from fibrotic bowel in a Crohn disease animal model.* Radiology, 2013. **267**(3): p. 757-66.

[247] Wirtz, S., et al., *Chemically induced mouse models of intestinal inflammation.* Nat Protoc, 2007. **2**(3): p. 541-6.

[248] Johnson, L.A., et al., *Optimisation of Intestinal Fibrosis and Survival in the Mouse S. Typhimurium Model for Anti-fibrotic Drug Discovery and Preclinical Applications.* J Crohns Colitis, 2017. **11**(6): p. 724-736.

[249] Elson, C.O., et al., *Experimental models of inflammatory bowel disease.* Gastroenterology, 1995. **109**(4): p. 1344-1367.

[250] Xu, G., et al. *Quantitative assessment of intestinal fibrosis in vivo with spectroscopic and strain by endoscopic photoacoustic imaging*. in *Biophotonics Congress: Biomedical Optics 2020 (Translational, Microscopy, OCT, OTS, BRAIN)*. 2020. Washington, DC: Optica Publishing Group.

[251] Alles, E.J., et al., *A reconfigurable all-optical ultrasound transducer array for 3D endoscopic imaging.* Scientific Reports, 2017. **7**(1): p. 1208.

[252] Ansari, R., et al., *All-optical forward-viewing photoacoustic probe for high-resolution 3D endoscopy.* Light: Science & Applications, 2018. **7**(1): p. 75.

[253] Sherwood, T., et al., *Microring resonators on side-polished optical fiber.* IEEE Photonics Technology Letters, 2005. **17**: p. 2107-2109.

[254] Maxwell, A., et al., *Polymer Microring Resonators for High-Frequency Ultrasound Detection and Imaging.* IEEE J Sel Top Quantum Electron, 2008. **14**(1): p. 191-197.